MICROSTRUCTURE AND RHEOLOGY IN SUSPENSIONS OF SWOLLEN PMMA SPHERES

By

STEVEN EDWARD PAULIN

Bachelor of Science
Cleveland State University
Cleveland, Ohio
1986

Master of Science
Oklahoma State University
Stillwater, Oklahoma
1990

Submitted to the Faculty of the
Graduate College of the
Oklahoma State University
in partial fulfillment of
the requirements for
the Degree of
DOCTOR OF PHILOSOPHY
December, 1993

MICROSTRUCTURE AND RHEOLOGY IN
SUSPENSIONS OF SWOLLEN
PMMA SPHERES

Thesis Approved:

Thesis Adviser

Dean of the Graduate College

ACKNOWLEDGMENTS

I wish to express my gratitude to my thesis adviser, Dr. Bruce J. Ackerson, for giving me the opportunity to learn and work in his laboratory and for his help, guidance and continuous support throughout this work. Special thanks and appreciation are also extended to the other Ph.D. Advisory Committee members, Dr. H. L. Scott, Dr. Paul Westhaus, Dr. Penger Tong and Dr. D. A. Tree for their kind cooperation. Dr. M. S. Wolfe of E. I. du Pont de Nemours and Company is warmly thanked for supplying the microgel suspensions and useful discussions.

I would like to express my appreciation to Ulf Nobbmann, for his help in learning the ALV light scattering equipment and Drs. Khalid Louyidi and Frankie Black, for their assistance during my early experience in the laboratory. Mike Lucas and members of the machine shop, past and present, have been indispensable to the completion of this project.

I want to thank all members of my family for their support throughout my graduate career, especially my parents, whose love and constant support made the difficult times seem easier. Special thanks go to my beautiful wife, Carol, whose love, encouragement and patience have made all of this possible. I want to thank God for giving me a healthy son, Ian, whose warm smile has given me the strength to complete this work.

I gratefully acknowledge the financial support provided by the U.S. Department of Energy.

poppeR may say,

tHat study of

viscoElasticity

in cOncentrated,

gLassy

suspensiOns is nearly

maGic.

he maY be right.

TABLE OF CONTENTS

Chapter Page

LIST OF FIGURES

CHAPTER I

INTRODUCTION

The purpose of this thesis is to examine the rheological significance of microstructure in colloidal suspensions. From an industrial point of view, understanding the microscopic behavior of complex fluids under shear flow has applications in ceramic manufacturing, where bulk behavior is determined by the microstructure. A knowledge of how to predict this microstructure from a rheological measurement may yield a new generation of oriented ceramic materials with taylored structural properties. Fundamentally, the shear thinning and thickening observed in intermediate and concentrated dispersions pose a complicated problem, whose understanding may help progress forward the knowledge of interparticle forces in colloidal suspensions as well as mandate the examination of nonlinear rheological measurements.

In this study dispersions of crosslinked polymethylmethacrylate spheres swollen in benzyl alcohol have been examined as a function of concentration in both equilibrium and sheared nonequilibrium states. Here, the interparticle interaction is soft, repulsive, and presumably due to particle deformation. The suspensions are nearly index matched, allowing for characterization via light scattering at concentrations exceeding 10% by weight.

It is the intent of this thesis to present Chapters V and VI more or less as an independent units, to be published later as a series of papers. Chapters II and III combined are already in the process of being written as an independent paper and Chapter IV has previously been published [1].

CHAPTER II

PARTICLE CHARACTERIZATION

Introduction

The particles used in this study were prepared by standard emulsion polymerization methods at E. I. du Pont de Nemours and Company, Fabricated Products Department, Philadelphia PA, and supplied by M.S. Wolfe, Central Research and Development Department, Wilmington DE. The constituent monomers used are methyl methacrylate, with Tetraethylene glycol dimethacrylate (10%) as the crosslinker. The particles arrived dispersed in benzyl alcohol and at two initial concentrations of 6.76% and 10%. The resulting suspensions will be referred to as polymethylmethacrylate (PMMA) microgels. Here, a microgel may be considered a crosslinked particle which swells when dispersed in a suitable solvent [2]. Dispersions of microgel particles have been used as ideal polymer solutions, but may behave as a colloidal suspension, depending upon the amount of crosslinking and swelling [2–5]. A colloidal particle is typically thought of as nonswellable.

Benzyl alcohol is a better than theta solvent for the constituent polymer in PMMA microgels, resulting in swelling. The amount of swelling depends upon the amount of crosslinking, and has been studied as a function of crosslinker content by Wolfe and Scopazzi [6]. Such swelling reduces the steepness of the interparticle potential to a degree where the interaction may be termed soft.

Systematic study of suspension behavior requires characterization of the individual constituent particles (size, shape and polydispersity) as well as a means of describing concentration, usually defined as a volume fraction. Particle characterization may be achieved via quasi-elastic light scattering in the single scattering regime, where examination of both the static and dynamic scattering can aid in

clarifying the structure of unknown particles. Volume fractions, while not straightforward for microgel particles, may be obtained from a combination of viscometry measurements and knowledge of the constituent polymer density.

Effective Volume Fraction

The volume fraction for rigid spherical particles can easily be calculated as the ratio of total sphere volume to total sample volume. However, for PMMA microgels, the swollen nature of the particles makes direct volume fraction calculations based on component weights unobtainable. Comparing Einstein's dilute limit expression for the reduced viscosity of a suspension of hard spheres

$$\frac{\eta}{\eta_s} = 1 + 2.5\phi^* \tag{1}$$

with a power series expansion in concentration for the reduced viscosity,

$$\frac{\eta}{\eta_s} = 1 + [\eta]C + \cdots \tag{2}$$

enables one to write an effective volume fraction, ϕ^*, to first order as

$$\phi^* = \frac{[\eta]C}{2.5} \tag{3}$$

where $[\eta]$ is the intrinsic viscosity obtained from a measurement of suspension viscosity in the limit of vanishing particle concentration, and C the particle concentration in g/ml. Here, η and η_s are the shear viscosity of the suspension and pure solvent, respectively. Capillary viscometry measurements yield $[\eta] = 36$ ml/g [7].

Interpretation of the effective volume fraction is complicated by measured volume fractions in execess of 0.749, that of closest packing for hard spheres. While such volume fractions are unphysical for hard spheres, it is speculated that deswelling and/or deformation of PMMA microgels under close packed conditions results in physical effective volume fractions greater than that for hard spheres.

Light Scattering

Coherent light scattered from suspensions of colloidal particles contains information about the diffusion and structure of those particles. In the Rayleigh-Gans-Debye (RGD) approximation, the particle is assumed optically small compared to the wavelength of incident radiation and made up of a collection of independent point dipoles, induced by the interaction of the incident electric field with the particle [8]. A rough criteria for validity is given by $|n_p - n_s| \ll \lambda/a$, where a is a characteristic particle dimension, n_s and n_p the solvent and particle index of refraction, respectively. λ is the wavelength of incident radiation in vacuum. In essence, the RGD approximation requires that the change in phase as a wave traverses the particle is negligible. The energy, E, and momentum, $\vec{p}$, associated with the incident radiation is quantized (a photon for the visible frequencies we shall consider here) as

$$E = \hbar\omega \quad \text{and} \quad \vec{p} = \hbar\vec{k_i} \tag{4}$$

where $\hbar = 1.055 \times 10^{-34}$ J sec. is known as Planck's constant, and ω the frequency of incident radiation. Here, $\vec{k_i}$ is the incident wavevector, whose magnitude is given as

$$|\vec{k_i}| = k_i = \frac{2\pi n_s}{\lambda}. \tag{5}$$

Further, if the change in energy associated with the scattering event is small, the momentum is effectively conserved, allowing one to write

$$\vec{k} = \vec{k_i} - \vec{k_s} \quad \text{and} \quad |\vec{k}| = 2k_i \sin(\frac{\theta}{2}) \tag{6}$$

where θ is the scattering angle, and $\vec{k_i}$ and $\vec{k_s}$ are the incident and scattered wave vectors as shown in Fig. 1, respectively. For light scattering in colloidal suspensions, the observed scattered radiation is of the same wavelength as the incident, thus it is assumed that the energy change associated with the scattering is negligible, and momentum conserved.

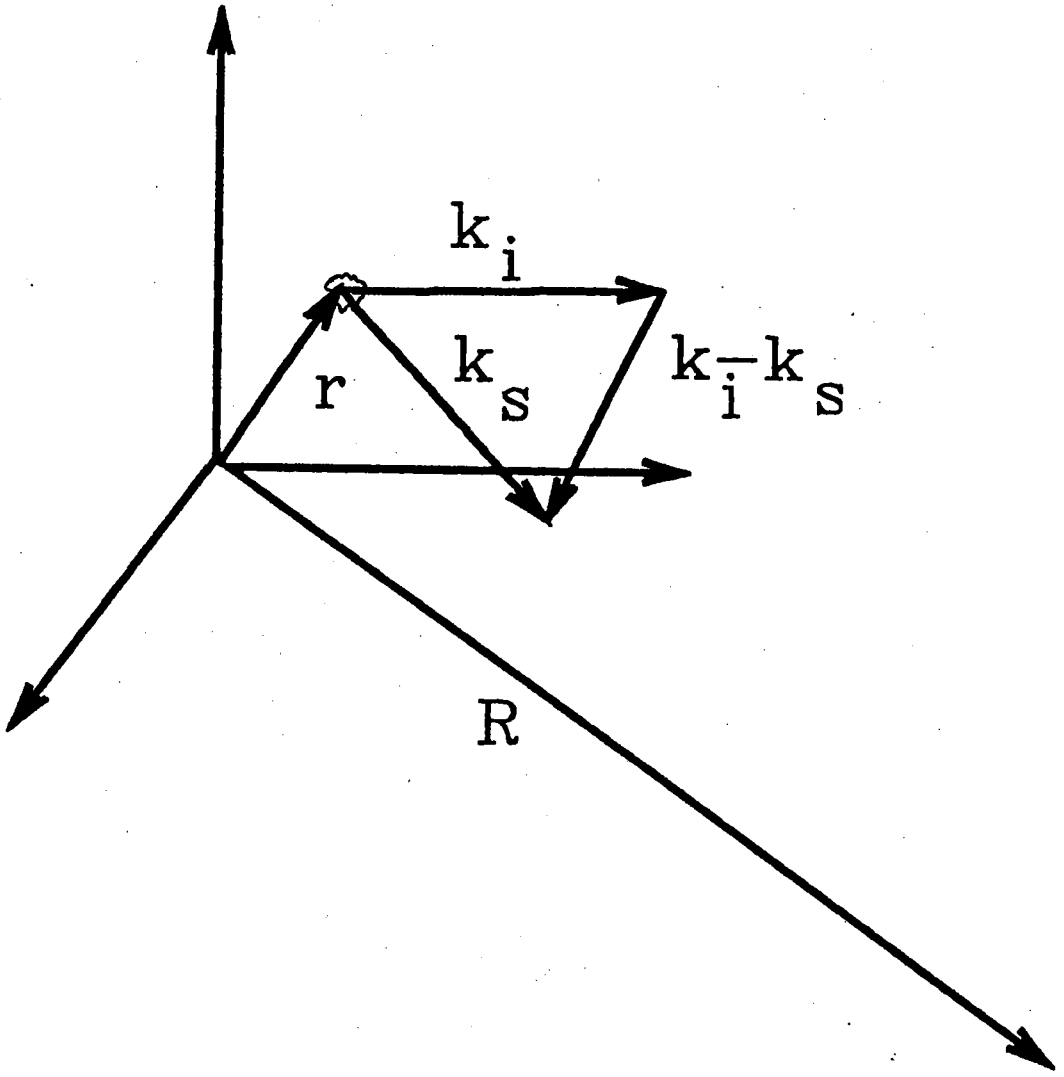

Figure 1. Scattering of radiation from a small dielectric object, depicting the incident, $\vec{k}_i$, scattered, $\vec{k}_s$, and scattering, $\vec{k} = \vec{k}_i - \vec{k}_s$, wave vectors. R is the point of observation, assumed much larger than r. θ is the scattering angle.

Static Scattering

For a plane wave incident on a dielectric particle, the total scattered electric field, $\vec{E}_t$, is given by the sum over all induced dipole fields in the particle. This may be generically written as

$$\vec{E}_t \propto \hat{p} \int_V \delta(\vec{r}) \exp^{(i\vec{k}\cdot\vec{r}-i\omega t)} dV \tag{7}$$

where $\hat{p}$ is the polarization direction, taken as perpendicular to both $\vec{k}_i$ and $\vec{k}_s$. The quantity $\vec{r}$ defines a vector from an arbitrary origin to a point within the particle, the integral being calculated over the particle volume. t represents the time dependence. $\delta(\vec{r})$ represents the distribution of dipoles within the particle and is considered constant for a uniform, homogeneous particle. $\vec{E}_t$ describes the electric field at points far from the scattering source. i.e. $|\vec{R}| \gg |\vec{r}|$, where $\vec{R}$ is the point of observation as indicated in Fig. 1.

The measured scattered intensity, I, is given by the modulus squared of the electric field. For a single particle, this may be written as

$$I(k) \propto |\vec{E}_t|^2 \propto P(k) \tag{8}$$

where $P(k)$ is called the particle form factor, specific to the geometry and structure of the particle. It is a measure of the intraparticle structure. In a suspension of particles, there is a phase shift associated with each scattering event, all of which contribute to the observed scattered intensity. However, for independent, uniform, and randomly distributed particles, averaging $\vec{E}_t^{\,2}$ over all particle positions may be done independently for each particle, resulting in

$$I(k) \propto nP(k) \tag{9}$$

where n is the number of particles scattering (in the laser beam at any given moment). Provided one has a monodisperse sample which is sufficiently dilute, measuring the *static* intensity as a function of scattering angle, k, provides a means of determining the single particle form factor. The form factor may be calculated for

isotropic spherical particles, enabling the particle radius to be obtained from the measured static scattered intensity [8]. However, if the particle has an unknown and/or asymmetrical density distribution, or the suspension is polydisperse, difficulties in analytically calculating $P(k)$ can arise, requiring a more complex analysis to obtain useful measurements of particle demension.

For $ka < 1$, Guinier showed that the scattered intensity from a homogeneous distribution of dipole oscillators, independent of particle shape, is given by

$$I(k) \propto \exp(\frac{-k^2 R_g^2}{3}) \tag{10}$$

where R_g is the radius of gyration for the particle and a some characteristic size of the particle [9]. A semilog plot of the static scattering intensity versus k^2 therefore yields a measure of the particles radius of gyration. This result provides at least some quantifying measure for particles of complex structure. For rigid spherical particles, $R_g = \sqrt{3/5}\, a$, where a is now the sphere radius.

The independent averaging of the phase shifts resulting from particle scattering is not possible in suspensions of higher concentration. Here the particles no longer behave independently, with a measure of the suspension structure being given by the pair correlation function, $g(r)$. The pair correlation function yields the probability density of finding a particle a given distance r from a chosen particle center. In calculating the scattered intensity for this case, it is natural to define a function, $S(k)$, termed the static structure factor [10]

$$S(k) = 1 + 4\pi n \int (g(r) - 1)\frac{\sin(kr)}{kr} r^2 dr \tag{11}$$

which arises due to interparticle interactions. The static scattered intensity for an interacting suspension is modified by these interactions and may be written as [10]

$$I(k) \propto nP(k)S(k). \tag{12}$$

For dilute (random) dispersions, $g(r) = 1$ resulting in $S(k) = 1$. In principle, one may therefore obtain $S(k)$ by dividing the measured intensity obtained from a dilute suspension into that measured from a concentrated one. Again, polydispersity complicates the analysis in that the individual phase shifts from each particle are no longer equally weighted.

Dynamic Scattering

Time dependent fluctuations of the scattered intensity also yield information about the suspension. Under the same RGD approximations as above, one may count photons as a function of time, and measure the intensity autocorrelation function, $g_2(k,t)$, where $g_2(k,t) =< I(k,0)I(k,t) > /I^2$. For dilute, independent suspensions undergoing Brownian motion, Gaussian statistics are obeyed and $g_2(t)$ may further be related to the intermediate scattering function (field correlation function), $g_1(k,t)$, where $g_1(k,t) =< E(k,0)E(k,t) > / < |E|^2 >$ as [11]

$$g_2(k,t) = (1 + \gamma|g_1(k,t)|^2) \tag{13}$$

γ an empirical constant depending on the experimental set up. For independent Brownian particles, the particle probablity distribution obeys the diffusion equation. Using the Stokes-Einstein relation for the diffusion constant, D_o, the intermediate scattering function may be written as [11]

$$g_1(k,t) = exp(-D_o k^2 t) \tag{14}$$

where

$$D_o = \frac{k_b T}{6\pi\eta a}. \tag{15}$$

Here, k_b, η, and T are Boltzmann's constant, solvent viscosity, and temperature, respectively. Thus, the correlation in the scattered electric field from any two particles in the suspension, which decays on the time scale of free particle diffusion. By measuring the intensity correlation function, the particle radius, termed the hydrodynamic radius, can be obtained. Often times one does not have a perfectly

rigid sphere or monodisperse distribution, resulting in an effective diffusion constant, D_{eff}. This may be the case if the particles have dangling polymer chains on their surface, or allow solvent penetration through them. Polydispersity leads to a nonexponential behavior for $g_1(k,t)$, which may be accounted for to a limited extent by a cumulant expansion, yielding a measure of the suspensions standard deviation in particle size [11]. These effects can result in the measured hydrodynamic radius being different from the true geometrical radius, or only representative of the dominant size in a distribution.

Experimental

Dynamic and static light scattering measurements were made on dilute suspensions of PMMA microgels, utilizing a Spectra-Physics Argon Ion laser ($\lambda = 514.5$ nm) in conjunction with an ALV-5000 Digital Correlator. Dynamic measurements were made over a range of 25 to 50 degrees in two degree increments. Successive dilutions of one sample in benzyl alcohol, until a stable hydrodynamic radius was obtained, insured the scattering to be in the dilute limit. Static measurements of scattered intensity were obtained for this sample over a range of 20 to 120 degrees, in 0.5 degree increments, yielding the particle form factor.

Results and Discussion

Results from dynamic measurements over all angles yields a average hydrodynamic radius, $R_h \sim 324 \pm 16$nm. In essence, an effective diffusion coefficient is measured and equated to D_o, with the sphere radius as an adjustable parameter. Though not definitive, this is one method of characterizing a particle of unknown structure. A nonswollen hydrodynamic radius of 150 nm was obtained for particles dispersed in water.

From static measurements, a semilog plot of the scattered intensity as a function of the scattering vector, k, is shown in Fig. 2. The large angle plateau ($k > 0.02$ nm^{-1}) is most likely due to the particle structure and near index matching of

the particles and solvent. In the dilute limit, the measured scattered intensity for a sphere drops off rapidly with increasing k, followed by oscillations. The depth of these minima in the oscillations depend on the homogeneity and monodispersity of the suspension. The microgel particles are not optically homogeneous, as solvent penetration into the particle results in a gradual variation in index of refraction between the particle and solvent. This is a possible reason for the reduction in the observed minima at $k \sim 0.02$ nm^{-1}. Also, the relatively weak signal at these larger angles may account for the inability to see any structure at $k > 0.02$ nm^{-1}. Without knowing some information about particle structure apriori, it is difficult to make conclusive statements about the observed static scattering and microgel structure. A Gunier plot of the low angle scattering (inset in Fig. 2) resulted in a radius of gyration, $R_g \sim 211$ nm. The ratio of R_g to R_h is found to be smaller than that for hard spheres ($R_g/R_h = 0.775$) in agreement with previous results for microgel dispersions [12]. Here, a decreased polymer density near the surface of the sphere which would not affect the radius of gyration in a significant way, but would effectively increase the hydrodynamic radius, was attributed to the observed decrease in R_g/R_h over that of hard spheres. If a nondraining core is covered with dangling chains, an increased hydrodynamic radius larger than the physical size of the sphere may be measured. Here, the ratio of R_g/R_h may be expected to be smaller than that for hard spheres. In the case that the particle is penetrated by convecting solvent, the measured hydrodynamic radius is smaller than the swollen size. In this case, since the radius of gyration is determined by the distribution of mass, it is not clear whether or not the ratio of R_g/R_h would appear smaller than that expected for hard spheres.

By comparing the volume fraction calculated from the known dried weight of particles to the effective volume fraction measured via the intrinsic viscosity, a ratio of swollen to nonswollen volumes may be calculated. For the suspensions examined here, this ratio is found to be nearly 18. Comparison of the swollen hydrodynamic radius obtained via dynamic light scattering, with that calculated from the nonswollen radius and the swelling ratio, indicates agreement between

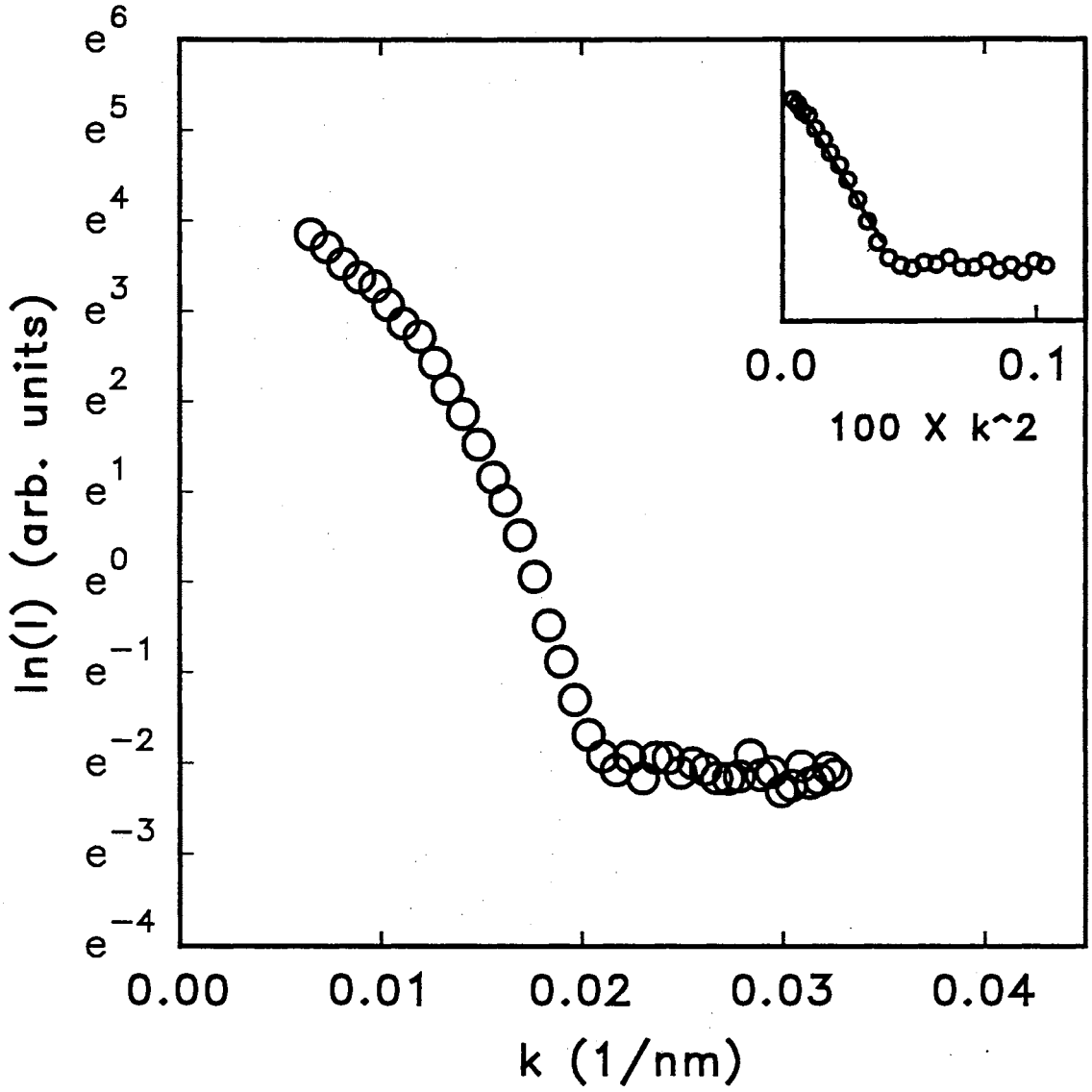

Figure 2. Ln of intensity versus scattering vector, k. Ln of intensity versus k^2 (Inset), to which the linear fit shown at low angles results in R_g = 211 nm.

the two radii to within $\sim 20\%$. Since the two radii show a reasonable amount of agreement and the microgels show qualitative hard sphere like equilibrium behavior (see Chapter III), it is assumed that the particles are essentially nondraining at a given concentration, with a decreased polymer distribution near the surface which may drain and deform on contact with other particles. However, the extent of deswelling with increased concentration is not known.

CHAPTER III

EQUILIBRIUM PROPERTIES

Introduction

The recognition that the material comprising the earth is made of "stuff" which can transform back and forth between fluid, solid and gas is rooted in antiquity. The most inspiring transitions are between the fluid to solid, particularly crystalline solid, phases. The unique patterns of ice crystals, or on a larger scale, the spectral iridescence found in opals are a result of the long ranged positional order of the materials atoms or particles [13]. Suspensions of the Tipula Iridescent Virus provided some of the earliest evidence that solutions of uniform microscopic particles could exhibit polycrystalline behavior [14,15] With the accidental production of uniform, micron sized latex spheres in 1947 [16] and the subsequent developement of the process, monodisperse suspensions of differing size, composition and surface chemistry have become readily available for investigation, stimulating research of both equilibrium and nonequilibrium phase transitions.

The study of equilibrium properties of well characterized suspensions provides insight not only for the behavior of more complex systems such as blood or paints, but also atomic and molecular systems, for which they serve as models. By treating the fluctuating fluid background of a colloidal system as a mean field, a pair potential for the particles can be defined, analogous to the effective pair potential found in atomic systems [17]. This essentially allows a degree of correspondence between atomic and collodial systems. However, the correspondence is not one to one. For example, a typical suspension will have a number density about 10^9 smaller than that found in an atomic solid. Since the strength of a material is approximately proportional to the number density [17], colloidal structures are 9

orders of magnitude weaker than similar atomic structures. This is easily observed by tipping a cuvette of charge stabilized polystyrene spheres which have undergone the fluid/solid transition. The suspension easily flows, destroying the crystallites.

Since the advent of uniform colloidal particle synthesis, the order/disorder transition for purely repulsive and fluid/solid transition for weakly attractive potentials has often been observed [18–20,22,23]. There are two obvious areas of study concerning such phase transitions: What governs the the crystals formation and growth, and once formed what are its structure and properties. The former is presently an area of discussion, and amenable to modified classical theories of crystallization [24,40–42] The latter can be characterized via light scattering and linear elastic measurements.

In this chapter, the equilibrium phase behavior of PMMA microgels is examined and compared with previous hard sphere data. Although thermodynamic properties such as an equation of state can be defined for a suspension (i.e. van't Hoff's Law) [17], the aim of the present examination is to illustrate where the transition occurs in particle concentration, and with what equilibrium structure the crystallization manifests itself. Visual observation and Bragg (powder) scattering measurements were made on the suspension in order to achieve this goal. The dynamics of crystal growth in these suspensions is left as future work.

Computer simulations predict an order/disorder transition as a function of volume fraction for particles with a hard sphere interaction. Here, the freezing and melting point volume fractions are found to be $\phi_f = 0.494$ and $\phi_m = 0.545$, respectively [25,26]. A phase transition at these volume fractions subsequently was observed in suspensions of charged stabilized spheres at high ionic strength [27]. More recently, sterically stabilized suspensions have been found to undergo this transition, the freezing and melting point volume fractions also in near agreement with simulation results [20,21].

Computer simulations for atomic systems have shown that crystallization kinetics is greatly dependent upon the steepness of the pair potential [28], while Monte Carlo studies of spheres interacting via a $1/r^n$ type repulsive potential,

indicates a decrease in the fractional density change on melting with decreasing n [29,30,32]. Modified approaches to Rowlinson's hard sphere perturbation method [35] result in agreement with simulation results [36,37], where density functional theory has met with less success [33,34].

Kose and Hachisu (1974) observed phase separation into ordered and disordered states in crosslinked PMMA spheres swollen in benzene [23]. The spheres were swollen to approximately 3 to 6 times that of their dry volume. The freezing point effective volume fraction, obtained by scaling the nonswollen volume fractions with the ratio of swollen to dry particle volumes, was found to be $\sim$ 50%. However, their effective volume fractions are in error due to partial dissolution of the particles, resulting in the presence of free polymer. The addition of free polymer has been demonstrated by Wolfe to result in particle deswelling in microgel dispersions [38], making the comparison of Kose and Hachisu's freezing point effective volume fraction with that of simulation results for hard spheres difficult. Examination of the ordered phase iridescence led Kose and Hachisu to the conclusion of crystallite structure being face centered cubic (fcc).

Smits (1990) has examined index matched sterically stabilized silica dispersions in which the steepness of the interparticle potential could be varied via the stabilizing layer [39]. Here, light scattering measurements on the crystalline phase yielded possibly random stacked hexagonal close packed (hcp) planes for the samples with steepest interparticle potentials. Those with softer potentials resulted in either fcc, hcp or mixtures of fcc and hcp crystal structures.

Equilibrium Phase Diagram

Experimental

In an effort to examine equilibrium phase behavior, a series of ten 8cc vials were prepared. Weighed vials were partially filled with premixed, highly concentrated ($\phi^* > 1$) microgel suspension. By keeping track of the weight of added benzyl alcohol, each vial could be diluted until the desired concentration was achieved.

In this way, samples were prepared at effective volume fractions of $\phi^* = 0.503$, 0.514, 0.524, 0.535, 0.548, 0.557, 0.566, 0.582, 0.599, and 0.612. The vials were sealed with screw tops and parafilm, tumbled overnight to homogeneously mix the solvent and microgel, and left to stand undisturbed for observation.

With incandescent back lighting of the vials, the heights of phase separated regions could be examined. A telescope equipped with a horizontal retical and mounted on a vertical translation stage, capable of resolving vertical displacements to within 0.005 cm, enabled determination of the colloidal liquid and crystal interface.

Results

Detailed nucleation times were not obtained. However, the rate was on the order of days. Within $\sim$ 82 hours, the $\phi^* = 0.599$ sample appeared iridescent as if fully crystalized with very fine crystals, although no graininess could be observed with the eye, and the $\phi^* = 0.582$ sample exhibited sparse nucleation in the bulk colloidal liquid. The sample of largest volume fraction, $\phi^* = 0.612$, as well as all samples of $\phi^* < 0.582$, showed no crystallization at this time.

At 70 days, the sample at $\phi^* = 0.612$ still showed no crystallization and is termed glassy. However, a few crystallites were observed in the meniscus, presumably due to shear ordering from countertop vibrations. Samples of $0.582 \leq \phi^* \leq 0.599$ appeared fully and homogeneously crystallized, with crystallite size being markedly smaller at $\phi^* = 0.599$ than lower effective volume fractions. A coexistence region from $0.548 \leq \phi^* \leq 0.566$ was observed, with sedimentation of crystallites out of the bulk suspension, leaving a crystallite depleted region of suspension above. For samples $\phi^* \leq 0.535$, liquid like behaviour was found, with no crystallization observed, even after a period of greater than one year. No clear supernatant was observed in any of the ten samples at any time, indicating near density matching between the swollen particles and benzyl alcohol. By measuring the ratio of crystal sediment height to total sample height, a percent crystallization could be calculated for samples in the coexistence region, and an equilibrium phase

diagram constructed as shown in Fig. 3. Here L, C, X and G correspond to liquid, coexisting, fully crystalline and glassy regions, respectively. The freezing and melting points are found, via linear regression through points in the coexistence region, to be 0.548 and 0.573, respectively.

Powder Pattern Scattering

Experimental

Scattering results were obtained using HeNe laser with the beam expanded to approximately 1cm in diameter and made to pass through a cylindrical lens. The beam was made incident upon the sample placed in the center of an index matching bath of benzyl alcohol and the cylindrical lens adjusted relative to the bath such that the incident wave vector was parallel to the detector plane. The index bath was used as a cylindrical lens, focusing the scattered light onto a focal plane, at which a vertical slit and diffuser plate were placed. Light incident upon the diffuser plate was transmitted through an optical fiber to an RCA photo-avalanche diode. The collection optics were mounted on a goniometer which could be stepped in 0.25 degree increments. Computer control allowed for the collection of intensities as well as goniometer control. The sample vial was rotated at 0.5rpm and intensity data collected for a period of not less than 2 minutes at each angle, to insure proper orientational averaging of the crystallites. For the liquid and glassy phases, rotation of the sample was not necessary.

Results

The results for measured intensity versus k, typical of samples in the liquid, coexisting, fully crystalline and glassy regions of the phase diagram are shown in Fig. 4. The profiles exhibited by samples in the coexistence and fully crystalline regions of the phase diagram are shown in (c) and (d), respectively. The insets show the highest order peak measured. Small oscillations in the data are due to drift in the laser output intensity and the 'peaks' at $k > 0.018$ nm^{-1} due to

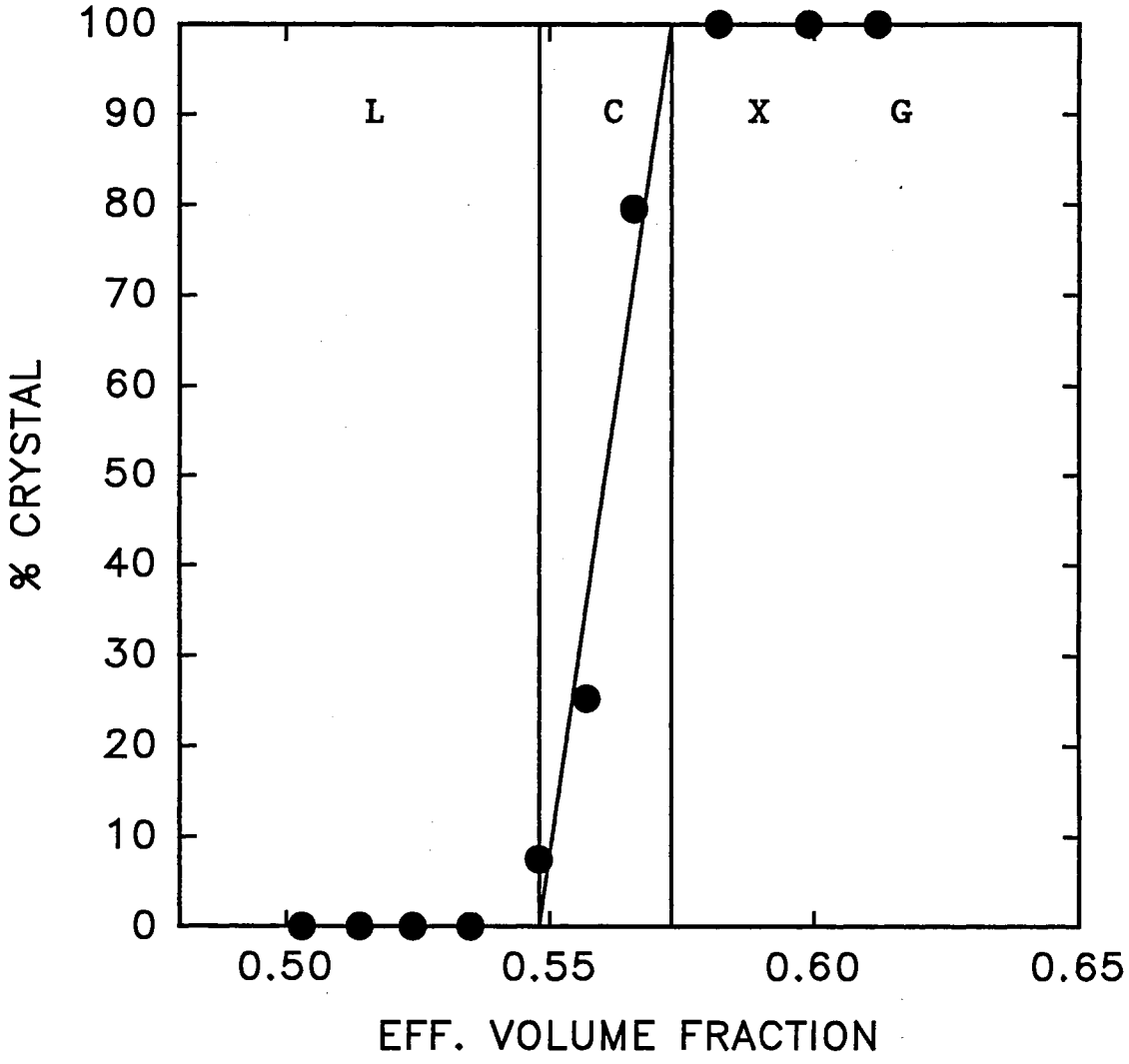

Figure 3. Equilibrium phase diagram for microgel suspension. L, C, X, and G indicate liquid, coexisting, fully crystalline, and glassy regions, respectively.

back reflections from the index bath. These results are nearly identical to those measured in the equilibrium crystal of hard sphere suspensions.

Discussion

Equilibrium Phase Behavior

The coexistence region for the PMMA microgels is greatly narrowed, as well as shifted in effective volume fraction compared to the simulation results for the freezing/melting transition in hard sphere suspensions of $\phi_f = 0.494$ and $\phi_m = 0.545$, respectively. It is possible, that due to particle deswelling with increased concentration, the assumed swollen particle radii are in error to the actual radii, thus shifting the measured freezing point volume fraction above that of hard spheres. A decrease in the swollen radius of $\sim 3.4\%$ would bring the microgel freezing point coincident with that of hard spheres. However, this does not explain the narrowing of the coexistence region. Although some deswelling may occur with increased concentration, it is believed that this narrowing is an indication of a soft interparticle potential compared to that of hard spheres.

Comparing ϕ_f^* with that obtained from computer simulation results for spheres interacting via a $1/r^n$ type potential, where $n = 4, 6, 12$, and ∞, yields an estimate of the interparticle potential. As shown in Fig. 5a, a polynomial fit to $1/n$ versus ϕ_f obtained from the simulations, results in $n \sim 20$ for the microgels examined here [29–32]. The error bars indicate the value of $1/n$ for $n = 20 \pm 5$. The value of n and the fractional density change upon melting, $(\phi_m^* - \phi_f^*)/\phi_f^*$, defines another point which can be compared with the simulation results as shown in Fig. 5b. As can be seen, the fractional density change upon melting for the microgels compares well with estimated simulation results for $n = 20$. The softness of the interaction is presumably due to the deformation of a polymer density distribution near the surface of the particle. In this sense, the particles are deswelling at their point of contact due to deformation.

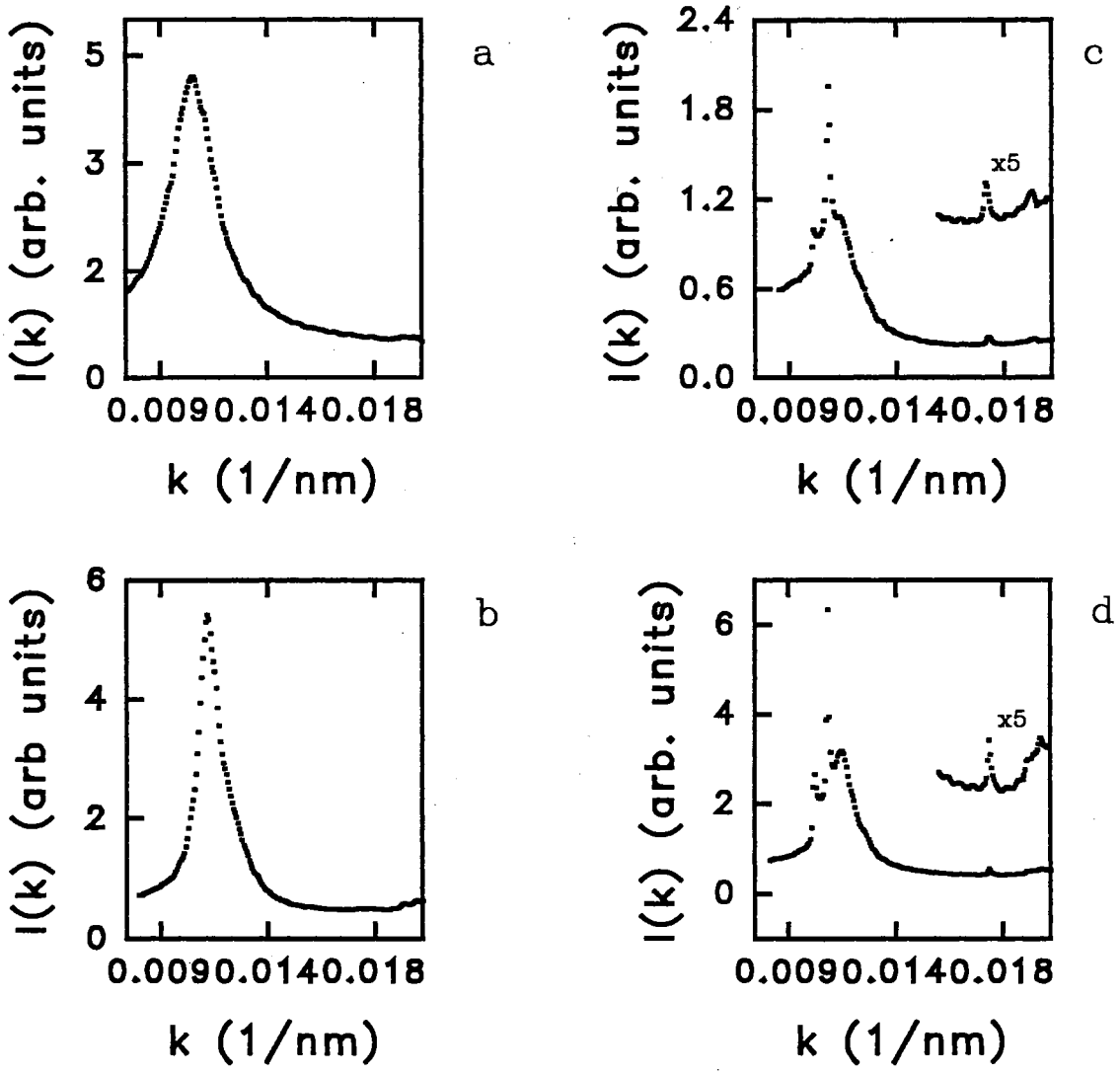

Figure 4. Powder diffraction patterns measured for microgel samples in the (a) ($\phi^* = 0.503$) liquid, (b) ($\phi^* = 0.612$) glassy, (c) ($\phi^* = 0.566$) coexisting, and (d) ($\phi^* = 0.582$) fully crystalline regions of the equilibrium phase diagram. Insets in (c) and (d) show the highest order peak measured on an expanded scale. See text for details.

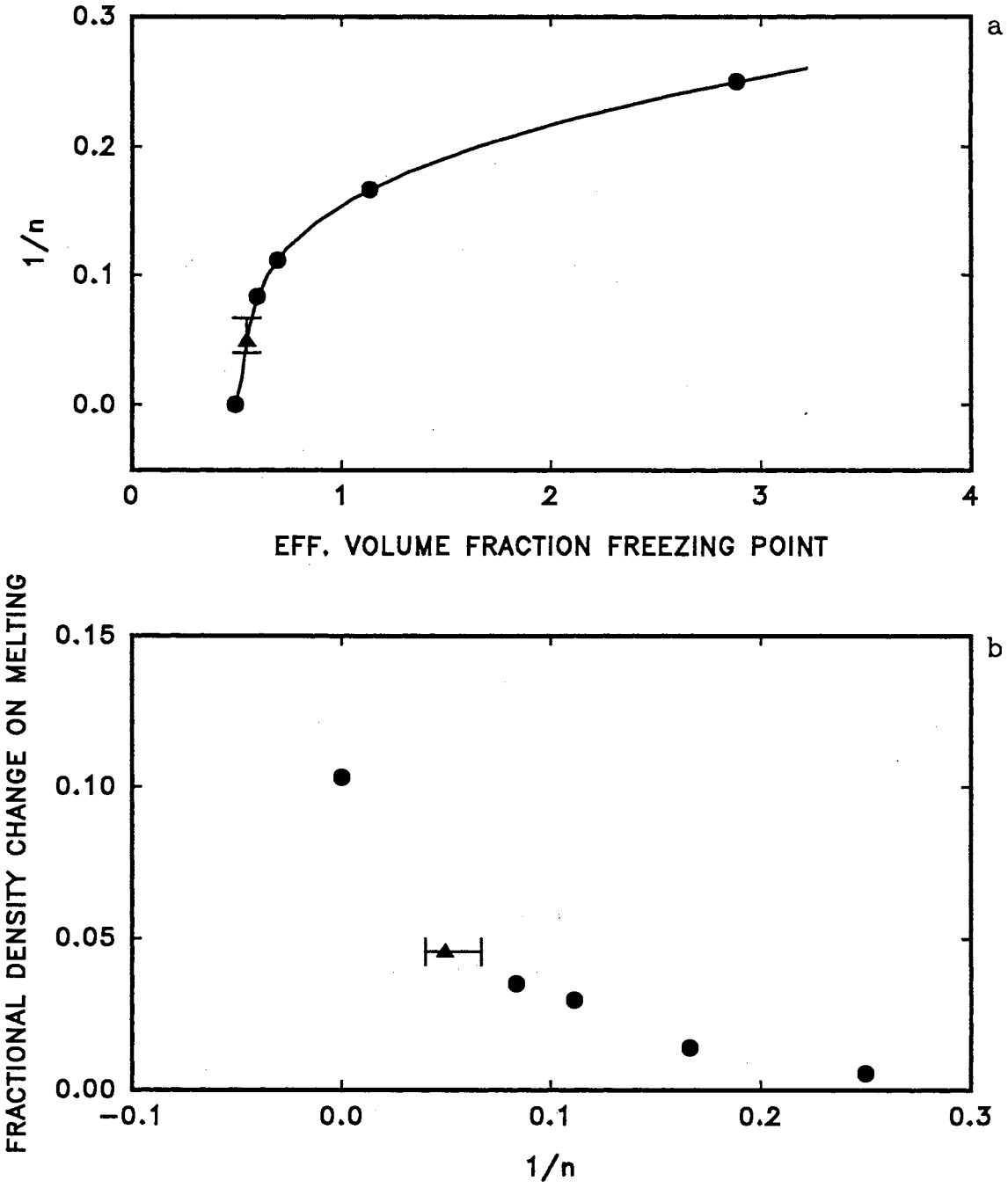

Figure 5. (a) Freezing point effective volume fraction obtained for suspensions interacting via a repulsive $1/r^n$ type potential versus $1/n$, (b) Fractional density change upon melting versus $1/n$. ● simulation results, ▲ this study. The error bars associated with the data of this study assume $n = 20 \pm 5$.

Wolfe [7] has observed frequency independent, roughly power law behavior in the dynamic storage modulus, G', versus ϕ^* for microgel suspensions at high concentrations (see Chapter VI for definition of the moduli). In Fig. 6, the data of Wolfe for the same particles examined here, is shown along with the dynamic moduli measured in this study. Here, the storage modulus obtained by Wolfe versus effective volume fraction is shown as $\bigcirc$, $\bigtriangledown$, and $\square$ for $\omega = 0.1$, 1.0 and 10 rad/sec., respectively. The data of this study is represented as $\bigtriangleup$ and $\diamond$ for $\omega = 0.63$ and 6.3 rad/sec., respectively. A passing note here, to be discussed in more detail in Chapter VI, is that the 'global' microstructure as observed in light scattering, does not appear to have a large effect on the equilibrium dynamic storage modulus. While underlying microstructure was not an issue for the data of Wolfe, it is important for the present study. The open symbols represent measurements made on initial microstructural state in which the closest packed direction of an hcp plane was directed along the velocity direction. The closed symbols are for initial states where the closest packed direction is aligned parallel to the vorticity axis (see Chapter IV for details of the shear induced microstructures). This observation aside, for $\phi^* \geq 0.758$, the data shows the storage modulus is roughly frequency independent over the range examined. Such independence is indicative of an elastic response in the suspension, in which the frequency used to probe the suspension is faster than some viscous relaxation time associated with the system. Buscall, et al. [80] derive an expression for the equilibrium storage modulus based on the interaction potential between pairs of particles as

$$G_o = \frac{\beta}{r}\left(\frac{\partial^2 V}{\partial r^2}\right) \tag{16}$$

where r is the center to center to center separation between particles, and β a constant related to the number of nearest neighbors associated with the details of the microstructure. The interparticle distance in a suspension of spheres, r, may be related to the closest packed volume fraction as

$$r^3 = d^3 \frac{\phi_m^*}{\phi^*} \tag{17}$$

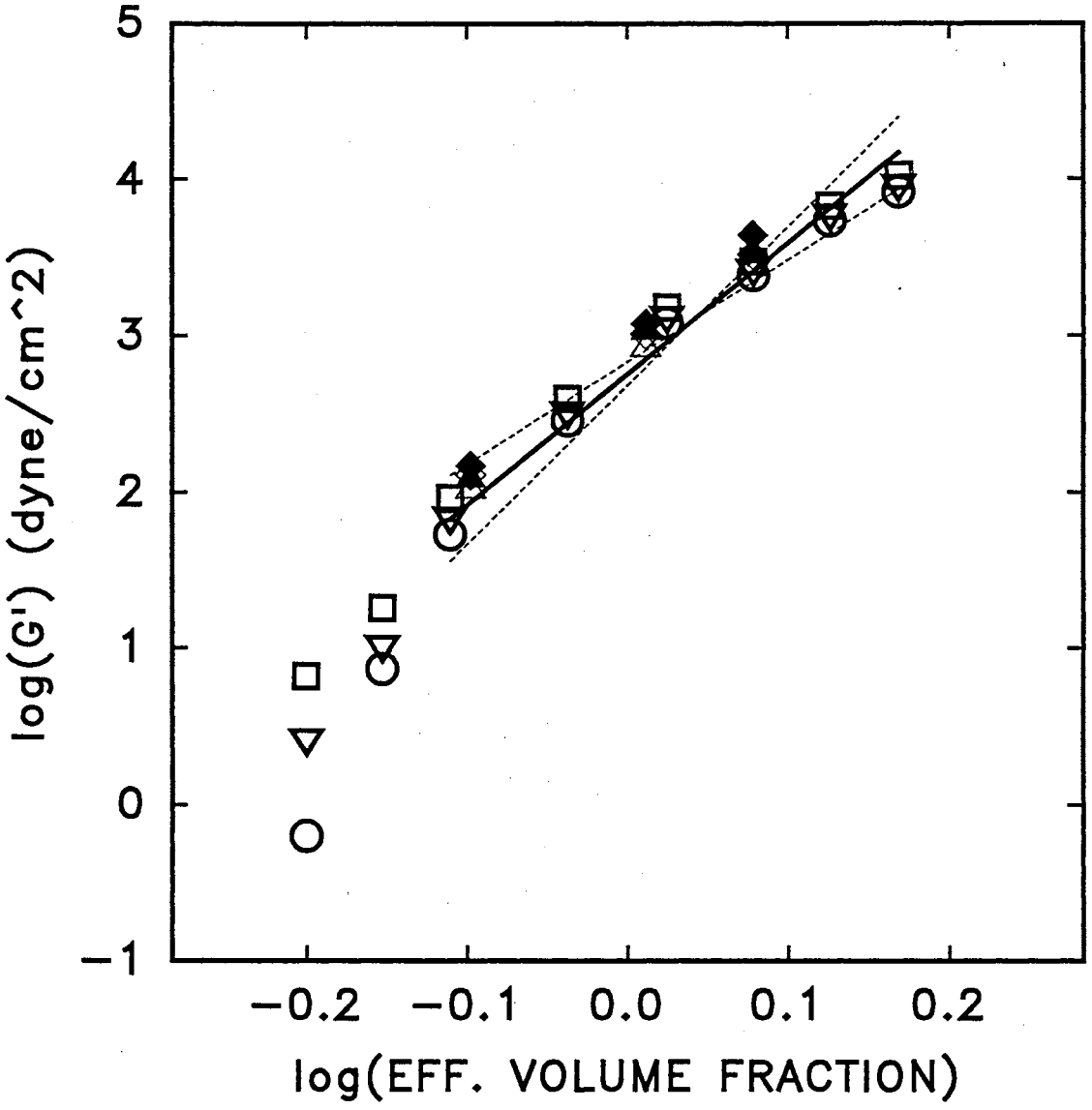

Figure 6. log(G') versus log effective volume fraction showing observed power law dependence in the data of Wolfe at frequencies of ◯ 0.1, ▽ 1.0, and □ 10 rad/sec. The data of this study is represented as △ and ◇ for $\omega = 0.63$ and 6.3 rad/sec., respectively. Filled and open symbols represent different microstructures (see text). Solid line is a linear fit for $G' \propto \phi^{*m}$, where $n = 3(m-1) = 20$. Dashed lines indicate $n = 15$ and 25.

where d is the sphere diameter and ϕ_m^* the closest packed volume fraction. Examination of the above two equations in relation to the assumed form of the interaction potential for the microgels, $V \propto 1/r^n$, yields

$$G_o \propto \phi^{*m} \tag{18}$$

where $m = (n/3) + 1$ is a power law exponent. For qualitative purposes, d and ϕ_m^* have been absorbed into the proportionality constant. Assuming the dynamic storage modulus of Fig. 6 to be exhibiting roughly power law behavior, this result may be used as an independent means of checking the relevancy of $n \sim 20$. Setting $3(m-1) = 20$ yields $m = 7.7$. The results of using this exponent is given by the solid straight line shown on Fig. 6. The $\phi^* = 0$ intercept was used as an adjustable parameter. Given the limitations of the above derivation, such agreement may seem fortuitous. Since Eqn. 16 is derived under the assumption of no viscous relaxation, G_o represents the high frequency limit of G', usually observed as a frequency independent plateau. It is possible that the observed frequency independent G' for the microgels is not the high frequency limit, but due to some intermediate relaxation time much slower than that associated with $G'_{\omega=\infty}$. It is interesting to note that power law behavior in G' has previously been observed in flocculated dispersions [81]. For comparison, the dashed lines indicate $3(m-1) = 25$ and 15.

Equilibrium Crystal Structure

Results for the powder pattern scattering from samples which exhibit crystallization appear nearly identical to those previously found in sterically stabilized PMMA hard sphere suspensions [43]. Here, the powder pattern profiles are explained as random stacked, hexagonal close packed planes. Starting with a single initial hcp plane with a particle labeled A, there are two choices for the next layers registration, B or C (see for example Fig. 11). In this way, an fcc crystal structure can be built with a stacking sequence ABCABC... or ACBACB..., and hcp crystal structure as ABAB... or ACAC.... Letting α denote a stacking probability, where $\alpha = 1$ results in fcc stacking and $\alpha = 0$ hcp stacking, purely random

stacking (ABCBCA...) is given by $\alpha = 0.5$. As described in Chapter II, the scattered intensity, $I(ka)$, is a product of a particle form factor and structure factor, $I(ka) = P(ka)S(ka)$. Solvent scattering being negligible, the scattered intensity obtained from a dilute suspension, where $S(ka) = 1$, yields $P(ka)$. Typically, the particle form factor is assumed independent of particle concentration. However, the degree to which the particle form factor varies with concentration due to deformation of the microgel particles, as well as multiple scattering effects, is not known. Therefore, the dilute scattered intensity shown in Fig. 2 is not suitable for dividing the particle form factor out of the measured intensities. It is likely some deviation occurs, making detailed analysis of structure factors relative to hard spheres suspect. However, a qualitative comparison can be made at relatively low angles. Fitting the measured intensity shown in Fig. 2 with a polynomial, allows the structure factor to be extracted from the measured powder pattern results. Following the same procedure as outlined in ref. [43], and described in Appendices A and B, calculated structure factors are compared to measured results for samples in the coexisting and fully crystalline regions of the equilibrium phase diagram. A Lindemann ratio of $\sim 14\%$ was used, which is consistant with a slightly soft interparticle interaction [33]. The crystallite size was estimated to be ~ 20 to 30 μm based on the half width of a gaussian fit to the central peak (indexed to the [111] direction for an fcc crystal).

A comparison of these calculations with the measured data is shown in Fig. 7a and 7b (samples c and d of Fig. 4, respectively). Agreement with calculated profiles is found to be quite good. Here, a stacking probability of $\alpha = 0.52$ was found for Fig. 7a, a sample in the coexisting region of the phase diagram. This indicates a slight tendency for fcc, and is consistent with the results of sterically stabilized, hard sphere like suspensions [43]. The longer nucleation times associated with the coexistence region is a possible reason for this tendency, as the particles have a longer time to find a favorable lattice position. A purely random stacking, $\alpha = 0.5$, was found for the fully crystallized sample shown in Fig. 7b. It should be noted that deviations at small angles is assumed due to the simple

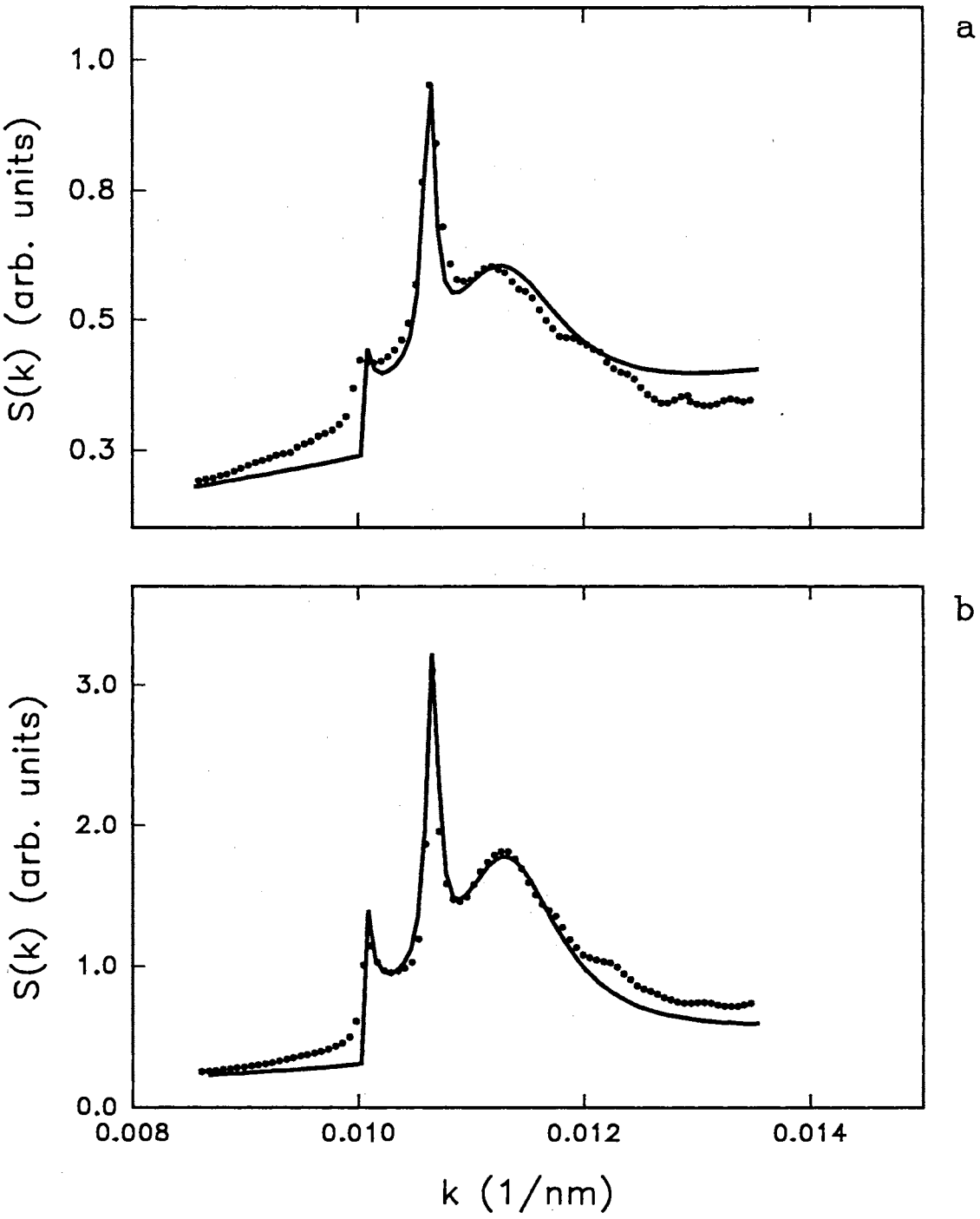

Figure 7. Calculated structure factors for crystallites composed of random stacked hard spheres compared to that measured for microgel samples in the (a) ($\phi^* = 0.566$) coexisting, and (b) ($\phi^* = 0.582$) fully crystalline regions of the equilibrium phase diagram. ● experimental, – theory.

independent oscillator model used to account for thermal motion, which does not take into account correlated particle vibration. The deviations at higher angles is attributed to use of the dilute limit particle form factor and multiple scattering effects. Although these deviations are present, the excellent agreement in peak positions should be noted. The ratio of the [111] peak position to the position of the highest order peak measured (shown as insets in Fig. 4c and d) agrees to within $\sim 4\%$ of the ratios obtained from their calculated profiles. Polydispersity effects have been neglected, although we note that the observed crystallization indicates the polydispersity to be less than 10%, due to the instability of colloidal crystals at larger polydispersities [17].

CHAPTER IV

NONEQUILIBRIUM PHASE BEHAVIOR

Introduction

As already noted, the characteristic particle size of colloids generally allows probing of microstructure with visible light or neutrons. However, microstructurally perturbing shear rates, $\dot{\gamma}$, can also be experimentally realized and applied. This makes colloidal suspensions unique in the ability to examine nonquilibrium microstructure while under applied shear. Under applied shear, hydrodynamics and the competition between hydrodynamics and thermal motion results in a complicated interplay between fluid and particles within a suspension. Here, the Péclet number, defined as $Pe = \dot{\gamma} l^2 / D_o$ where l is a characteristic length of the particles and D_o the free diffusion constant, indicates the relative importance of diffusive to convective time scales. Since it is the thermodynamic driving force which relaxes the system to equilibrium, and convection which perturbs the equilibrium, the Péclet number gauges the systems departure from equilibrium. Configurational relaxation times for atomic and molecular systems is rapid enough, unlike colloidal systems, that experimentally unobtainable shear rates would be needed to probe this departure. Also, in concentrated dispersions, long lived metastable states can be induced which may be examined in their unique state (the measurements of Chapters V and VI, for example). Finally, since colloidal suspensions mimic atomic systems, observations made on them may qualitatively describe the dynamics of atomic system which are not directly observable [48]. However, caution is due in part to the lack of hydrodynamic interactions in atomic systems.

In this chapter, the scattered intensity from concentrated suspensions of microgel particles is examined. Here, microstructure is examined under the influence

of applied oscillatory shear as a function of concentration, frequency, and amplitude, with no regard for measuring the stress. These results are interpreted relative to hard sphere behavior and on geometrical grounds, rather than more sophisticated theories [46]. An exploratory examination of Bragg spot position and intensity as a function of applied shear stress in steady state flow will also be presented. A more detailed connection between rheology and microstructure is discussed in Chapters V and VI.

There have been a number of attempts to correlate microstructure and rheology by connecting the applied shear to bulk stresses in the suspension, via a constituitive equation. These efforts have been two fold. Based on the early work of Batchelor [50–54] and further effort of Felderhof [55–57], Russel [58,59], and Wagner [60], theories have been devised which connect bulk rheological properties, such as shear viscosity, to suspension microstructure. Due to the complications of many body hydrodynamics, success has generally been only in the vanishing shear rate limit of concentrated suspensions or the dilute limit. Analytic examination of the shear rate dependent structure factor has been used to connect microstructure with the experimentally observed distortion of Debeye-Scherer ring under applied shear [61–71]. However, experimental complications due to multiple scattering effects and analytic complications at increased concentrations have circumvented a complete solution. If the suspension is sufficiently concentrated, equilibrium crystallites may form and have been observed to shear melt under applied shear [72]. Further, long range structure may develope under applied shear, evidenced as a collapse of the Debey-Scherer ring into Bragg peaks [73–76,46,77,78,39,1]. The formation and evolution of such shear induced structure is presently not well understood.

A second method of approach is through computer simulations. Here, both particle "snapshots" and bulk properties can be simultaneously obtained. Simulations provide a means of examining the induction and evolution of shear ordered structures along with the ability of probing microstructure in regions unaccessible to experimentation. However, the cost of including N-body hydrodynamics in a

simulation of Brownian particles leads either to their neglect or small simulation sizes limited to two dimensions [79].

Nonequilibrium Phase Diagram

Experimental

Light scattering measurements of PMMA microgels while under applied shear were made with the scattering geometry as shown in Fig. 8. Here, $\vec{k_i}$ and $\vec{k_s}$ represent the incident and scattered wave vectors, respectively. $\vec{\Omega}$ is the vorticity, $\vec{\Delta}$ the shear and $\vec{v}$ the velocity directions. With passage of Helium Neon beam ($\lambda = 632.8$nm) through the center of the shear cell and perpendicular to the axis of rotation, small scattering vectors, $\vec{k_i} - \vec{k_s}$, probe the $\vec{v}\vec{\Omega}$ plane. Immersion of the cell in a square glass box filled with glycerin provided index matching, allowing scattering from the couette to be imaged directly on a flat screen placed perpendicular to the incident beam. With this design, the diffuse Debye Sherrer ring associated with liquid like structure as well as Bragg spots to first order could easily be monitored. The couette cell used was made by machining a glass plunger with a uniform 250μm step cut into the bottom 2 cm, to fit into a 20 ml glass syringe. This allowed for loading of the cell by injecting the suspension through the bottom of the syringe, filling the gap. A single drop of benzyl alcohol placed at the top of the cell, between the plunger and syringe wall, was used as a seal between the sample and air, as well a lubricant for the plunger/syringe interface. A computer controlled stepper motor capable of 25000 steps/rev. was used to rotate the plunger in an oscillatory fashion.

Structural studies for the microgels consisted of measurements in which samples were subjected to a shear oscillation of fixed frequency throughout a range of amplitudes. Here, the amplitude is reduced by the width of the couette gap and results reported as strain amplitude. Each oscillatory measurement was conducted for a period of five minutes, at which point most samples appeared by eye to have

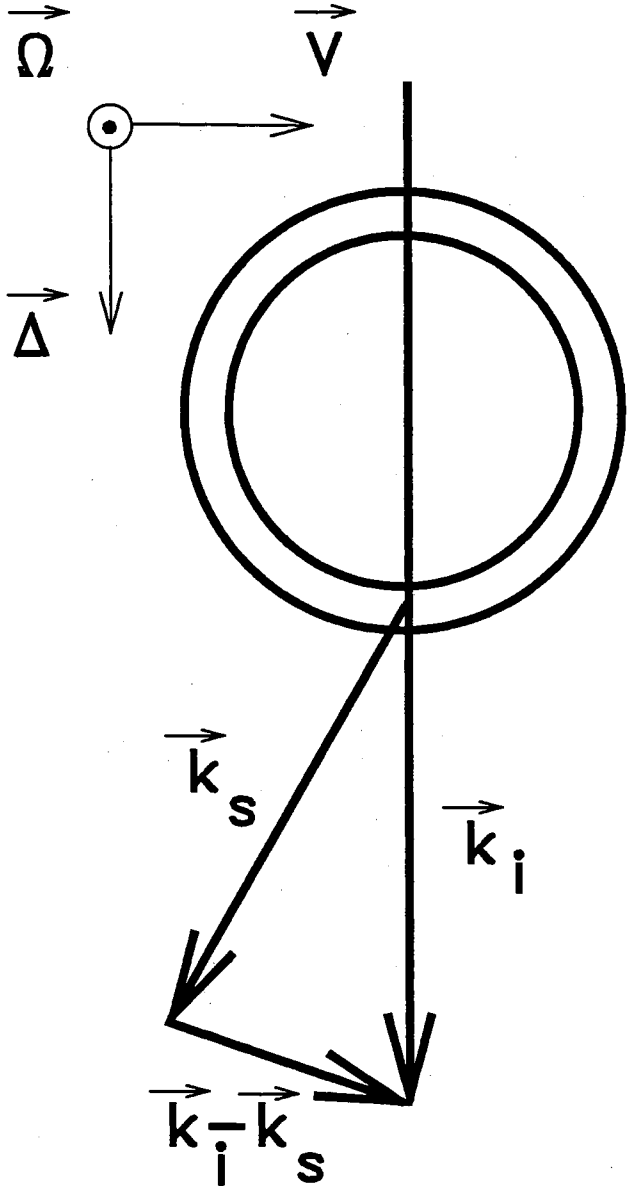

Figure 8. The scattering geometry showing the incident beam normal to the axis of rotation. Here $\vec{k_i}, \vec{k_s}$ and $\vec{k} = \vec{k_i} - \vec{k_s}$ are the incident, scattered and scattering wave vectors, respectively. $\vec{\Omega}$, $\vec{\Delta}$, and $\vec{v}$ represent the vorticity, shear, and velocity directions in the scattering volume, respectively. Note, the $\vec{\Omega}\vec{v}$ plane is probed at small scattering angles.

fully evolved into a definite microstructural state. Samples of concentration coincident with the equilibrium phase diagram were measured at frequencies of 1 Hz and 4 Hz, over a range in strain of 0 to 16.

Results and Discussion

The oscillatory shear measurements made on the microgels yield essentially the same results as observed in hard sphere like suspensions of sterically stabilized PMMA. At effective volume fractions greater than ϕ_f^*, shear ordering of the microgel suspensions, qualitatively similar to that found for hard spheres, has been observed. Previous experimental studies [76,46] for hard sphere suspensions have indicated and determined five basic types of microstructures associated with shear flow: amorphous, registered random stacked hexagonal planes, fcc, sliding layer, and string. With the exception of the string structure, the measured scattered intensity distributions for the microgels under applied oscillatory stress are as indicated in Fig. 9a-9f. Samples of effective volume fraction less than the freezing value ($\phi_f^* = 0.548$), exhibited only amorphous ordering. Such a correlation has been observed by Ackerson and Pusey in sterically stabilized hard sphere suspensions [46]. It is interesting to note that the equilibrium freezing point concentration for the microgels was initially determined from this observation. The results for all samples measured are shown in Fig. 10a and 10b, where the structures associated with 5 minutes of oscillation are given as a function of strain amplitude and effective volume fraction. Here (◆) is amorphous, (◯) face centered cubic, (□) sliding layer, (△) mixed fcc and sliding layer structures, (◒) amorphous/fcc, (⬓) amorphous/sliding layer, and (◭) amorphous/mixed fcc and sliding layer structures. The ordering of structures, separated by /, indicates the prominent order with which they appeared in the scattering.

The registered random stacked structures consist of planes of hexagonally close packed particles aligned parallel to the cell walls (the $\vec{v}\vec{\Omega}$ plane) such that a closest packed direction within the layer is parallel to $\vec{v}$. The slippage of planes over one another in a shear flow results in a registered random stacking of these

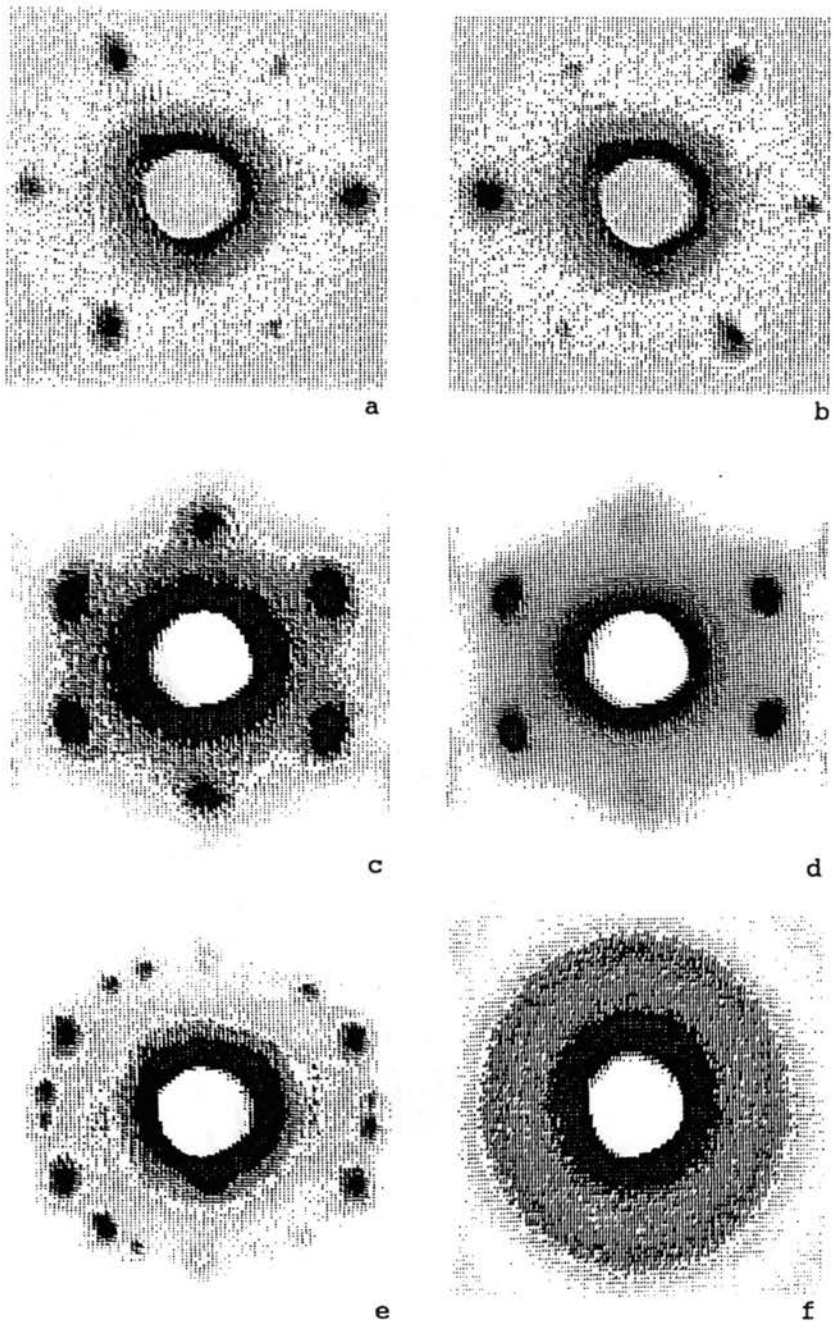

Figure 9. Observed scattering patterns, from microgel suspensions, imaged on a screen. Induced structures are identified as (a), (b) fcc twin structures, (c) random stacke hcp, (d) sliding layer, (e) mixed fcc and sliding layer, and (f) amorphous structures.

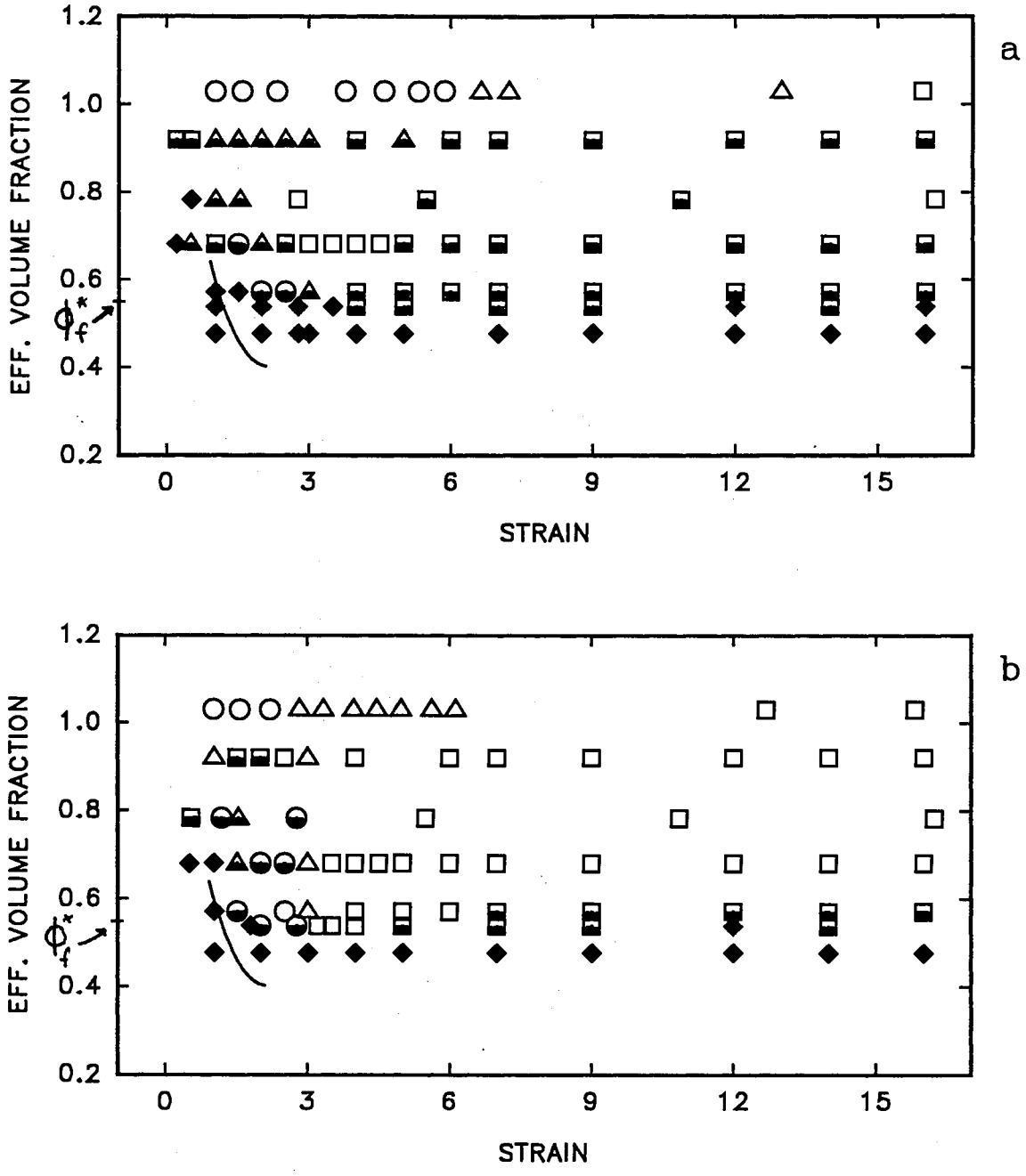

Figure 10. Measured nonequilibrium phase diagrams for microgel suspensions. Here, (◆) is amorphous, (○) fcc, (□) sliding layer, (△) a mixture of fcc and sliding layer structures, (◒) amorphous/fcc, (⬓) amorphous/sliding layer, and (▲) amorphous/mixed fcc and sliding layer. The order of structure listed for each symbol is the order of prominence with which the structure was observed. (a) 1 Hz., (b) 4 Hz. results. The solid curve represents a geometrical hard sphere boundary, above which an fcc state evolves into a mixed structure. - indicates the freezing point.

planes. This corresponds to a stacking sequence shown in Fig. 11a, where the first plane is positioned with a particle at A. Neighboring planes may be registered at positions B or C. In a random stacking, either choice is equally likely, giving a random (ABCBCA...) sequence. The sequence for a hexagonal close packed crystal is ACAC... or ABAB..., while an fcc crystal is ABCABC... or ACBACB.... At large shear rates or strain amplitudes, the sliding layer structure is observed, where the planes of hexagonal close packed particles no longer register with one another, but are found along paths located halfway between registration sites as indicated by the dashed line in Fig. 11a. The centering of layers diminishes the intensity of the six fold symmetric spots lying on the Ω axis. At the largest strain amplitudes, the hexagonal close packed planes of particles break up into strings of particles regularly spaced in the $\vec{v}$ direction.

In the fcc structures, the planes of hexagonal close packed particles aligned parallel to the cell walls are oriented with a close packed direction parallel to Ω rather than to $\vec{v}$, as shown in Fig. 11b. This orientation could be achieved in two ways. Manually pulling the rotor up and down a fraction of a millimeter was enough to drive the system to fcc ordering. This was done in preparing the initial state for the $\phi = 1.03$ sample, as a return to the amorphous state was not possible once structure had been introduced. The $\phi^* = 0.92$ sample was observed to order into a weak fcc structure upon injection of the suspension into the couette (presumably due to the vertical injection). Although made as amorphous as possible prior to each run, this sample evidenced sliding layer structure within a few cycles of applied oscillation, indicating residual order prior to the run. The suspensions could also be driven from an amorphous into an fcc state via the 1 and 4Hz oscillations of the plunger, as shown in Fig. 10a and 10b. This ordering is usually not as strong and is accompanied by more amorphous scattering than that induced from vertical movement of the plunger. The cause of this oscillatory transition from amorphous to fcc is not obvious. The fcc orientation of layers only permits homogenous shear deformation for a limited range of starting amplitudes. The largest strain amplitudes are produced by ABCABC... or ACBACB... stacking, fcc

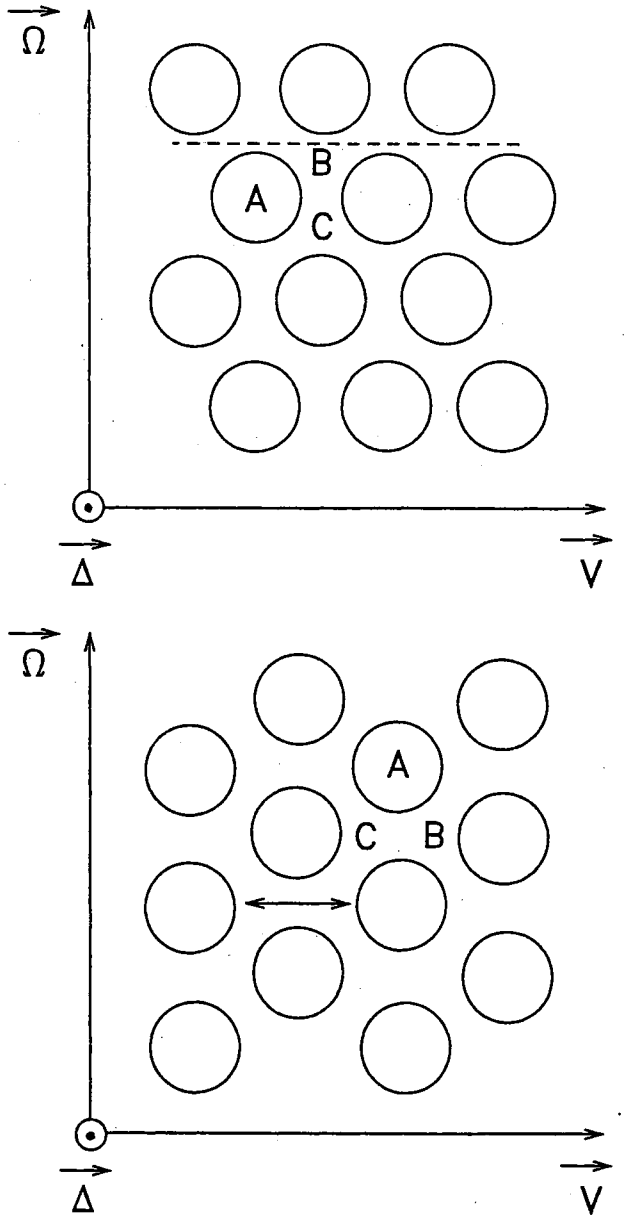

Figure 11. (a) Layering of close packed hexagonal planes within the shear cell gap. As shown, the stacking of planes is in the shear direction. Here the dashed line represents particle positions of the neighboring layer in a sliding layer structure. (b) Orientation of close packed hexagonal planes within the gap when the sample has been prepared in an fcc microstate. The double headed arrow represents the allowed range in strain amplitude for neighboring layers, before significant restructuring of the layer occurs.

twin structures. In fact, the scattering observed in these measurements indicates an oscillation between fcc twins. The double headed arrow in Fig. 11b indicates the range in strain amplitude allowed for neighboring layers.

The curve shown on each graph of Fig. 10 represents the maximum allowed strain for an fcc structure comprised of hard spheres, as a function of volume fraction. In this purely geometrical model, the layers become freely slipping for $\phi \leq 0.40$ and caged by their nearest neighbors for $\phi \geq 0.64$, random close packing. At volume fractions between this range, the layers may slide within a range of strain consistent with the observed twinning behavior, schematically represented as the arrow in Fig. 11b. While agreement is not expected, it is observed that the trend in development of an fcc state from an amorphous structure with strain is maintained in the microgels, relative to hard spheres. The open and half filled circles relevant to a 1 Hz oscillation, qualitatively follow the model prediction, shifted to larger strains and volume fraction. At 4 Hz, agreement is less. A possible explanation is the increased importance of the hydrodynamics neglected in this simple model, as the shear rate increases with frequency. The data shown at $\phi^* = 1.03$ is not in contradiction to the above argument, as this sample was intialized in a fcc microstate.

The evolution of these structures exhibits a frequency dependence. The most pronounced difference in structure development with frequency is observed in the $\phi^* = 0.54$ sample. As shown in comparison of Fig. 10a and 10b, 4 Hz shear oscillations induced microstructures much more readily at low strain amplitudes than 1 Hz, melting back to amorphous structure upon cessation of shear flow. Here, the ability to induce microstructure with a 1 Hz. oscillation was realized only after the sample had ordered at 4 Hz, indicating an incomplete return to the amorphous state prior to begining the next run.

It is presumed that the microstructures observed here, as in sterically stabilized suspensions, occur in order to reduce the interparticle stresses while under shear. If there is not enough free space available to accomodate the applied strain, a structural change occurs. The softness of the interparticle potential and particle

deformation is assumed responsible for the increased amplitudes associated with these structures, above that of hard spheres.

Bragg Spots Under Steady Shear

In this section, a set of exploratory measurements were made in order to not only correlate microstructure with observed shear thinning, but also quantify that microstructure by examining the position and intensity of the spots as a function of shear.

Experimental

The scattering geometry used in these measurements is the same as that for the nonequilibrium phase diagram, only now a Bohlin constant stress rheometer equipped with a glass couette was utilized rather than the syringe cell described previously. The couette gap is 0.7 mm and the radius of the inner bob, 7 mm. The sample was presheared at a shear rate of ~ 66 sec^{-1} for 300 sec. followed by ~ 180 sec. of quiescence. This oriented the microstructure such that the closest packed direction in an hcp plane was along the velocity direction. Once presheared, a constant stress was applied and the scattering monitored from one spot on and one off the central axis of the couette. Symmetry considerations only necessetate these spots be monitored in order to determine the particle spacings within an hcp layer. The shear stress was stepped from zero up to values well into the high shear rate plateau and intensities recorded as a function of applied shear stress. Care was taken so that the spot intensity did not saturate the video camera. Samples of effective volume fraction $\phi^* = 1.22$, 1.03, 0.783, and 0.681 were examined.

Results and Discussion

Treating each Bragg spot as a distribution of intensities within a 120x120 grid of pixels, the first moment for the x and y position was calculated resulting in a measure of the spot center. In this way, the position of each spot could be

found as a function of applied shear stress, relative to the zero shear position. From these data, assuming hexagonal close packed symmetry for the lattice plane producing the scattering, the real space lattice point positions were calculated. The position of these points normalized to zero shear are shown in Fig. 12, where ○ and ● indicate center to center particle spacing parallel, v, and perpendicular, e, to the flow direction, respectively. It can be seen that for the two lowest effective volume fraction samples examined, $\phi^* = 0.681$ and 0.783, the hcp layers seem to compress in both the velocity and vorticity directions, with perhaps a slight bit more compression in the velocity direction over that of the vorticity for the $\phi^* = 0.681$ sample. This is roughly consistent with what has been observed in poly(styrene) dispersions [75]. Regretably, absolute measurements could not be obtained due to distortions in the images. At zero shear, variations of up to 10% were observed between the reciprocol space positions of the on and off axis spots, relative to the origin (scattering angle = 0). It is presumed that this observation is due to misalignment of the camera with respect to the screen, and/or a lensing effect due to the optical couette and imperfect index matching. With increasing $\phi^* \geq 1.03$, the results are somewhat unusual. Not only does the compression along the vorticity direction now appear to be slightly greater than that of the the velocity direction, but the spacing along the velocity direction increases somewhat, with the spacing at higher shear stress never decreasing much below its equilibrium value (in fact, increasing for the $\phi^* = 1.218$ sample).

The spot positions as a function of shear rate are shown in Fig. 13. Here it is observed that the minimum in relative particle spacing in the velocity direction is greatest for the lowest effective volume fraction and decreases with increasing ϕ^*. This is intuitively satisfying, as more free space is available for lower volume fraction samples, making the relative change larger. This trend appears opposite for the particle spacing parallel to the vorticity direction. For both v and e directions, this minimum occurs at increasing shear rate with increasing ϕ^*. This may be due to congestion at high effective volume fractions as the hcp layers are jammed against the outer couette wall, requiring larger stresses to increase the density of

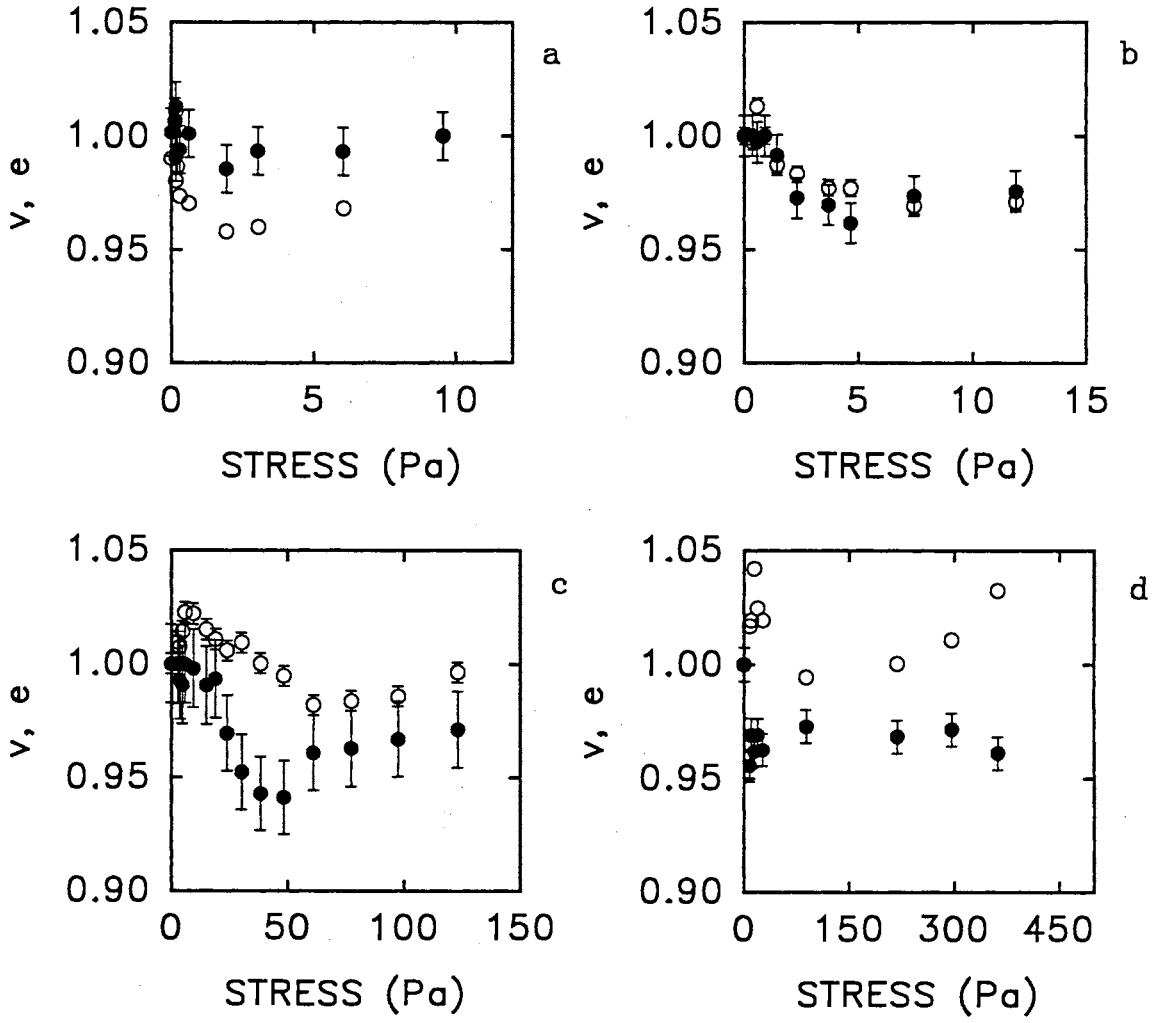

Figure 12. The interparticle spacing in the hcp layers of a sliding layer structure as a function of shear stress, normalized to their zero shear rate values. ○ the direction parallel to the shear flow, ● perpendicular to the shear flow. (a) $\phi^* = 0.681$, (b) $\phi^* = 0.783$, (c) $\phi^* = 1.03$, (d) $\phi^* = 1.218$.

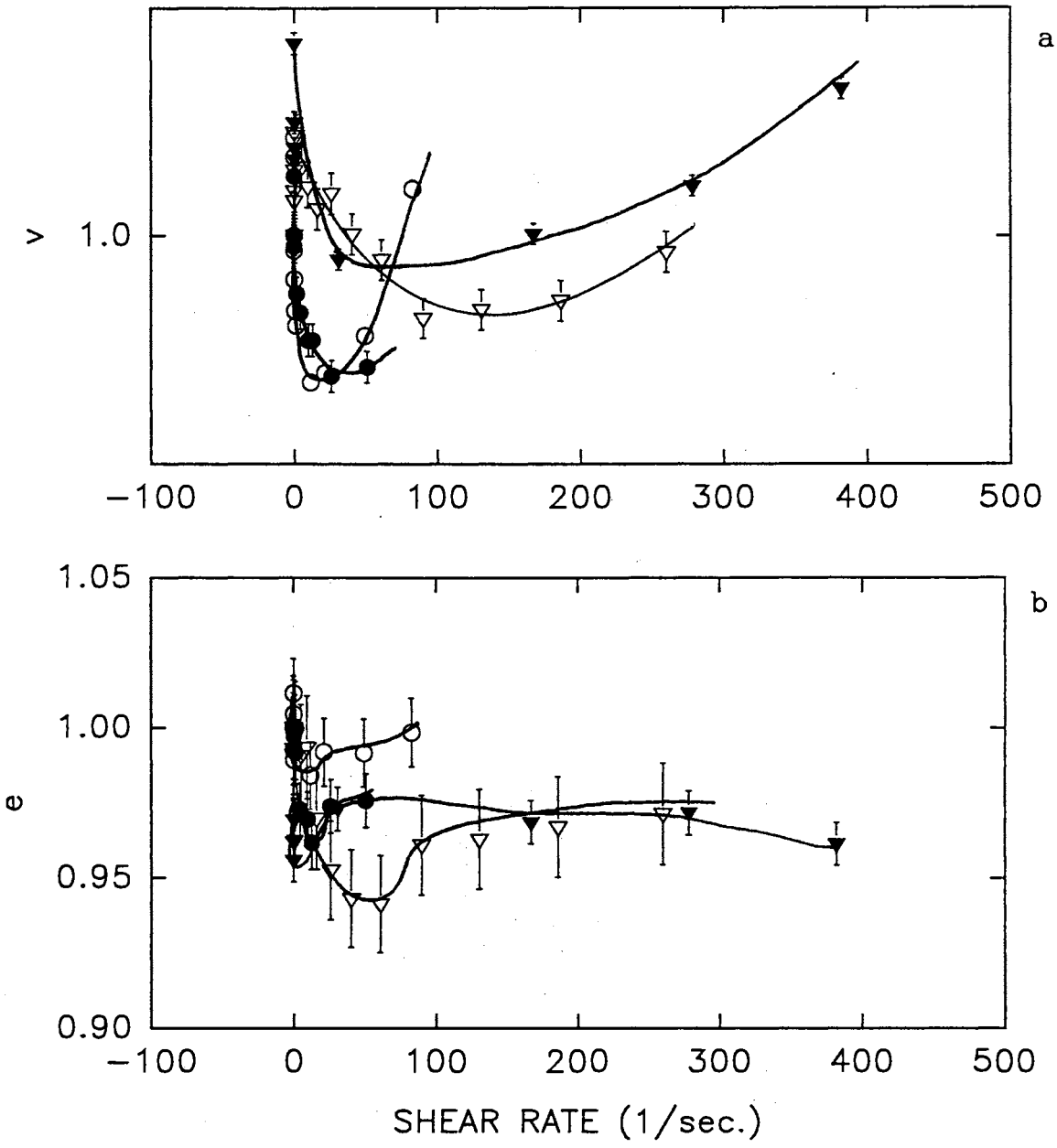

Figure 13. The zero shear normalized interparticle spacings in the hcp layers of a sliding layer structure versus shear rate. (a) the direction parallel to the shear flow, (b) perpendicular to the shear flow. ○ $\phi^* = 0.681$, ● $\phi^* = 0.783$, ▽ $\phi^* = 1.03$, ▼ $\phi^* = 1.218$. Lines are guides to the eye.

particles within an hcp layer. The reason for the apparent reversal of this trend with the $\phi^* = 1.218$ sample is unclear. Since these data are obtained in the shear thinning region and such nonNewtonian behavior is due to the hydrodynamic and microstructural interactions, no simple scaling is observed.

The position data presented here can only be taken as suggestive of possible behavior. Experimental difficulties prevented accurate results in the following ways: The 'run out' for the chuck holding the bob is quoted as $< 10\mu$m/16mm. This manifests itself as a wobble as the bob rotates, which alters the gap by $\sim 45\mu$m at its end. It is unfortunate, but even such a small deviation causes the spot positions to vary with strain and shear rate, as the shear is no longer simple. This effect appeared more pronounced at higher shear rates, presumably due to larger normal stresses as the gap was squeezed and expanded with each rotation. A 40 frame average was used in an attempt to compensate for this irregularity. The error bars associated with the data are an attempt to represent this deviation. Also, as the shear rate increased, the spot shapes tended to become anisotropic, deform and at sufficiently high shear rates, disappear. While this reflects the changing microstructure, it makes determining the spot center, perhaps somewhat ambiguous. Also, it would be best to divide the form factor out of the spot intensities before finding the centers. This was not possible due to the inability to obtain particle form factors at high concentration.

The data for peak spot intensities is equally susceptible to the above experimental difficulties, but nonetheless interesting and at least suggestive in interpretation. Fig. 14 shows the peak intensity data versus shear stress for the spot on ● and off ○ the vorticity axis, respectively. At all effective volume fractions, the intensity is observed to decrease with applied stress. Consistent with observations in sterically staibilized hard sphere PMMA and charge stabilized polystyrene suspensions, the spots on the vorticity axis diminish in intensity much more rapidly than the off axis spots [46]. This is due to the zig-zagging of registered hexagonal close packed layers past one another. Upon increasing the shear stress, the on axis spots continue to diminish, and the off axis spots broaden into elongated nodes

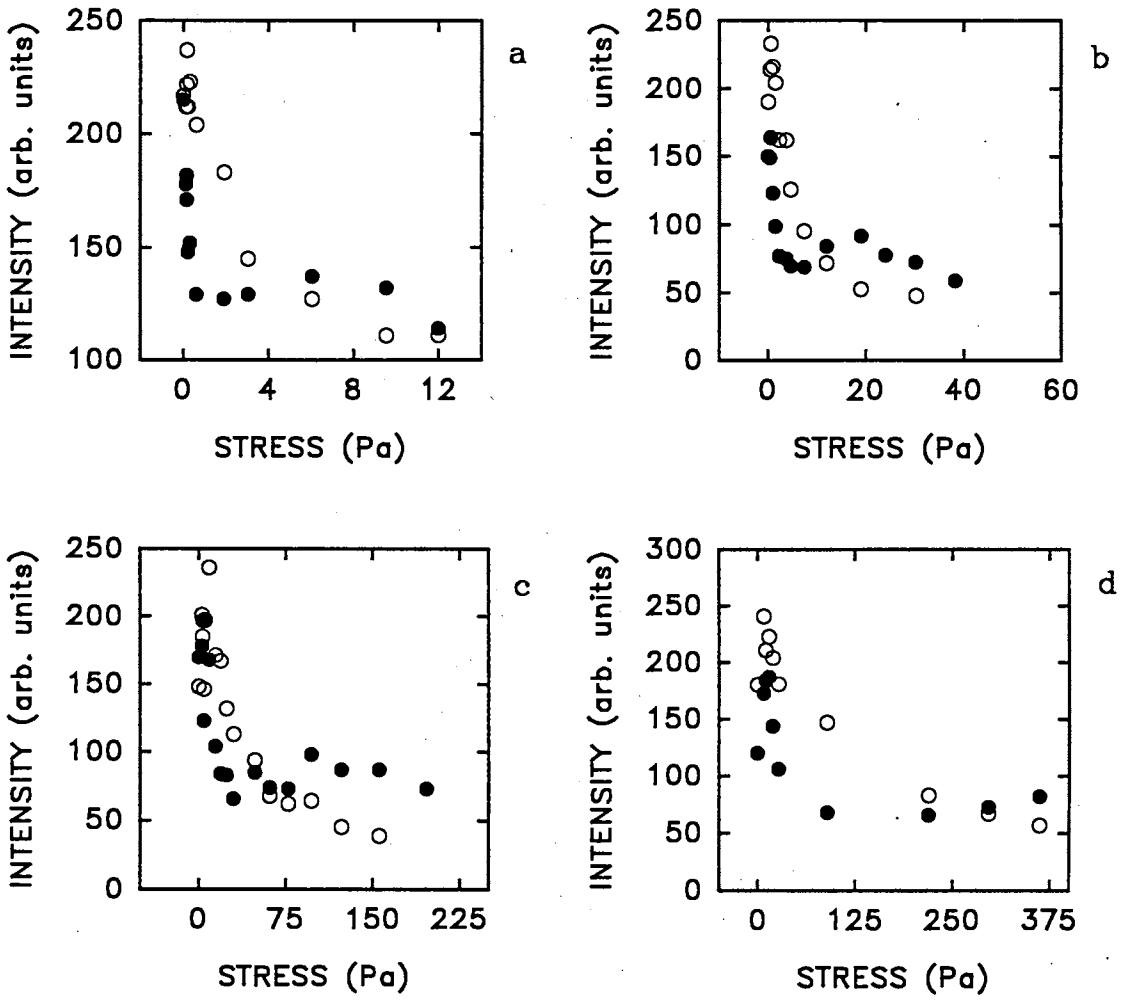

Figure 14. Peak intensities for the ● on axis and ○ off axis Bragg spots versus applied stress. a $\phi^* = 0.681$, b $\phi^* = 0.783$, c $\phi^* = 1.03$, d $\phi^* = 1.218$.

along the vorticity direction. This indicates that the hcp planes are disrupted, and now oriented as strings of regularly spaced particles along the velocity direction. However, increasing the stress further causes the on axis spots to brighten, while the off axis continue to diminish and elongate parallel to the vorticity direction. This may indicate that the microstructure has evolved into a structure in which the regularly spaced particles in the strings along the velocity direction have become sufficiently jammed together as to form a nearly solid line. Since it is observed that the on axis spots appear to move to smaller angles at approximately the same stress they brighten, it is possible that the form factor is responsible for the increased intensity. However, more controlled measurements are necessary to sort out these difficulties.

The microstructural transitions from random stacked to sliding layer and sliding layer to string like structure are hydrodynamically driven. However, the scattering only depends on the final geometrical result of those hydrodynamic interactions. The scattering images observed for each effective volume fraction are overall very similar. The necessary shear stress to drive different effective volume fraction samples into similar scattering patterns increases with particle concentration. Assuming Brownian motion to be negligible at these applied stresses, one might expect the shear rate to be the important parameter in determining the observed intensity of the Bragg spots. Fig. 15 shows the observed scattering intensity for the (a) off axis and (b) on axis spots as a function of shear rate. Each sample was shifted by an arbitrary factor in intensity to bring all of the curves into coincidence. The significance of this scaling is presently not clear.

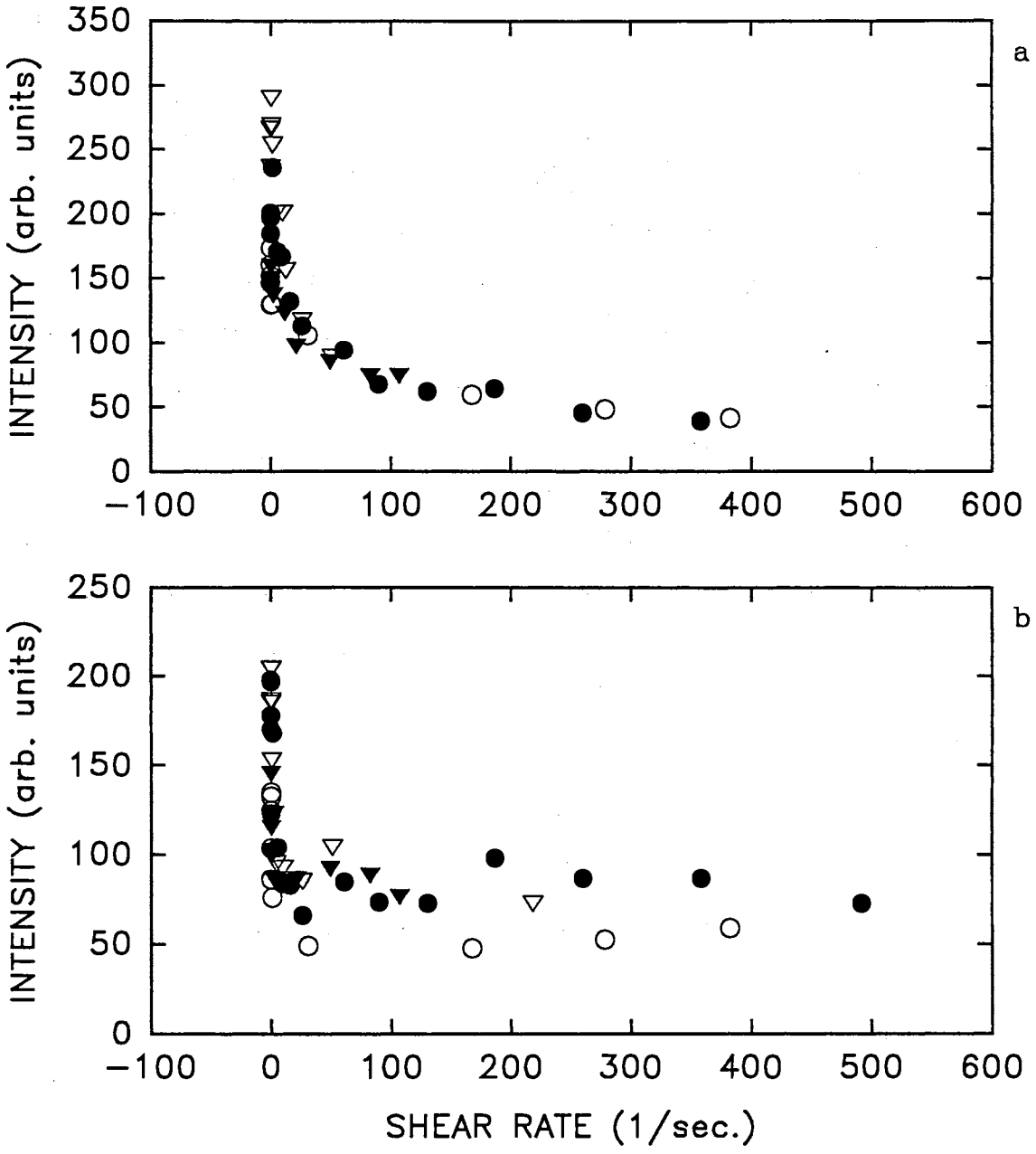

Figure 15. Peak intensities for (a) the off axis spot (b) the on axis spot versus shear rate. Here, ○ $\phi^* = 1.218$, ● $\phi^* = 1.03$, ▽ $\phi^* = 0.783$, ▼ $\phi^* = 0.681$. The intensities were scaled by an arbitrary factor.

CHAPTER V

STEADY STATE OPTO-RHEOLOGY

Introduction

The importance of correlating macroscopic rheological properties with underlying dispersion microstructure has already been outlined in Chapter IV. However, no connection was made there between the observed shear induced structures and their rheological properties. In this chapter, a connection of these structures with rheology will be explicitly examined in the concentrated limit. Unique with respect to the present rheo-optical measurements being made, specific shear induced microstructural states are introduced and compared rheologically by observing the strain response under a specific applied stress (creep and creep recovery measurements). A requirement for making such measurements is that the induced structure be stable once there. For the microgels examined, this sets a lower bound on the effective volume fractions suitable for study at ~ 0.55 [1]. Below this value, Brownian motion tends to melt the induced microstructure back to amorphous order upon cessation of shear flow. The actual measurements were made at $\phi^* > 0.65$ in order to increase the effects of microstructure by increasing interparticle interactions. The samples examined are therefore in what may be termed a glassy state.

Dispersion rheology is governed by viscous and thermodynamic contributions to the bulk stress. The viscous (hydrodynamic) interactions arise from interactions between the particles and surrounding fluid. These include forces due not only to an applied shear flow, but also a Brownian contribution from incessant colloidal particle motions. The thermodynamic contributions result from interparticle forces, to which Brownian motion also contributes in the form of a thermodynamic

driving force. An indirect contribution to bulk stress arises from the particle configuration - the equilibrium microstructure. When thermodynamic interactions between particles becomes significant enough to produce structure in the equilibrium radial distribution function, the contribution to bulk stress is increased above that of that due to purley viscous contributions. The effect of these interactions on the rheology of dispersions is typically observed as shear thinning [59]. Here, the viscosity as a function of applied shear stress exhibits a Newtonian plateau at low stress, which decreases as the stress is increased, until a high shear stress plateau is reached. The Newtonian plateau at low stress is governed by Brownian motion and the equilibrium structure of the suspension. If Brownian motion is strong enough relative to other interparticle interactions that an equilibrium state may be maintained under shear flow, the plateau is observed. At high stresses, viscous forces overcome the thermodynamic contributions and a high shear stress plateau is observed. As mentioned in Chapter IV, the Péclet number gauges diffusive to convective time scales. Thus, for $Pe > 1$ nonNewtonian (shear thinning) behavior should be observed.

In the case that the interparticle interactions become strong enough that Brownian motion is negligible, the low shear rate plateau may vanish and the viscosity appear to diverge as the stress is reduced. For hard sphere like dispersions, this is typically observed when the suspension volume fraction is increased to near random close packing $\phi \sim 0.64$, decreasing the relative particle spacing and thus reducing the self diffusion [82]. In charge stabilized systems, the same effect has been observed by reducing the ionic strength at a constant volume fraction [83]. An equivalent but perhaps more general dimensionless number which can be used to classify suspension behavior is the Deborah number [84],

$$De = \frac{\text{time of relaxation}}{\text{time of observation}} \tag{19}$$

If the 'time of relaxation' is identified as that given by diffusion and the 'time of observation' identified as the shear rate, the Péclet number is recovered. However, the utility of thinking in terms of the Deborah number becomes apparant

when examining creep measurements in 'glassy' nonequilibrium colloidal suspensions. Here, it becomes not a question of whether the suspension flows, but on what time scale it flows.

At the effective volume fractions examined for the PMMA microgels, the shear viscosity versus applied stress appears to diverge at low stress, as shown in Fig. 16. Unable to achieve the low shear rate limit, the common ground of linear viscoelasticity is not present and the comparison of rheological results with that of, say, hard spheres not possible. However, this does not eliminate the ability to examine microstructural evolution in the microgels within the context of their own rheological behavior. Comparison of microstructural states is examined through nonlinear creep and creep recovery measurements. From these results, the viscous response due to the applied stress is observed and an instantaneous viscosity calculated and correlated with microstructural evolution. These results also suggest the observed elastic recovery is due to local suspension microstructure and/or particle deformation.

Creep and Creep Recovery

The viscoelastic behavior of suspensions require the formulation of a constitutive equation which encompases the ability to both store and dissipate mechanical energy. With no regard for microstructure, such a relationship can be contructed by considering viscoelastic materials as those which posess a memory [85]. If the stress applied to a material is changed, the material responds to this change, along with a continued response to the initial stress. That is, the present state of deformation is due to the entire past history of applied stress. It is expected that this memory effect fades with time, so that the present state of stress is most strongly determined by its most recent state of deformation. For homogeneous materials in which the displacements are kept infinitesimal, a formal expression of such a relationship in simple shear may be written as [85],

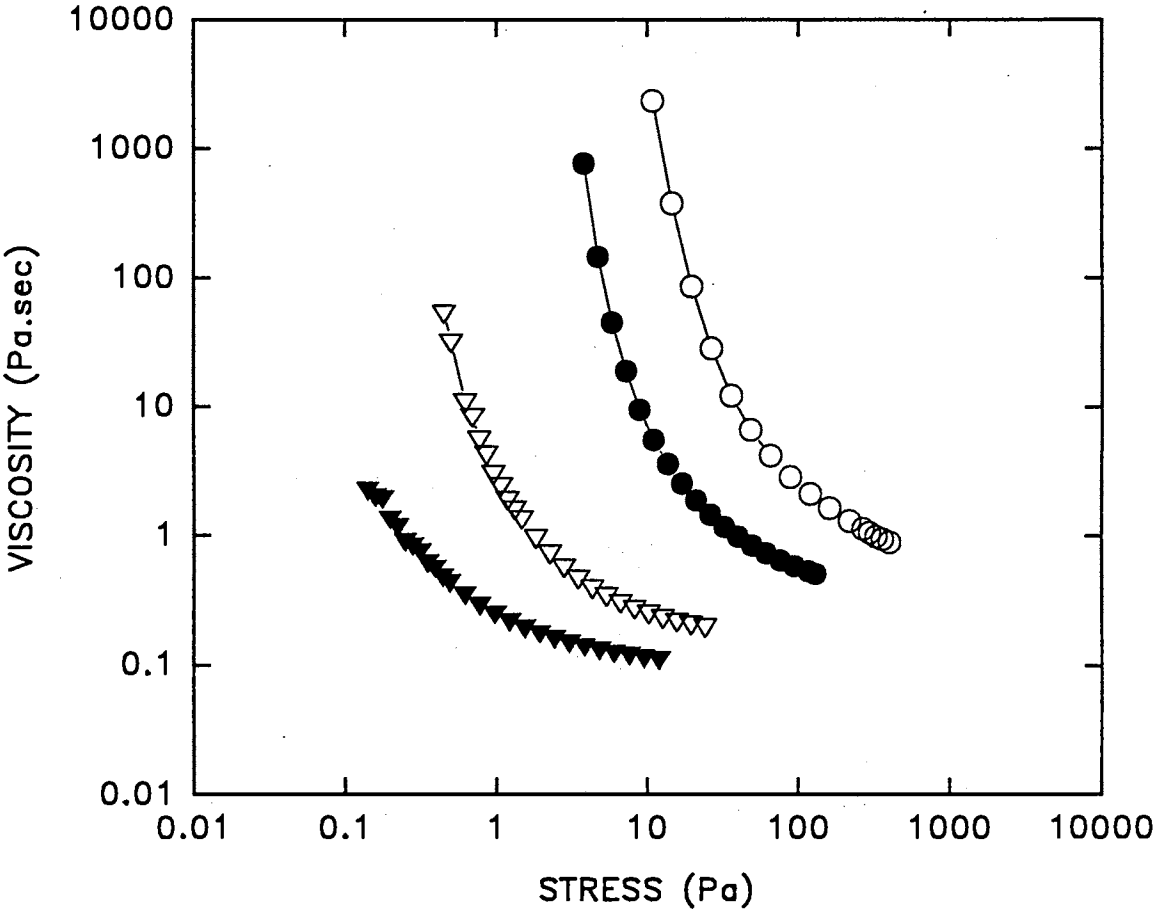

Figure 16. Shear viscosity versus shear stress for ○ $\phi^* = 1.218$, ● $\phi^* = 1.03$, ▽ $\phi^* = 0.783$, ▼ $\phi^* = 0.681$.

$$\sigma(t) = \int_0^t G(t-\tau)\frac{d\gamma(\tau)}{d\tau}d\tau \tag{20}$$

which represents the stress at time t resulting from a change in strain, $\gamma(\tau)$, at time τ, weighted by the past history of all applied strains for $t < \tau$. $G(t)$ represents mechanical properties of the material, termed a relaxation function, as it represents the stress behavior after deformation. It is assumed positive and decreasing with time, consistent with the concept of fading memory. The amplitude of $G(t)$ is the elastic shear modulus for the material. Note that for a viscoelastic solid, intuition tells us that $G(\infty) =$ constant, where as for a viscoelastic fluid, $G(\infty) = 0$. That is, for a viscoelastic solid the induced stress state remains nonzero for all times. For a viscoelastic fluid, the stress state induced will eventually decay to zero.

To gain a better physical understanding of relaxation functions, it is useful to decompose $G(t)$ as

$$\begin{aligned} G(t) &= G^o + \hat{G}(t) \\ \hat{G}(t) &\rightarrow 0 \text{ as } t \rightarrow \infty \end{aligned} \tag{21}$$

where G^o represents the long time modulus. $G^o = 0$ for a viscoelastic fluid, and so a viscoelastic fluid behaves as such for long time scales ($G(\infty) \rightarrow 0$). A viscoelastic solid will likewise behave as a viscoelastic solid for long time scales ($G(\infty) \rightarrow G^o$). However, on short time scales, a viscoelastic material will behave like a viscoelastic solid regardless of whether or not its long time behavior determines it to be a fluid. Note, if both G^o and $G(0)$ are defined to be zero, then one is no longer describing a viscoelastic, but a purely viscous material. An important distinction to be made here is that the time scale your measurement probes ultimately determines whether you are measuring $G(0)$, $G(\infty)$ (or both), and they are not the same. Moduli are meaningless unless the corresponding time scale under which it was measured is given. The short time moduli is also known as the equilibrium modulus, G_o, which presumably yields the unperturbed elasticity of the equilibrium structure. The long time modulus, G^o, yields a 'system' elasticity for a state which is deformed

but in steady state. Consistant with $G^o = 0$, a viscoelastic fluid can sustain shear flow, with a steady state viscosity, η_o.

These limits will have important consequences later on in this chapter where creep and creep recovery (defined below) results are compared with that obtained from dynamic data (see Chapter VI for dynamic measurements).

Similar to the expression for stress relaxation, the strain response as a function of imposed stress may be written [85]

$$\gamma(t) = \int_0^t J(t-\tau)\frac{d\sigma(\tau)}{d\tau}d\tau \tag{22}$$

where $J(t)$ is termed the creep function, which like $G(t)$, represent macroscopic mechanical properties of the material. The results presented in this chapter were obtained under the conditions of an applied constant stress. Since physical intuition as to the nature of $J(t)$ may be less abundant than for stress relaxation functions, it is important to make a connection between the two. The form of Eqns. 20 and 22 are amenable to the convolution theorem, which states

$$\mathcal{L}^{-1}\left\{\widetilde{f(s)}\widetilde{m(s)}\right\} = \int_0^t f(t-\tau)m(\tau)d\tau \tag{23}$$

where the tilde represents the Laplace transform of a given function, with s the transform variable. $\mathcal{L}^{-1}$ is the inverse Laplace transform. Given the above, the Laplace transform of Eqns. 20 and 22 results in

$$\begin{aligned} \widetilde{\sigma(s)} &= \widetilde{G(s)}(s\widetilde{\gamma(s)} - \gamma(0)) \\ \widetilde{\gamma(s)} &= \widetilde{J(s)}(s\widetilde{\sigma(s)} - \sigma(0)). \end{aligned} \tag{24}$$

Although they are related over all time scales, the relationship is most useful in the limit of small and large times. The initial and final value theorem for Laplace transforms allows one to write,

$$\lim_{t\to 0} G(t) = \lim_{s\to\infty} s\widetilde{G(s)} \tag{25}$$

$$\begin{aligned}
\lim_{t\to 0} J(t) &= \lim_{s\to\infty} s\widetilde{J(s)} \\
\lim_{t\to\infty} G(t) &= \lim_{s\to\infty} s\widetilde{G(s)} \\
\lim_{t\to\infty} J(t) &= \lim_{s\to\infty} s\widetilde{J(s)}
\end{aligned}$$

from which it can be seen,

$$\begin{aligned}
\lim_{t\to 0} J(t) &= \lim_{t\to 0} \frac{1}{G(t)} \\
\lim_{t\to\infty} J(t) &= \lim_{t\to\infty} \frac{1}{G(t)}.
\end{aligned} \tag{26}$$

This provides a more physical meaning to the creep functions, and is important when attempting to obtain elastic moduli from creep data.

The creep function can be obtained from a simple rheological measurement. Allowing $\sigma(t) = \sigma_o h(t)$, where $h(t)$ is a unit step function, Eqn. 22 yields

$$J(t) = \begin{cases} 0 & t < 0 \\ \frac{\gamma(t)}{\sigma_o} & t \geq 0. \end{cases}$$

It is therefore possible to experimentally measure the creep function by applying an instantaneous step in stress to some finite value, σ_o, and observe the resulting strain response, $\gamma(t)$, as a function of time.

The behavior of the creep functions depend, of course, upon whether the system is a viscoelastic fluid or solid. For a fluid, $J(t)$ will be a continuously increasing function of time, achieving steady state when $J(t)$ is linear in time, with $dJ(t)/dt = 1/\eta_o$ in this limit. The material exhibits a shear viscosity, which for a shear thinning fluid represents the low shear rate Newtonian value. For a solid, $J(t)$ will eventually plateau at some constant value, and of course has no defined shear viscosity. Such statements are all consistent with Eqn. 26. The short time response of the creep function depends upon the physical process of energy storage and dissipation in the material. That is, $J(0)$ may or may not have a measurable nonzero value. $J(0)$ is also known as the glassy compliance, J_g. From the above considerations, it is clear that $J_g = 1/G_o$.

Correspondingly, upon removal of the applied stress the recoverable strain, $\gamma_r(t_c, t)$, can be observed in time, yielding a measurement of the recovery function, $J_r(t_c, t) = \gamma_r(t_c, t)/\sigma$. Here, t_c is the length of time the stress is applied and t the recovery time. (at time t_c, $t = 0$). It is assumed here that t_c is long enough such that the material is in steady state at the begining of recovery. That is, for all practical purposes, the material views t_c as ∞. In essence $J_r(t_c, t)$ is a measure of the recoil of the material, or the recovery of stored energy. Here, $J_r(t_c, 0) = 1/G(0) = 1/G_0 = J_g$ for both a fluid and a solid. However, $J_r(t_c, \infty) = 1/G(\infty) = 1/G^o$ for a viscoelastic solid, but not for a viscoelastic fluid. For a viscoelastic fluid, $J_r(t_c, \infty) = J^o$, where J^o is the long time compliance, much like G^o is the long time modulus for a solid. Note that $J^o \neq 1/G^o$. They are two fundamentally different quantities based on the different nature of viscoelastic solids and fluids.

The above results are for linear viscoelastic measurements. Although this makes the creep and relaxation functions quantities which are strictly defined only within those constraints, this does not preclude one from making the same measurements in the stress sensitive nonlinear region. Here, instead of obtaining one master curve for $J(t)$, relevant for all stresses below some critical stress (above which the flow becomes nonNewtonian), one will measure a family of functions, $J_\sigma(t)$, which depend on the stress applied, σ_o. The question now becomes whether or not any useful information can be teased from such measurements. Are the moduli obtained at all relevant? Certainly, beyond the linear regime the elastic moduli are no longer constant. Also, the glassy compliance measured would no longer represent a measure of the equilibrium modulus since by definition, J_g is a linear quantity. Such consequences present a dilema in trying to correlate suspension microstructure with the rheology. Therefore, in terms of linear viscoelasticity, the results presented in this chapter must be interpreted with caution. However, this makes the analysis all the more interesting, as an "in spite of... it is observed..." tenor can sometimes yield fruitful results.

One final note about semantics. In an attempt not to confuse linear and nonlinear creep functions, it should be assumed that all creep functions mentioned from this point on are nonlinear, which may functionaly exhibit linear and/or nonlinear regions.

Instantaneous Viscosity Measurements

The nonequilibrium phase behavior of these suspensions has been described in Chapters III and IV. As noted there, microstructures consisting of ordered layers of hexagonal close packed (hcp) planes, randomly stacked parallel to the shear direction in a simple shear measurement, can be induced. Further, the closest packed direction can be oriented either parallel to the velocity or vorticity direction, depending upon the initial preparation. All samples examined in this study are sufficiently concentrated that long lived microstructural states could be induced. That is, once a specific microstructural state was induced, it remained in that state for an indefinite period of time. Relaxation of the structure was exhibited on the time scale of hours, typically by a narrowing of the diffraction spots. This narrowing may be an indication that the induced crystal structure is annealing out defects. Though interesting, this effect was not studied. All measurements reported were on induced structures which were only minutes old.

A Bohlin Instruments constant stress rheometer, equipped with a glass C14 concentric cylinder shear cell, was used to measure the creep and recovery response to an applied stress, while simultaneously monitoring suspension microstructure. The radius of the rotating inner bob is 7 mm, with a gap size of 0.7 mm between the bob and fixed outer cup. The temperature of the shear cell was not controlled, and left to the ambient value ($\sim 20°C$). To prevent solvent evaporation, a solvent trap consisting of a a knife edge and trough filled with benzyl alcohol was utilized. The low volatility of benzyl alcohol coupled with the solvent trap allowed measurements to be made over a period of days with no appreciable evaporation. Viscosity as a function of applied shear stress was periodically measured to monitor any volume fraction changes due to solvent evaporation.

The scattering geometry is identical to that shown in Fig. 8 used in the nonequilibrium studies in Chapter IV. Here, a helium cadmium laser (λ = 442 nm) probes the suspension microstructure approximately in the $\vec{v}\vec{\Omega}$ plane. Further, to reduce the effects of refraction, the couette was immersed in a rectangular index matching bath of glycerin, and the scattering imaged directly on the front of the index bath container. The observed scattering patterns were video taped for digitizing.

Nonlinear creep, $J_\sigma(t)$, and creep recovery, $J_{r,\sigma}(t_c, t)$, measurements were made on samples of effective volume fraction ϕ^* = 1.22, 1.03, 0.783, and 0.681, over a series of discrete times ranging from t = 2 to 22000 sec. Measurements were repeated over a range of applied stresses for each effective volume fraction. The initial microstructural state of each run consisted of two different orientations of random stacked hexagonal close packed planes, indicated by the scattering patterns shown in Fig. 17a and 17b, respectively.

The same initial preparation was followed for each measurement, which consisted of preshearing the suspension at a shear rate of$\sim$ 66 sec^{-1} for 300 sec followed by $\sim$ 180 sec of quiescence. This was the preparation for what is termed the presheared microstructure. This oriented the closest packed direction of the hcp planes along the velocity direction. For the microstructure termed here as fcc, the preparation was the same as the that of the presheared, except the bob was moved up and down (vertically) a set number of repetitions, prior to beginning the measurement. This oriented the closest packed direction of the hcp layers in the vorticity direction. Strictly speaking, such a microstructural state is not in an fcc stacking sequence. However, as this structure evolves into an fcc twin when strained, it is termed an fcc structure for the purposes of this and future chapters. The preshearing shear rate, time of preshearing, quiescence, number, and amplitude ($\sim$ strain of one) of vertical repetitions were all determined by experience with the microgels as reasonable parameters which brought the sample back to some uniform initial state. Reproducibility of the observed scattering is reasonable.

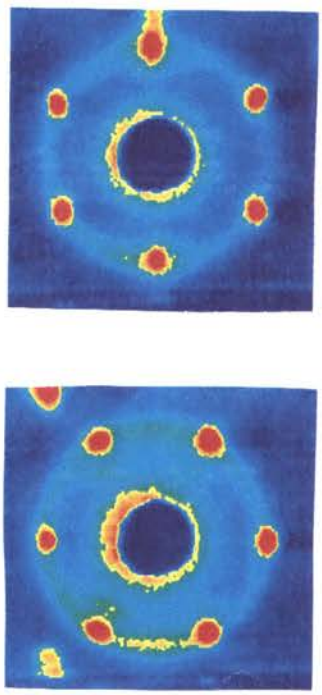

Figure 17. Scattering images from structures identified as random stacked hexagonal close packed planes with the closest packed direction oriented parallel to (a) the velocity direction, (b) the vorticity direction (as depicted in Fig. 8).

Results and Discussion

The results of the above measurements supply one with a set of nonlinear creep and creep recovery curves which vary in magnitude of applied stress, time for which the stress is applied, intitial microstructure, and effective volume fraction. A typical example of such creep functions are shown for $\phi^* = 1.03$ at $\sigma_o = 5$ Pa and 8 Pa, in Fig. 18a and 18b, respectively. Here, the distinct form for each creep function is peculiar to the initial microstructural state, as well as applied stress. The open circles in each graph, ○, correspond to the microstructure shown in Fig. 17a, and the solid circles, ●, 17b. These scattering patterns are indicative of hexagonal close packed planes aligned parallel to the shear cell wall, but randomly stacked in the shear direction. However, due to the different orientation of the closest packed direction in these layers, relative to the velocity direction, each structure exhibits vastly different strain behavior for a given applied stress. The structure exhibited in 17a may accomodate an unlimited amount of strain, provided the shear rate is low enough that the close packed planes themselves do not become disrupted. Here, the closest packed direction lies along the velocity direction, allowing the layers to slide past one another while still maintaining registration between each layer. It would thus be expected that no large structural evolution would occur during a creep measurement. The scattering shown in Fig. 17b is produced by an alignment of the closest packed direction parallel to the vorticity. A limited amount of strain will remove the randomness of the stacking, causing the layers to stack in an order indicative of a face centered cubic (fcc) crystal with the [111] direction oriented perpendicular to the cell wall. As described in Chapter IV, the fcc structure can only accomodate a limited amount of strain before evolution into the sliding layer structure begins. If unlimited strain is imposed, the hcp planes themselves will become disrupted, eventually evolving back to the random stacked hcp alignment of 17a. The creep behavior observed in Fig. 18 supports the 'geometrical' considerations above, as the fcc structure strains less for the same applied stress and given time, than the structure which allows unlimited and

relatively easy slippage of hcp layers. It is simply easier to slide layers past one another, as in a presheared structure, than to restructure the hcp planes as in a strained fcc structure. The initial oscillation at short times appears in nearly all measurements and is an instrumental artifact due to the inertial response of the measuring system. Depending on how the rheometer controls the stress, this 'ringing' may or may not contain useful rheological information. However, this possibility was not pursued.

The measured nonlinear creep functions only become of interest when examined in light of the their respective recovery measurements. Certainly, the family of creep functions represent valid measurements. Yet, taken as a single result their interpretation is not clear, as they presumably represent a mixture of elastic and viscous responses to applied stress and microstructure. As will be shown below, the elastic relaxation appears to be relatively short, rendering the nonlinear behavior of the creep curves due to a viscous restructuring of suspension microstructure. This allows an instantaneous viscosity, as a function of strain and microstructure, to be calculated.

The total recoverable strain obtained over a series of different applied times, for several applied stresses, and for each effective volume fraction sample examined is shown in Fig. 19. Here it is observed that the total recoverable strain, $\gamma_{r,\sigma}(t_c, \infty)$, is nearly constant over all time scales measured and that it appears independent of the microstructure. This result indicates that the suspension is elastically relaxed within $\sim$ 2 sec., the shortest time scale probed. This is initially surprising since the creep curves clearly indicate nonlinear behavior at the time at which the stress was removed, t_c, and recovery measured. For example, comparing Fig. 18a over the measured time with the results of Fig. 19b, $\sigma_o = 5$ Pa, clearly shows that the same amount of recoverable strain was measured throughout the nonlinear region, independent of microstructure.* Since the standard thinking in terms of

*The data plotted in Fig. 19b was not obtained from the single creep curve of Fig. 18a, but a multitude of measurements, each starting with the same initial state as that of Fig. 18a, but with varying times of applied stress, t_c, before which a recovery measurement was begun.

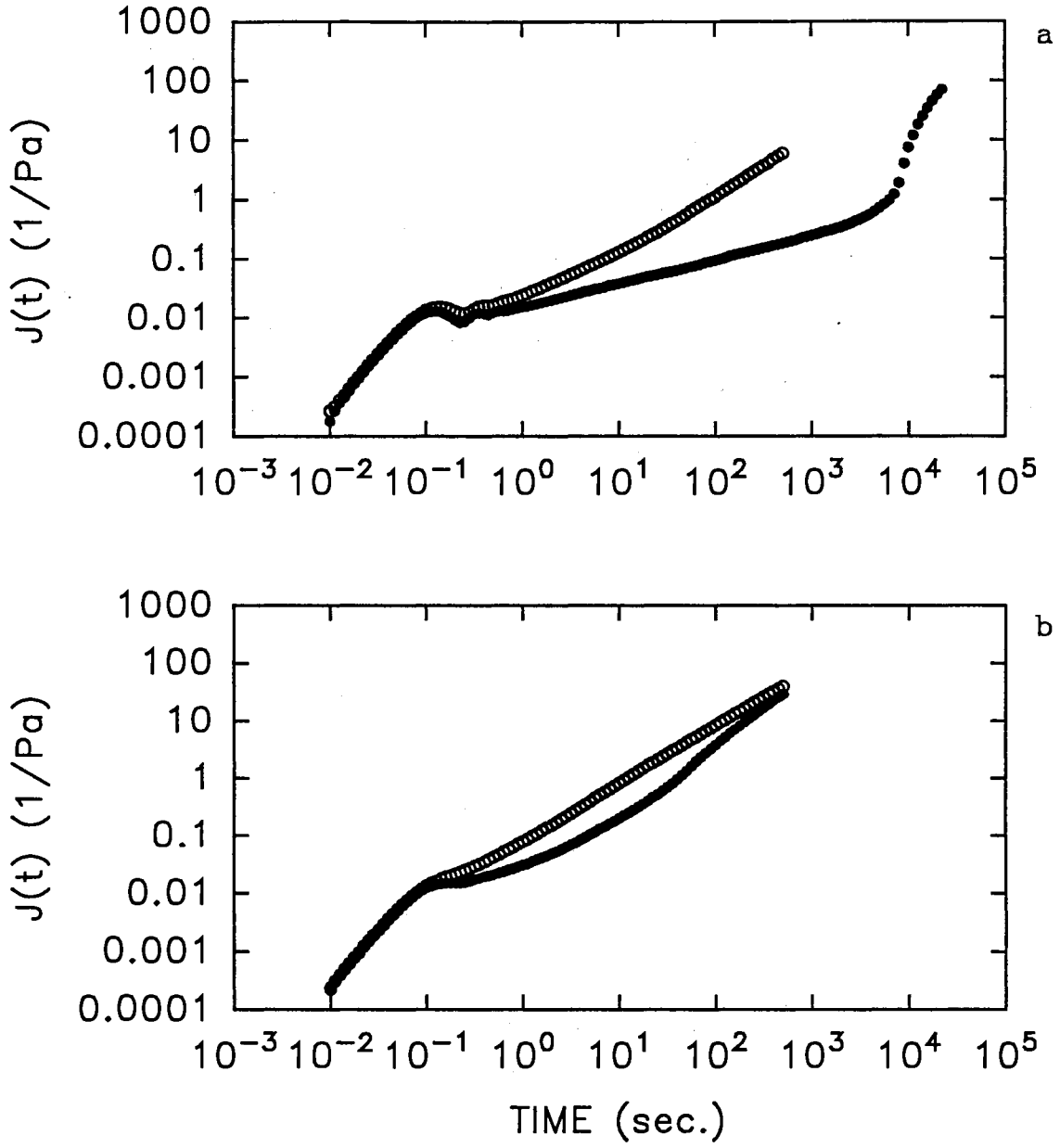

Figure 18. Typical nonlinear strain response versus time for $\phi^* = 1.03$, (a) $\sigma_o =$ 5 Pa ○ presheared structure, ● fcc structure, (b) $\sigma_o = 8$ Pa ○ presheared structure, ● fcc structure.

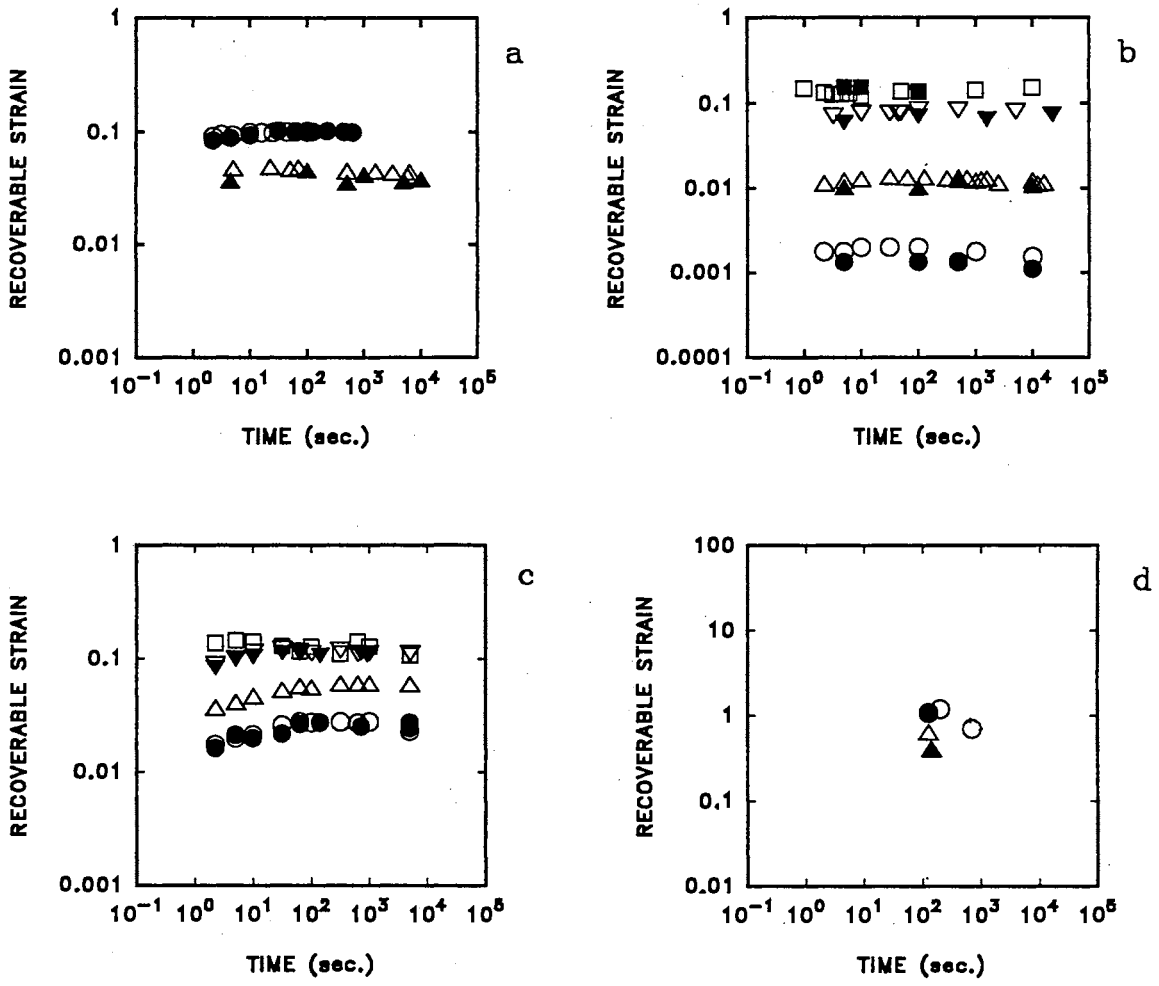

Figure 19. Total recoverable strain as a function of time, for effective volume fractions and applied stresses noted below. (a) $\phi^* = 1.22$, ◯20 Pa, △10 Pa, (b) $\phi^* = 1.03$, ◯0.14 Pa, △1.0 Pa, ▽5.0 Pa, □10.0 Pa, (c) $\phi^* = 0.783$, ◯0.14 Pa, △0.25 Pa, ▽0.5 Pa, □1.0 Pa, (d) $\phi^* = 0.681$, ◯0.14 Pa, △0.25 Pa. Open symbols represent the initial structure as presheared and closed symbols that of fcc.

creep measurements is that the nonlinearity observed is in general, due to elastic relaxation of the material, and yet the microgels exhibit such nonlinear behavior in spite of appearing elastically relaxed, the observed nonlinearity in the creep curves must be due to a viscous restructuring of the suspension. An immediate consequence of this is that an instantaneous viscosity, η_i, may be calculated directly from the long time creep functions

$$\frac{1}{\eta_i(\gamma)} \equiv \frac{dJ_\sigma(t)}{dt}. \tag{27}$$

This result is shown in Figs. 20, 21, 22, and 23, and dramatically illustrates the effect of microstructure on the suspensions viscous response under applied constant stress. The peaked curve in each graph, indicated by ●, is the measured instantaneous viscosity versus strain for an initial microstructure with the closest packed direction oriented parallel to the vorticity direction (what is called an fcc, here). The corresponding scattering patterns labeled A through F are associated with the evolution of this structure at the indicated strains. It is observed that this structure evolves from that of random stacked hcp planes, to that of an fcc twin as indicated by the three fold symmetric pattern. The relatively constant instantaneous viscosity indicated by ○, is for an initial microstructure where the closest packed planes are oriented parallel to the velocity direction (what is called presheared, here). The scattering pattern for such a structure is identical to that of image F, and shows relatively little evolution under the stresses applied, compared to that of the fcc. Thus, the suspension microstructure is in two different initial states which evolve differently under applied stress, and ultimately end up in the same final microstructural state. This is reflected in η_i where differences in microstructure, aside from orientation, do not appear significant at small strains, but increase dramatically as the strains become large enough to significantly disrupt the structure, and again approach the same value as the microstructures approach similar orientation. These results are qualitatively consistant with a geometrical interpretation, as the peak instantaneous viscosity observed for the fcc twin structure occurs at an increased strain with decreased effective volume fraction, where

there would be more free space available for interacting hcp layers. However, these measurements are in the shear thinning region where hydrodynamic interactions play a dominant role in the rheology. Measurements of η_i at applied stresses larger than those of Figs. 20 - 23 typically show a broadening of the peak, with the initial rise in instantaneous viscosity occuring at smaller strains and peaking to a lower value. This is shown in Fig. 24 where η_i for the fcc structure is plotted for $\phi^* = 0.783$ at applied shear stresses of 0.3 Pa to 0.5 Pa. The microstructure typically shows a twinning at strains less than 0.1, which is maintained through the peak. As η_i starts to decrease, the fcc twin begins to exhibit some distortion, which typically worsens as the strain increases and η_i levels off. Therefore, the observed form of η_i and strains at which it peaks need to be treated with caution. For a given effective volume fraction, they depend on the applied stress. It is also observed that while the general form of the curve may be the same, errors in the peak viscosity of up to 30% can occur. The scattering appears the same initially for these runs, indicating either the lack of sensitivity in the scattering to predict detailed creep behavior, or the need for more careful intensity measurements. It is probably a combination of the two. The minimal increase observed in the recoverable strain for the $\phi^* = 0.783$ shown in Fig. 19 may be due to the increased microgel spacing, allowing for more particle compression and increased elastic behavior. The viscous response may therefore contain some small component of elastic relaxation. Data for the $\phi^* = 0.681$ sample is incomplete and scattered, as inertia of the bob caused difficulties in determining when the creep stopped and recovery begun.

There does not appear to be a significant difference between the recoverable strain and observed microstructure. This is an indication that the elastic recovery is due to local microstructure and/or particle deformation. However, more surprising is the results shown in Fig. 25. Here it is observed that the recoverable strain scales on the applied stress. The suspension is therefore behaving with a linear elastic response, even though the applied stress is clearly in the nonlinear region. A possible mechanism for this is a strain triggered viscous response, where by the

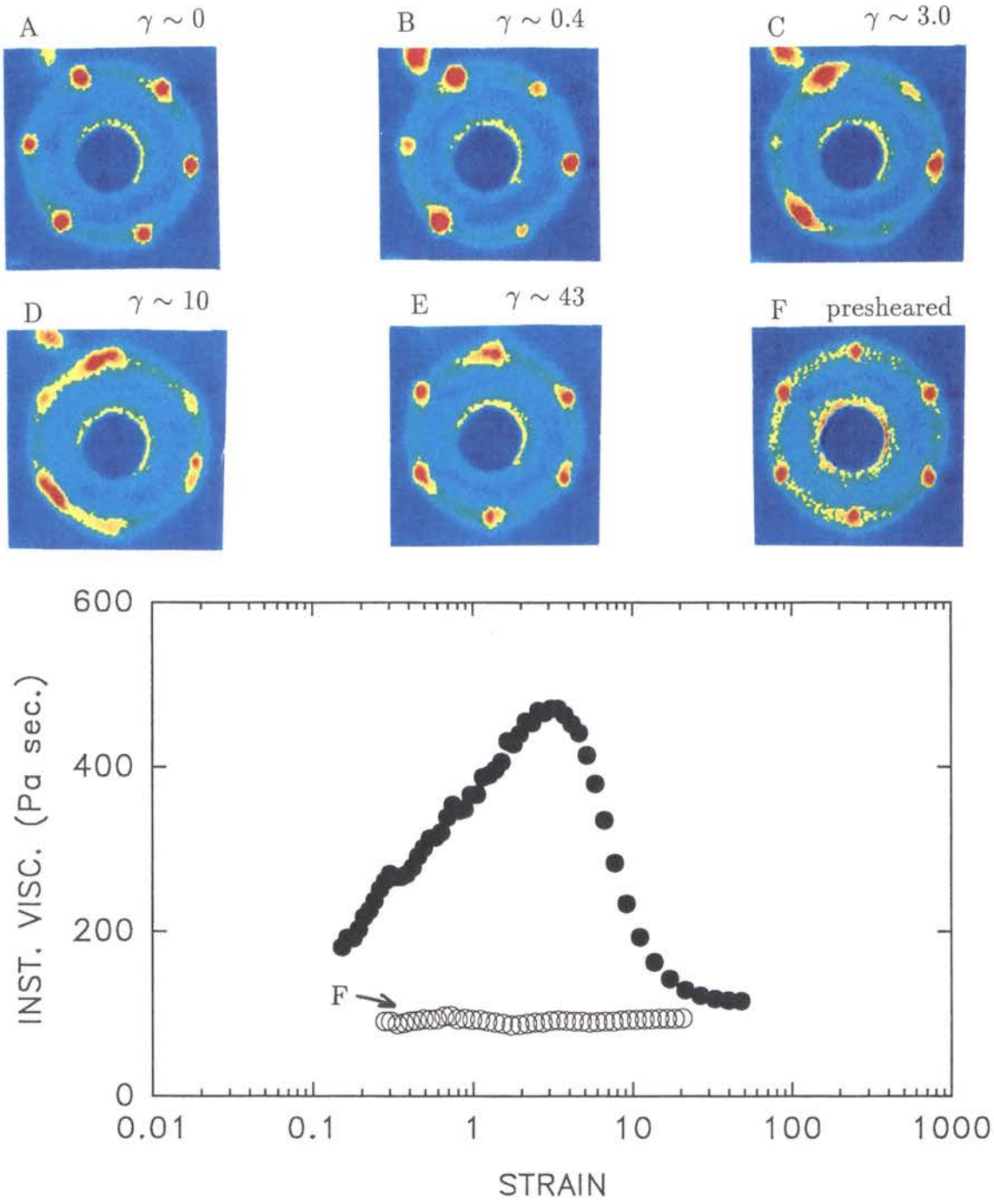

Figure 20. The instantaneous viscosity as a function of strain for microgel suspensions ($\phi^* = 1.22$, $\sigma_o = 20$ Pa) prepared in presheared and fcc microstructural states. Observed microstucture is shown by above scattering images, which correlate with the viscous response, as noted by A, B, C, D, and E. $\gamma \equiv$ strain.

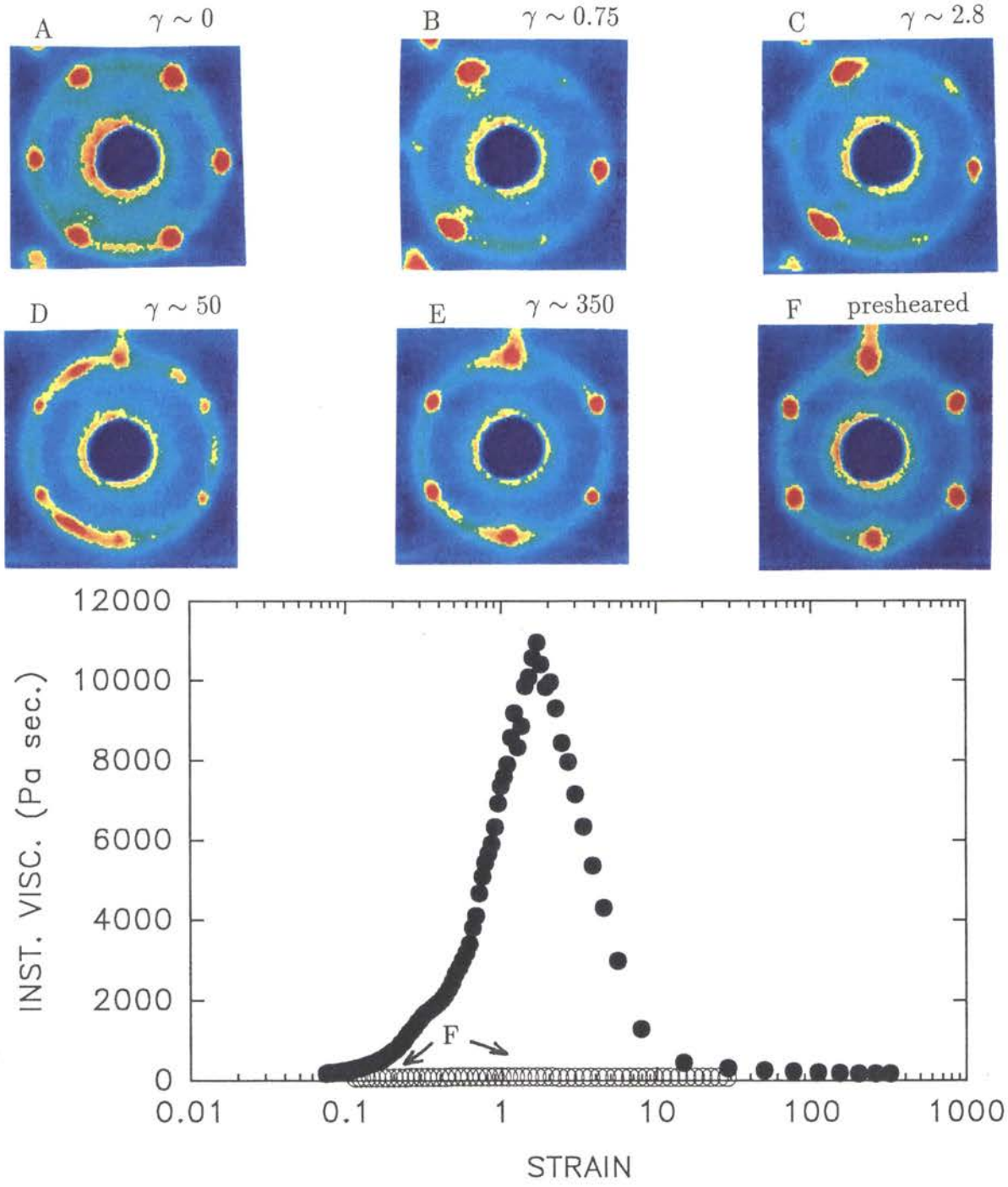

Figure 21. The instantaneous viscosity as a function of strain for microgel suspensions ($\phi^* = 1.03$, $\sigma_o = 5$ Pa) prepared in presheared and fcc microstructural states. Observed microstucture is shown by above scattering images, which correlate with the viscous response, as noted by A, B, C, D, and E. $\gamma \equiv$ strain.

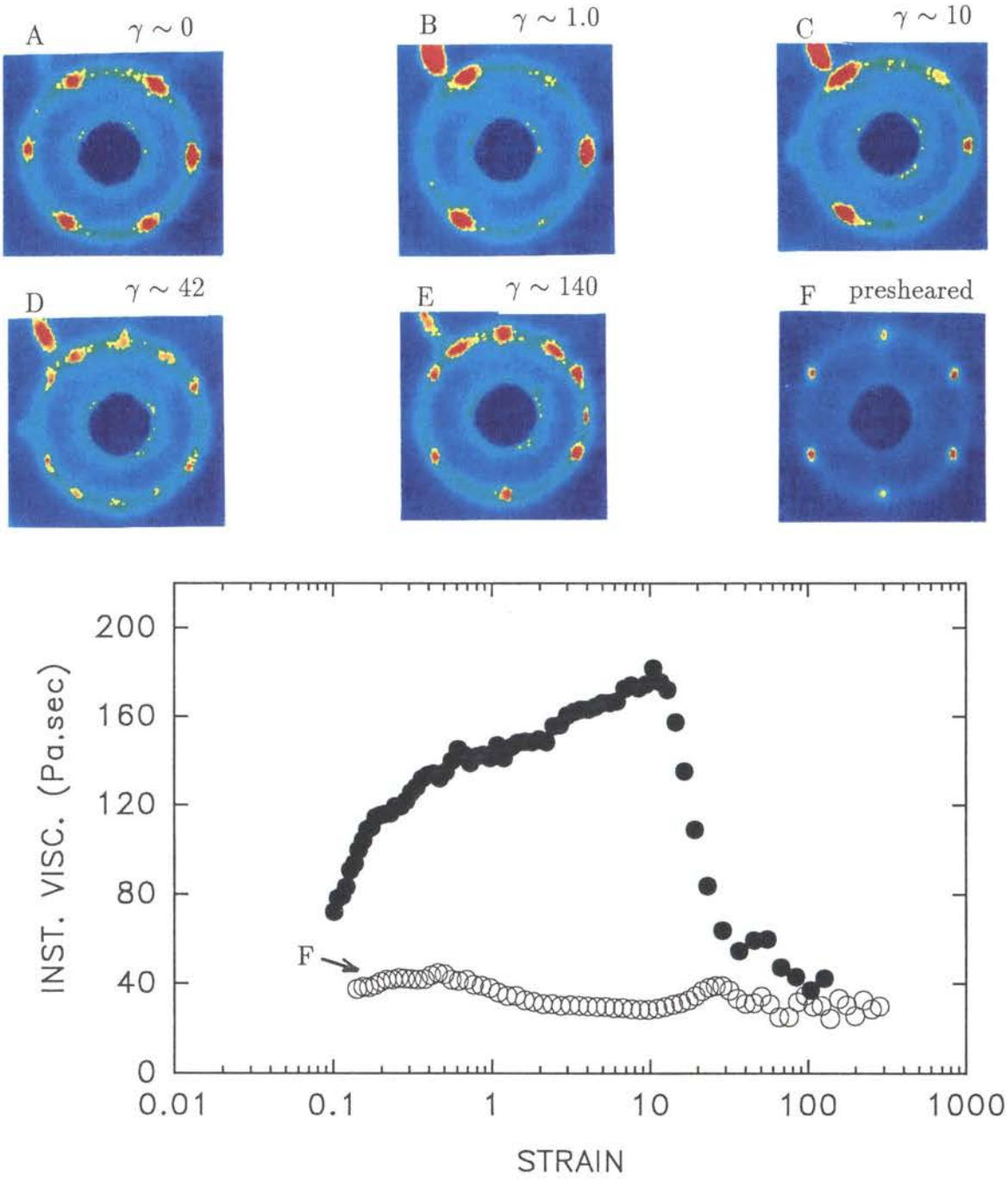

Figure 22. The instantaneous viscosity as a function of strain for microgel suspensions ($\phi^* = 0.783$, $\sigma_o = 0.40$ Pa) prepared in presheared and fcc microstructural states. Observed microstucture is shown by above scattering images, which correlate with the viscous response, as noted by A, B, C, D, and E. $\gamma \equiv$ strain.

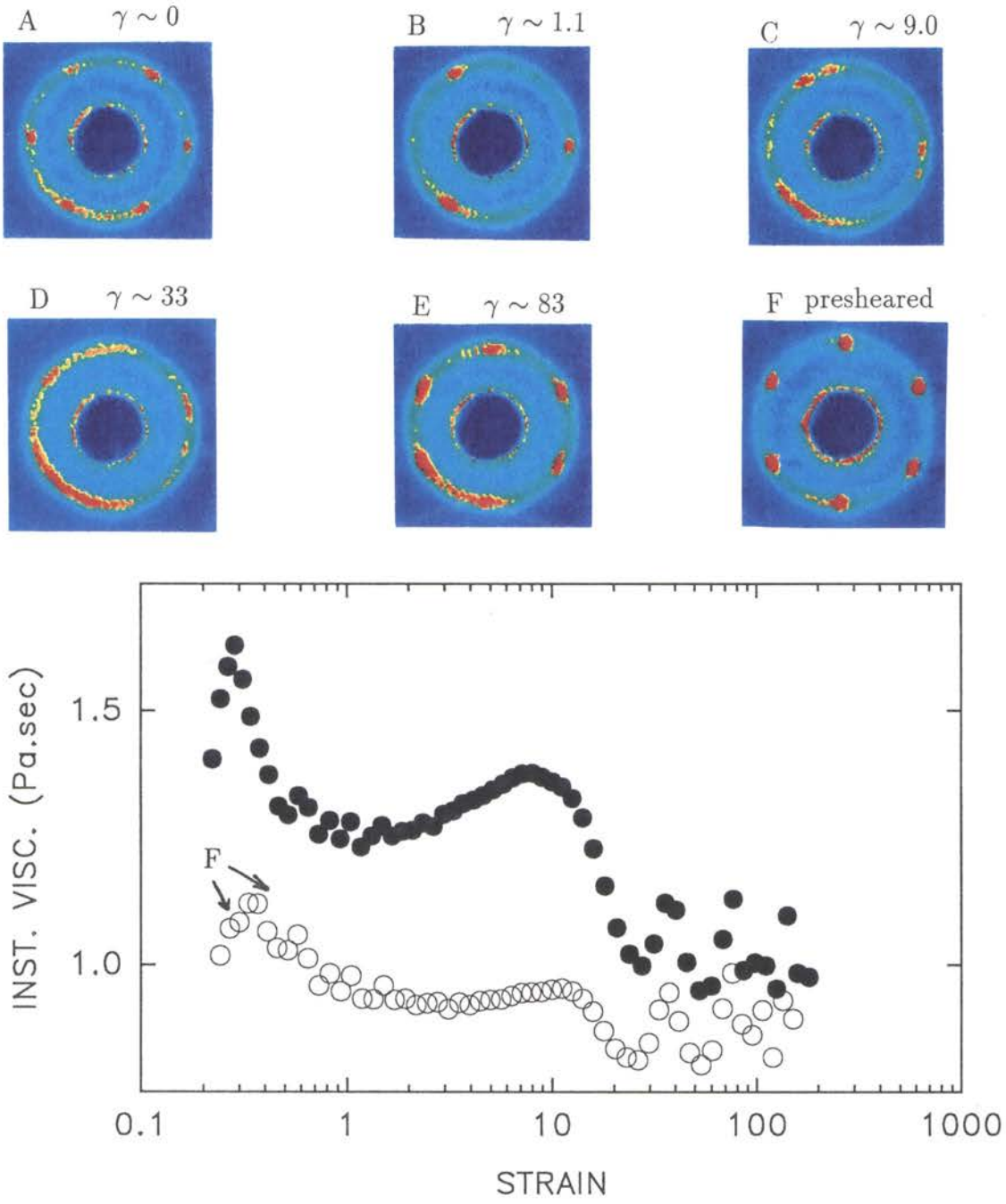

Figure 23. The instantaneous viscosity as a function of strain for microgel suspensions ($\phi^* = 0.681$, $\sigma_o = 0.25$ Pa) prepared in presheared and fcc microstructural states. Observed microstucture is shown by above scattering images, which correlate with the viscous response, as noted by A, B, C, D, and E. $\gamma \equiv$ strain.

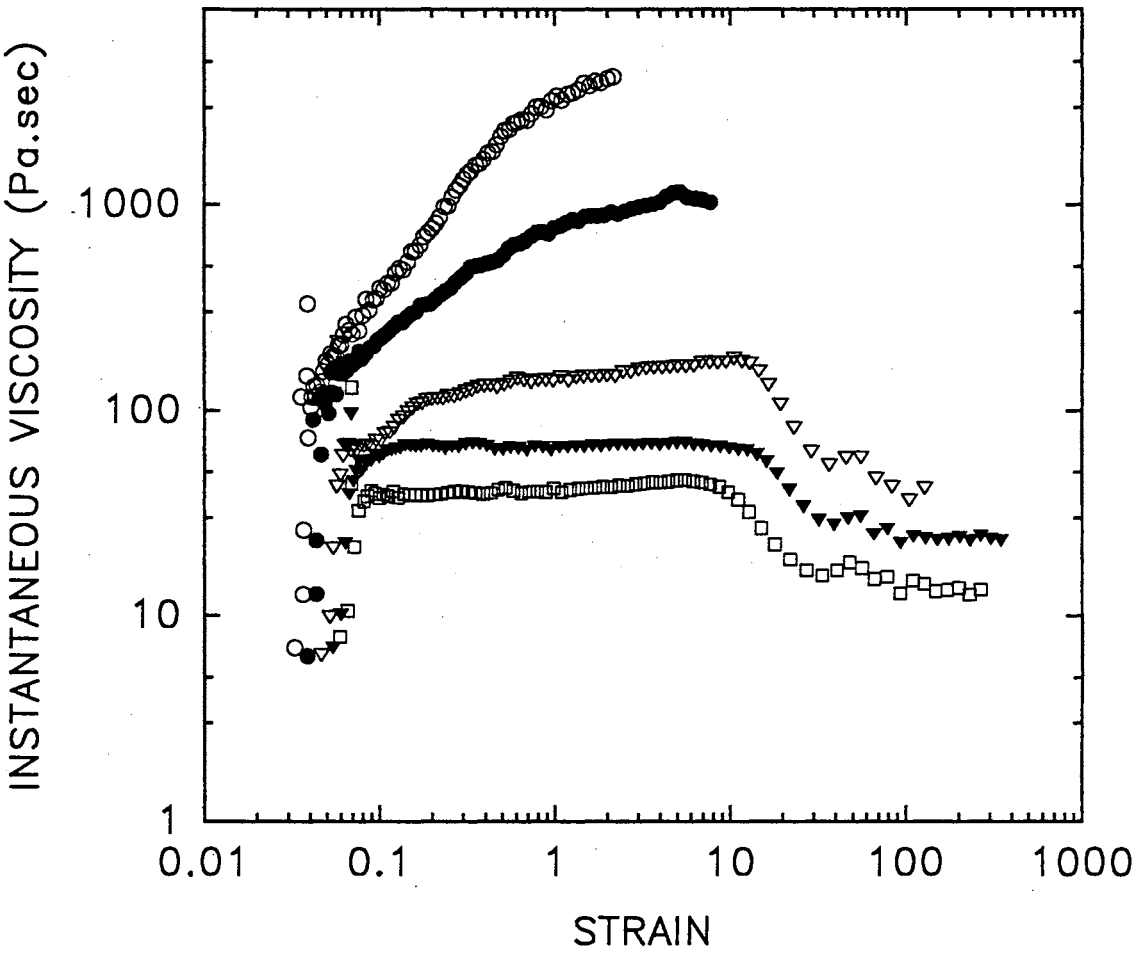

Figure 24. The instantaneous viscosity as a function of stress and strain for an fcc state, $\phi^* = 0.783$. (○) $\sigma_o = 0.3$ Pa, (●) $\sigma_o = 0.35$ Pa (▽) $\sigma_o = 0.4$ Pa (▼) $\sigma_o = 0.45$ Pa (□) $\sigma_o = 0.5$ Pa.

suspension alters its microstructure, viscously dissipating any increase in energy beyond that which it is capable of storing in a linear way. Such a mechanism could be realized in the suspensions local equilibrium particle configuration. Under applied stress, the local configuration would be altered from its "equilibrium" state, against the restoring forces due to particle deformation and perhaps randomizing effects of Brownian motion. If the suspension is strained beyond some critical value, the microstructure viscously evolves, keeping the elastic energy stored in the altered configuration constant. This is not contradictory to fact that the applied stresses are in the shear thinning regions, as any stress strain relationship can be considered linear provided the strains are small enough. These considerations are corroborated by the observations of Berry, Hager, and Wong in solutions of poly(α-methylstyrenes) [86]. Here, they find that exceeding a critical stress is a necessary but not sufficient condition to bring about nonlinear viscous flow. A critical strain must also be exceeded, which is suggestive of a viscous microstructural transition with strain. They define the following functions to describe nonlinear behavior in creep,

$$\Delta\gamma(t) = \gamma_\eta(t) - \sigma t/\eta_o \tag{28}$$

$$\gamma_\eta(t) = \sigma J_\sigma(t) - \gamma_{r,\sigma}(t,\infty) \tag{29}$$

where γ_η represents the viscous contribution to strain due to a nonlinear creep measurement, and $\sigma t/\eta_o$ the viscous contribution to strain in the linear limit. It can therefore be seen that $\Delta\gamma(t)$ represents a departure from linearity when greater than zero. Berry, Hager and Wong find that $\Delta\gamma(t) = 0$ for strains up to some critical value, γ_c, above which $\Delta\gamma(t)$ increases for their solutions. This is observed in spite of applied stresses being in the shear thinning region. Below some critical stress, of course, there is no nonlinearity found in the creep behavior, even for strains an order of magnitude larger than γ_c.

As a verification of this behavior in the microgels, it was attempted, although not expected, to find η_o for the presheared structure in the $\phi^* = 0.783$ suspension.

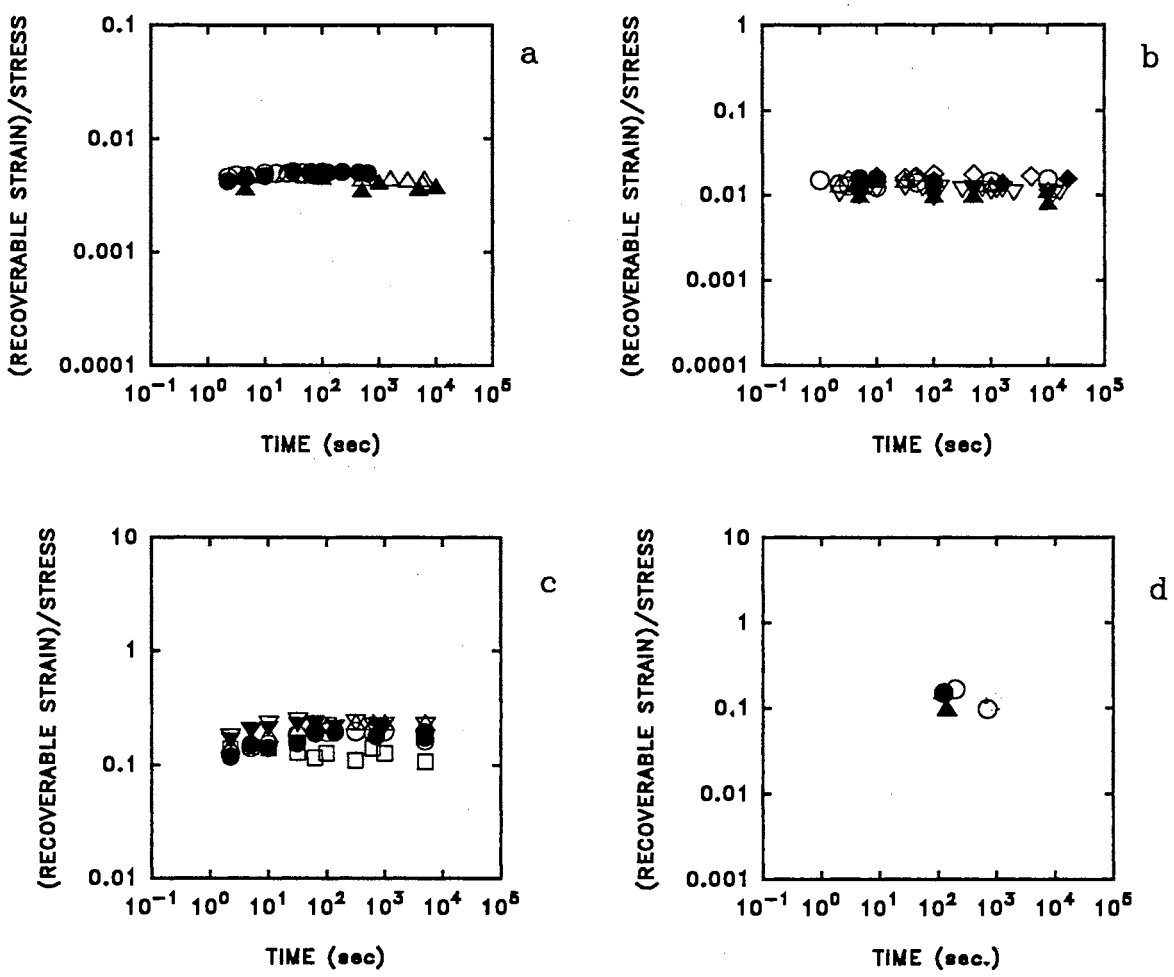

Figure 25. Total recoverable strain scaled on applied stress as a function of time, for effective volume fractions and applied stresses noted below. (a) $\phi^* = 1.22$, ◯20 Pa, △10 Pa, (b) $\phi^* = 1.03$, ◯0.14 Pa, △1.0 Pa, ▽5.0 Pa, □10.0 Pa, (c) $\phi^* = 0.783$, ◯0.14 Pa, △0.25 Pa, ▽0.5 Pa, □1.0 Pa, (d) $\phi^* = 0.681$, ◯0.14 Pa, △0.25 Pa. Open symbols represent the initial structure as presheared and closed symbols that of fcc.

Utilizing a double gap couette, it was hoped that the $\sim$ two orders of magnitude decrease in minimum applied stress afforded by this geometry, below that of the optical couette, would yieled η_o. As may be expected, the viscosity diverged at low applied stresses, becoming immeasureable for $\sigma < 0.09$ Pa. Since it becomes a philosophical question as to whether or not η_o exists for stable, glassy suspensions (i.e. apply a small enough stress and wait a long enough time) the following track was taken. Although η_o could not be measured, the results from the double gap provided a range for which it might be said 1000 Pa.sec $< \eta_o < \infty$. With this in mind, $\Delta\gamma$ is plotted versus γ, for $\eta_o = 1000$ Pa.sec and $\eta_o = \infty$, as shown in Fig. 26. In both cases, a linear region is observed for strains below $\sim 2\%$, in spite of the applied stress ($\sigma = 0.092$ Pa) being at a value which promotes shear thinning. This result warrants a similar examination in microgel suspensions of lower effective volume fracion, where η_o is defined both experimentally and conceptually. Limited sample availability prevented a complete set of these data as a function of ϕ^* and microstructure. It is interesting to note, that over all, the strain amplitude defining the linear region in a dynamic measurement (Chapter VI) is of the same order as the critical strain observed here.

Since the recovery measurements are observed to be linear, $\gamma_{r,\sigma}(t_c, \infty)/\sigma$ is the measured compliance, J^o, obtained typically from a linear creep measurement. Plotting the average value of the total recoverable strain for each stress shown in Fig. 19 versus the stress, yields a straight line. The slope of this line is a measure of J^o. Fig. 27 depicts the data for $\phi^* = 1.22, 1.03$ and 0.783 along with their respective linear fits. The $\phi^* = 0.681$ data is too incomplete and is not shown. A comparison of $1/J^o$ with the measured value of G' at $\omega = 1$ and 0.006 rad/sec. is shown in Fig. 28. Although J^o is typically measured at strains associated with the nonlinear region, and on a time scale shorter than that probed in the dynamic measurements, agreement between the two is observed.

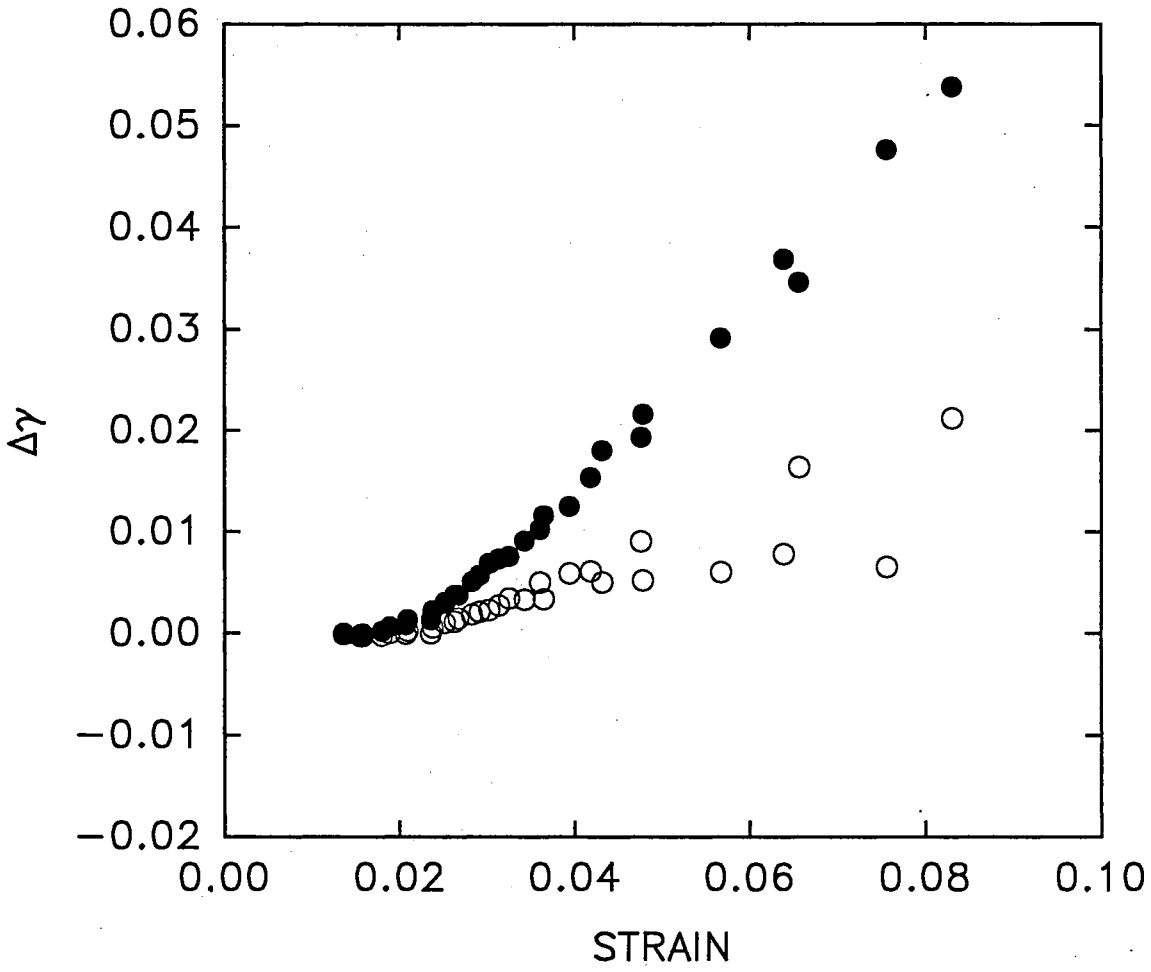

Figure 26. The nonlinear response function, $\Delta\gamma$ as a function of strain for the $\phi^* = 0.783$ sample. The applied stress is $\sigma = 0.092$ Pa. ○ $\eta_o = 1000$ Pa.sec, ● $\eta_o = \infty$.

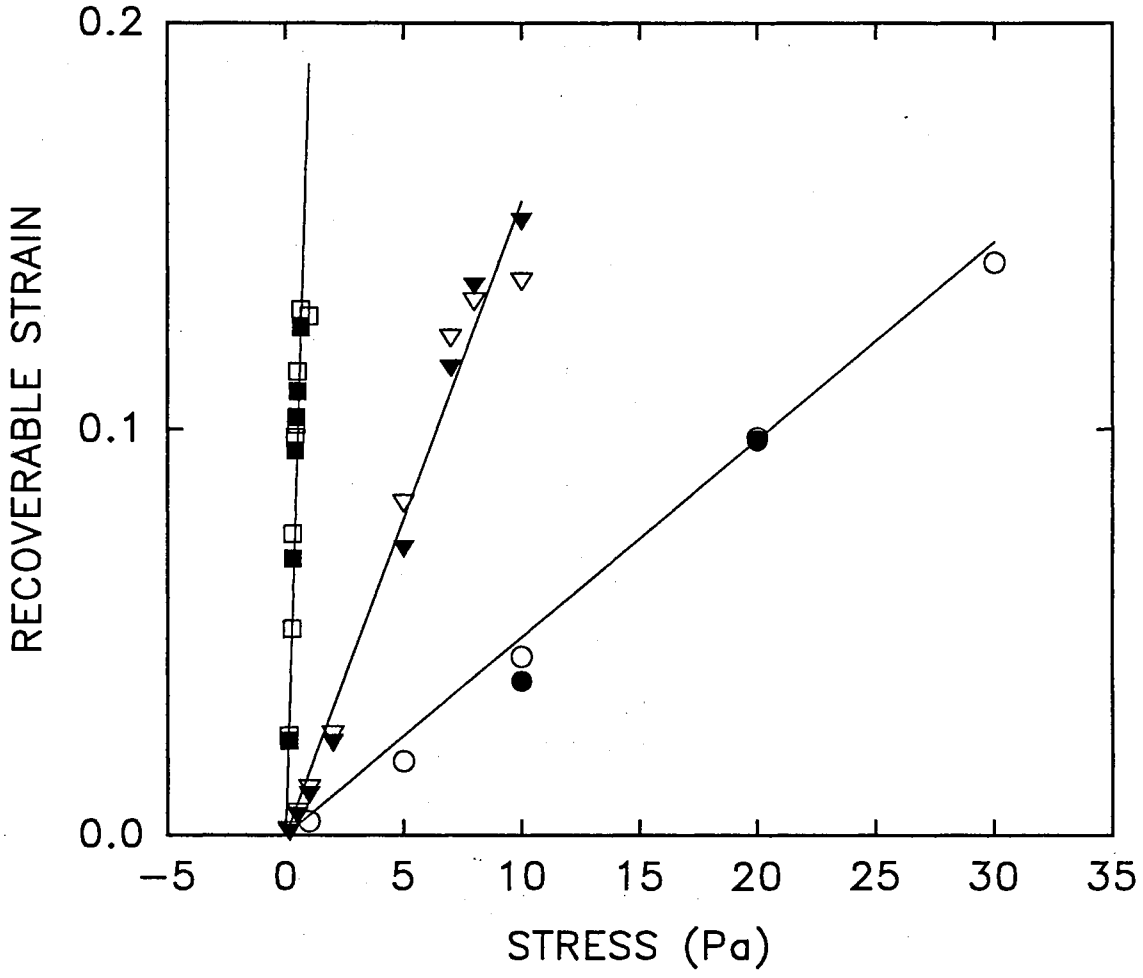

Figure 27. Measured recoverable strain versus applied stress for ○ $\phi^* = 1.22$, ▽ $\phi^* = 1.03$, □ $\phi^* = 0.783$. The open and filled symbols represent the presheared and fcc structures, respectively. - Least squares fit from which the slope yields J^o.

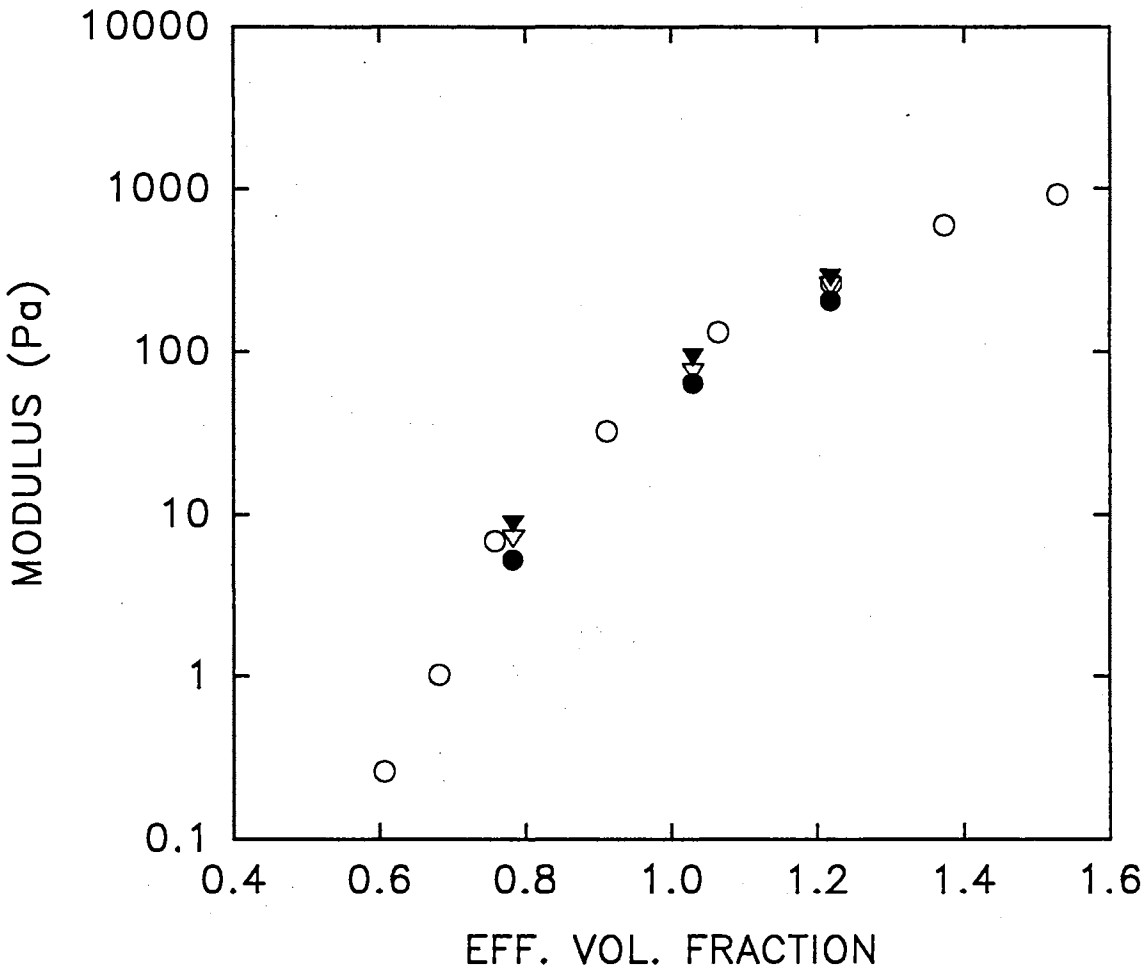

Figure 28. Measured suspension moduli versus ϕ^*. ○ G' at $\omega = 1$ rad/sec from the data of Wolfe. ○ $1/J^o$ from recovery measurements. ▽ G' at $\omega = 0.006$ rad/sec from data of this study. Open and closed triangles represent presheared and fcc microstructures, respectively.

CHAPTER VI

DYNAMIC OPTO-RHEOLOGY

Introduction

The steady state measurements of Chapter 5 are structure evolving. Equilibrium measurements could not be made in the sense that steady shear perturbed the microstructure at even the lowest possible applied stresses. By applying an oscillatory stress over a range of frequencies rather than a constant stress, this problem can be circumvented as the suspension is probed over a large number of time scales. In this way, suspension behavior ranging from elastic to viscoelastic to viscous may be examined within the context of a single measurement. If the frequency is high enough and the strain small enough, such measurements can probe the "equilibrium" structure in a non perturbative way, providing insight into interparticle interactions and the equilibrium modulus, G_o. Low frequencies probe the dissipative nature of the suspension, yielding a measure of the low shear rate viscosity, η_o, if indeed such a region is present.

The evolution of microstructure as it is observed in the creep measurements of Chapter V is a rheologically nonlinear phenomena. In this chapter, a similar evolution is examined dynamically. The interpretation of nonlinear results will be qualitative and in the form of recongnized patterns. Linear behavior is examined within the context of its usual meaning.

Dynamic Rheology

The dynamic moduli may be derived beginning from the same stress strain relationship examined in the creep and creep recovery measurements,

$$\sigma(t) = \int_0^t G(t-\tau)\frac{d\gamma(\tau)}{d\tau}d\tau \tag{30}$$

where now a time varying strain history is applied,

$$\gamma(t) = \gamma_o \exp^{i\omega t}. \tag{31}$$

Consistant with the constitutive form found previously, the stress may be written as

$$\sigma(t) = |G^*(i\omega)|\gamma_o \exp^{i(\omega t+\phi)} \tag{32}$$

where ϕ is a phase shift between the applied strain and response in stress. $G^*(i\omega)$ is known as the complex modulus, which may be further decomposed into its real and imaginary components,

$$G^*(i\omega) = G'(\omega) + iG''(\omega). \tag{33}$$

Here, G' and G'' are termed the storage and loss modulus, respectively. In a sense, they represent the storage and dissipation of energy in a dynamic measurement. Generally, it is the high and low frequency limits of the dynamic moduli which are of interest, as they represent the equilibrium modulus, G_o or zero shear rate viscosity, η_o, respectively. If the relaxation function, $G(t)$, is represented as in Chapter V,

$$G(t) = G^o + \hat{G}(t) \tag{34}$$

then it may be shown that the following limits exist [85],

$$\begin{aligned} G'(0) &= G^o \\ G''(0) &= 0 \end{aligned} \tag{35}$$

and

$$\begin{aligned} G'(\infty) &= G^o + \hat{G}(0) = G_o \\ G''(\infty) &= 0. \end{aligned} \tag{36}$$

The above expressions point out the peculiar behavior of viscoelastic material and the importance of time scales. As can be seen, viscoelastic solids behave as elastic solids at both short and long time scales, where as viscoelastic fluids behave viscously for slow processes and elastically for fast processes. Further, a complex viscosity may be defined as

$$\eta^*(\omega) = \eta^{'}(\omega) - i\eta^{''}(\omega) \tag{37}$$

in which $\eta^{'}$ may be related to the dissipation of energy [88] and is termed the dynamic viscosity. Since very low frequency, small amplitude oscillations can be considered nearly steady flow, $\eta^{'}(\omega \rightarrow 0) = \eta_o$.

In a standard simple shear dynamic measurement, the magnitude of the applied strain, sample stress response and phase angle is measured, yielding a measure of G^*,

$$G^* = \frac{\sigma_o}{\gamma_o} \exp^{i\phi} = \frac{\sigma^*}{\gamma^*}. \tag{38}$$

The measurements made in this chapter were under an applied oscillatory stress, rather than strain. However, the analysis and applicability of the above equations is the same. In the case where nonlinear behavior is examined, these results do not hold.

Dynamic Measurements

The sample preparation, effective volume fractions and scattering geometry are identical to those described in Chapter V. The microstructures termed 'pres-heared' and 'fcc' are as described in that chapter. Here, a sinusoidal stress was applied in lieu of the constant stress. The output strain response and phase shift

between the stress and strain were monitored. Fourier transforming the strain response results in relative contributions of higher order harmonics and observations of a departure from linearity.

Two sets of data were routinely taken for each effective volume fraction examined. One set consisted of measurements at a constant frequency, but over a predetermined range in strain. Examination of the magnitude of G^* resulted in determination of the linear region for each sample. The region in strain where the dynamic modulus is constant yields the linear viscoelastic region. Typical values of frequency examined were 5 Hz to 0.001 Hz, over a range in strain of 1% to 1000%. Sample response could be monitored as a function of microstructure and effective volume fraction, through the linear and into the nonlinear viscoelastic regions. Since the microstructure typically evolves with increasing strain, all measurements were started at small strains, which gradually increased as the applied stress was increased. Similarly, holding the applied stress constant and sweeping through a series of frequencies results in the frequency response of the suspension. Depending on the stress, the measurement either probed the linear, nonlinear, or combination of both, viscoelastic regions. Here, the measurement was begun at high frequencies, probing small amplitudes and gradually decreased, probing larger strains.

Results and Discussion

Rheological behavior observed in the evolution of specific microstructural states is inherently nonlinear. However, the linear region may be examined if the applied strains are sufficiently small. One must therefore know what the upper bound on strain is and remain below that critical value, γ_c. The 'plateaus' associated with the linear viscoelastic region of the microgels examined are shown in Fig. 29 and 30, where G' and G'' are shown plotted versus strain for $\phi^* = 1.218$, 1.03, 0.783, and 0.681. Here, the oscillation frequency associated with each graph is $\omega = 1$, 0.1, 0.01 and 0.001 Hz. The open and closed symbols are for initial microstructures termed presheared and fcc, respectively. For the three largest effective volume fractions, $G' > G''$ at all frequencies, indicating the microgels are

behaving more elastically than viscous. In the case of $\phi^* = 0.681$, G' is only slightly larger than G'', indicating a relative viscous response above that of the higher concentration samples. Note that the linear region could not be reached for the $\phi^* = 0.681$ sample for $\omega > 1$ Hz. A stress small enough to insure linearity could not be applied here.

Evidence for the effect of microstructure on the linear and nonlinear regions is sought through examination of G' and G''. In the linear region, it is observed that the moduli are not greatly affected by microstructure, except for a slight shift in G' to larger values for the fcc structure, perhaps indicating the fcc orientation to be a more rigid structure. It is not clear why this trend is violated for the $\phi^* = 1.218$ sample at 0.1 Hz and 0.01 Hz. This sample certainly does not exhibit this behavior when examined in a frequency sweep measurement (see Fig. 32) and is likely due to an unknown experimental difficulty. No similar clear distinction can be made for G''. The scattering images associated with this region indicate only a slight departure of the initial fcc microstructure from its quiescent state. The Fourier transform of the strain response also indicates linearity of the system in this region. These results are perhaps not surprising. Linear measurements are presumably displacing the particles only slightly from there equilibrium positions and due to the random stacked nature of each initial microstructure, they should have approximately the same amount of free volume to move around. Also, imperfections which must surely exist in each of the microstructures may tend to average out any deviations. However, since the closest packed direction relative to the shear flow direction is different for each microstructure, some difference is expected. The plateau in G' is observed to shift to slightly smaller strains and its value increase in magnitude as the effective volume fraction increases, which intuitively agrees with the importance of interparicle interactions at higher concentrations. Although the gross evolution of microstructure observed in the scattering measurements made in this study are too insensitive to distinguish where the nonlinear regions begin for each effective volume fraction, the plots of G' versus strain shown yield this information directly. A measure of where the linear region ends as a function of

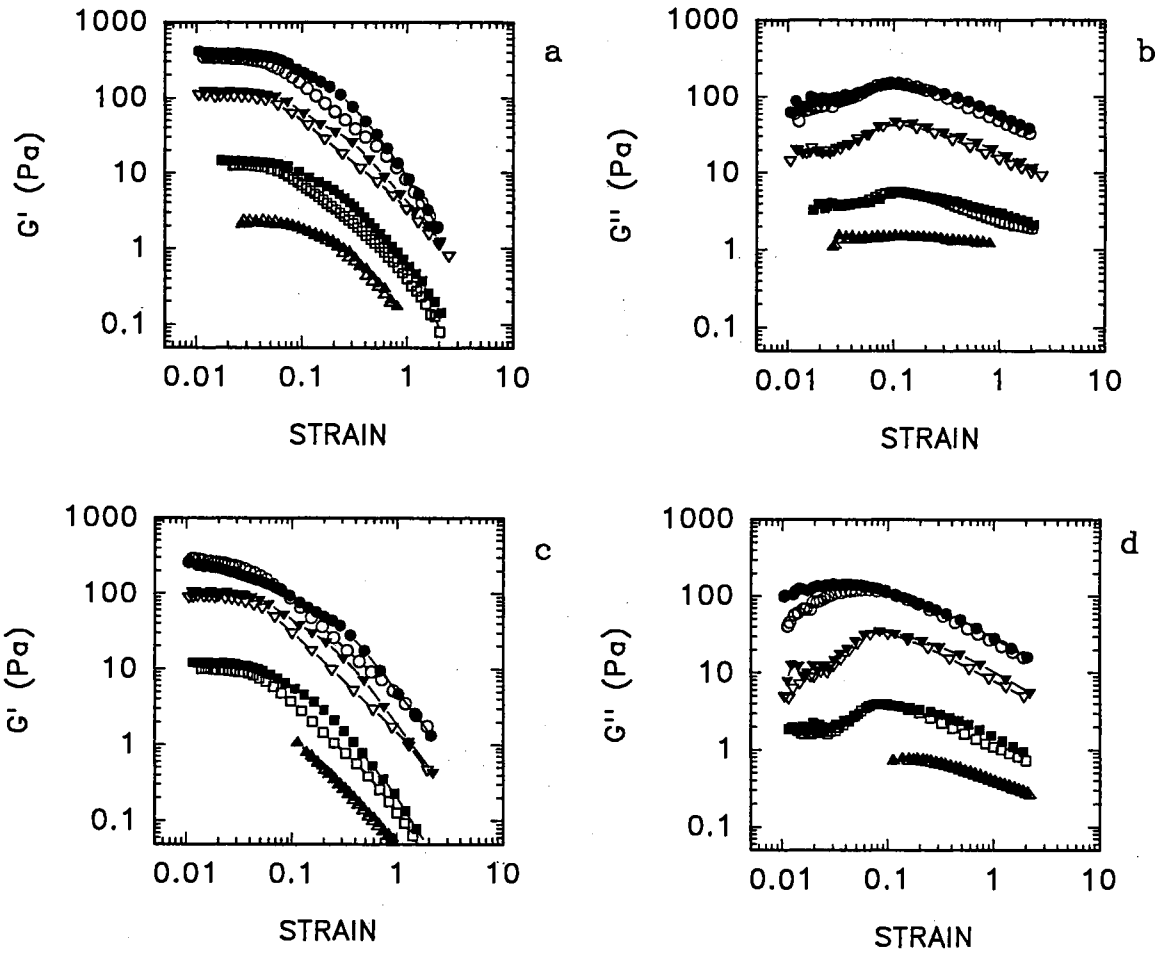

Figure 29. The (a,c) storage and (b,d) loss moduli versus strain for an oscillation frequency of 1 and 0.1 Hz, respectively. ○ $\phi^* = 1.218$, ▽ $\phi^* = 1.03$, □ $\phi^* = 0.783$, and △ $\phi^* = 0.681$. The open and closed symbols indicate presheared and fcc initial microstructural states, respectively.

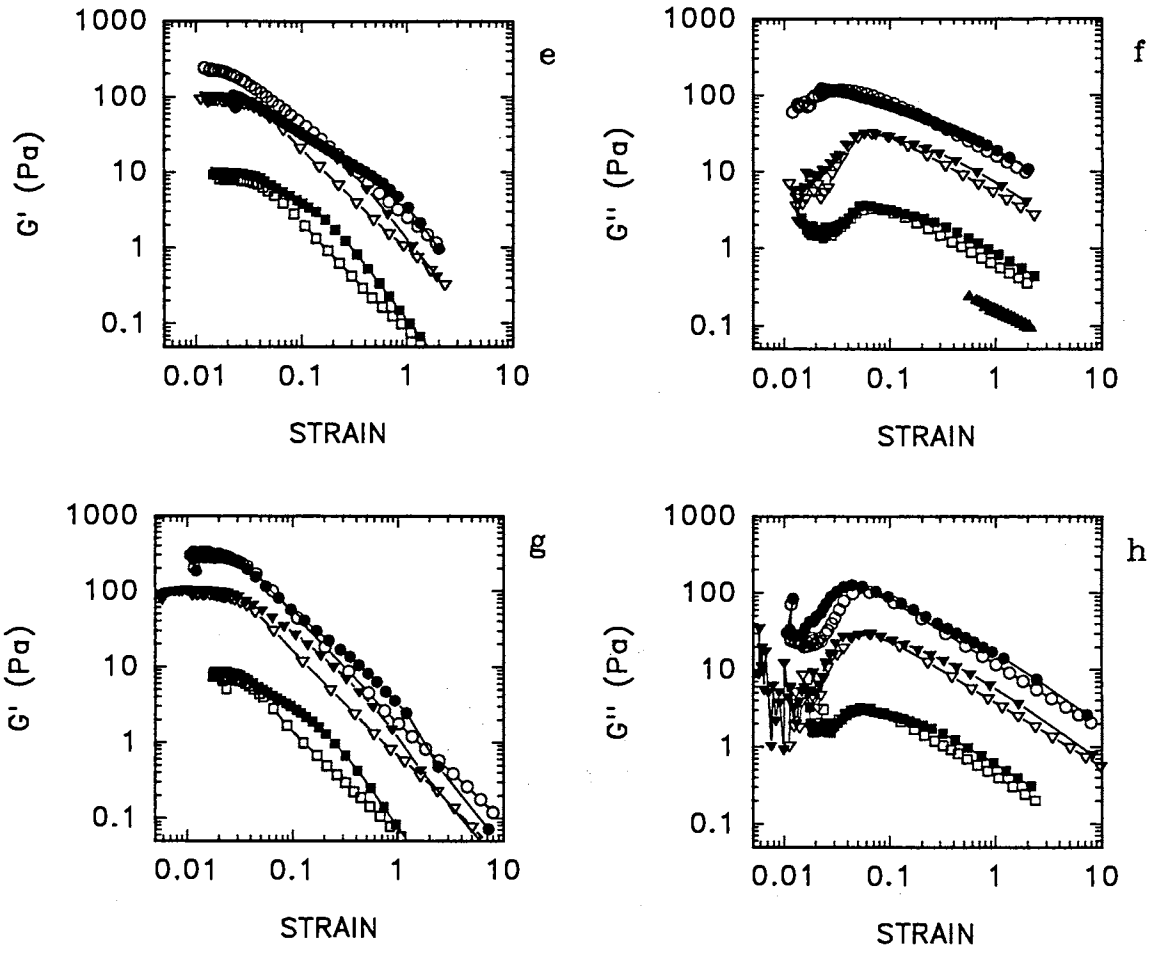

Figure 30. The (e,g) storage and (f,h) loss moduli versus strain for an oscillation frequency of 0.01 and 0.001 Hz, respectively. ○ $\phi^* = 1.218$, ▽ $\phi^* = 1.03$, □ $\phi^* = 0.783$, and △ $\phi^* = 0.681$. The open and closed symbols indicate presheared and fcc initial microstructural states, respectively.

volume fraction is shown in Fig. 31. Here, the critical strain is termed the strain above which G' breaks from linearity. The strain at which G' begins to fall roughly 2 to 5% below a line drawn at the plateau value determines the break. Although perhaps crude, a trend is clearly present. Differences between the presheared and fcc initial microstructures were not clearly resolveable.

The insensitivity of G' with frequency for a given effective volume fraction is shown in Fig. 32, where within the linear region, the suspension is probed over a range of frequencies. This insensitivity has already been noted in Chapter III, in reference to the results of Wolfe. Here, however, it is also observed that G' is relatively insensitive to microstructure. As shown, moduli for the presheared and fcc microstates track one another, with only a slight increase in those of the fcc above that of the presheared. The uncomplicated behavior of the moduli further indicate that the suspensions are behaving in a 'elastoviscous' manner. That is, their elastic properties are dominating the viscoelastic behavior. Given the high concentration and extremely (if existant at all) limited amount of particle diffusion possible, it seems reasonable that dynamic behavior of the microgels would appear largely elastic even at frequencies of 0.001 Hz. Data could not be obtained in the linear region for $\phi^* = 0.681$ sample, as a low enough stress could not be applied to insure linearity.

As shown in Fig. 33, the dynamic viscosity appears to indicate a divergence in $\eta_o = \eta^*(\omega \rightarrow 0)$ at all effective volume fractions and for both microstructures examined. Also shown is the steady state results for η, which can be seen does not mirror the dynamic result. Thus, the Cox-Merz rule does not apply in the microgel suspensions examined [89].

Beyond the linear region, any interpretation of the moduli is tenuous at best. Previous studies have attempted to predict nonlinear behavior of G' with little success [90,91]. However, for the microgels there may be trends which can be examined in light of the underlying microstructure. It is observed that the deviation of G' in the nonlinear region, between the presheared and fcc structures, is generally characteristic of twinning in the fcc miscrostructure. The images shown

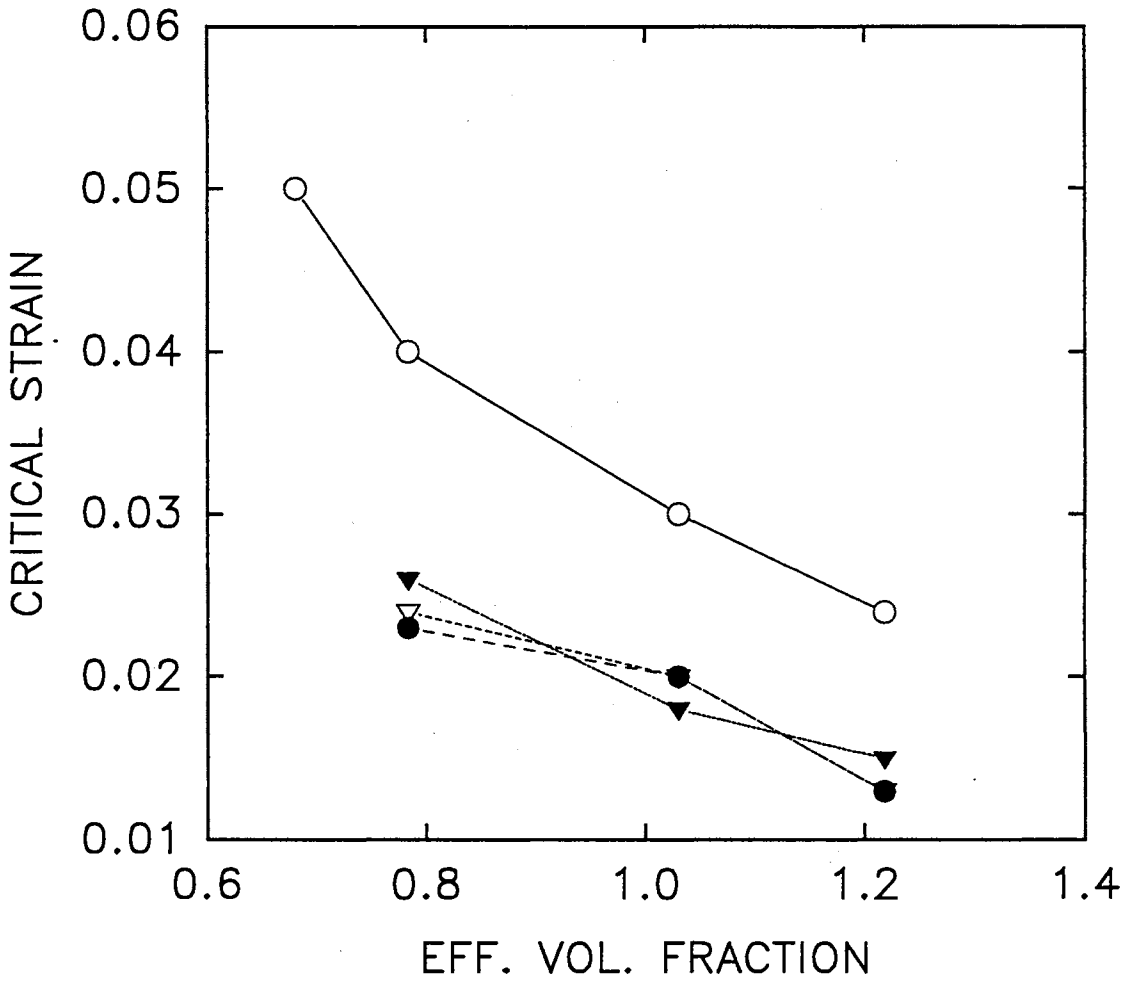

Figure 31. The critical strain as a function of effective volume fraction and frequency. ○ ω = 1.0Hz, ● ω = 0.1Hz, ▽ ω = 0.01Hz, ▼ ω = 0.001Hz.

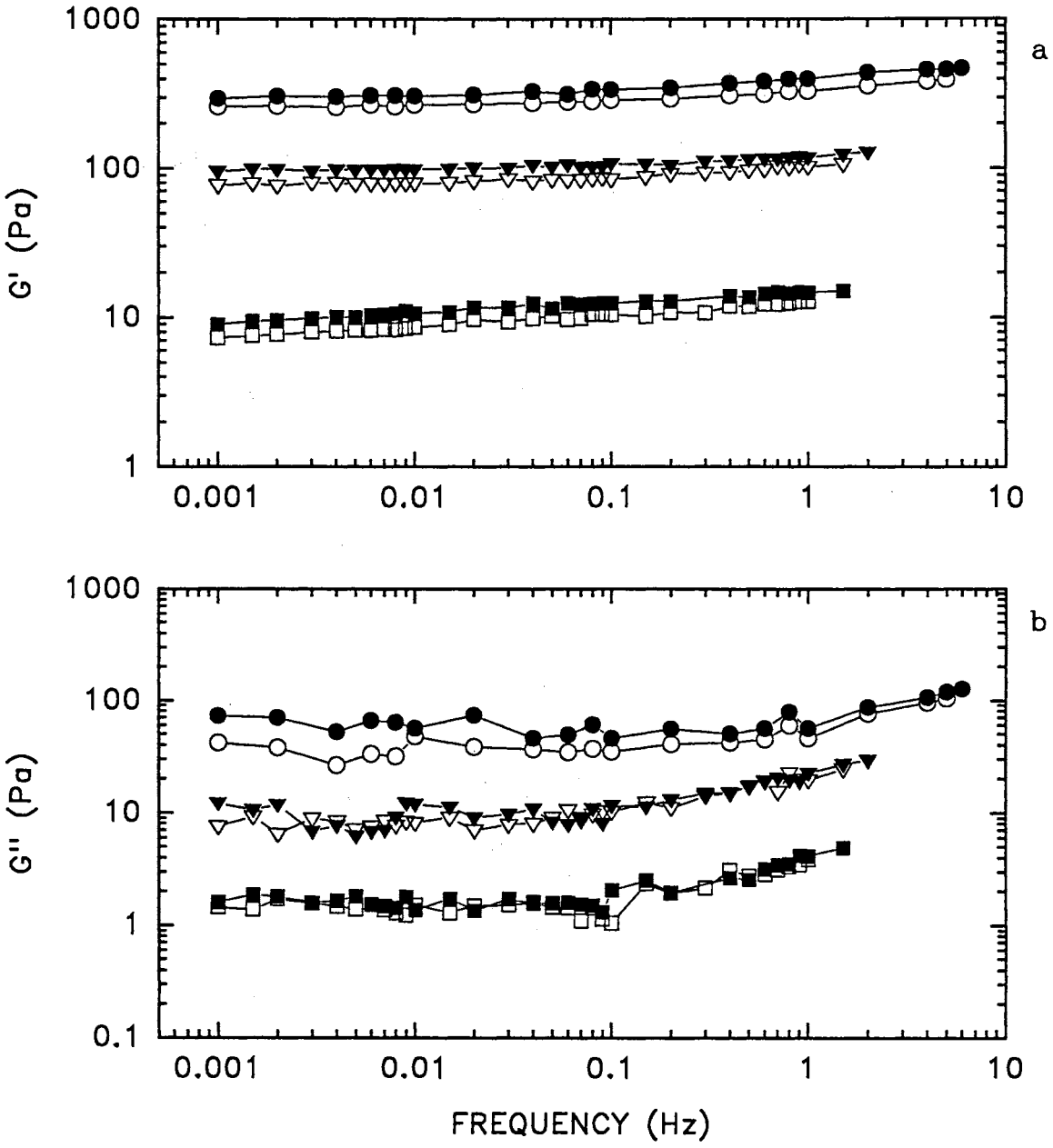

Figure 32. The (a) storage and (b) loss moduli versus frequency. ◯ $\phi^* = 1.218$, ▽ $\phi^* = 1.03$, □ $\phi^* = 0.783$. The open and closed symbols indicate presheared and fcc initial microstructural states, respectively.

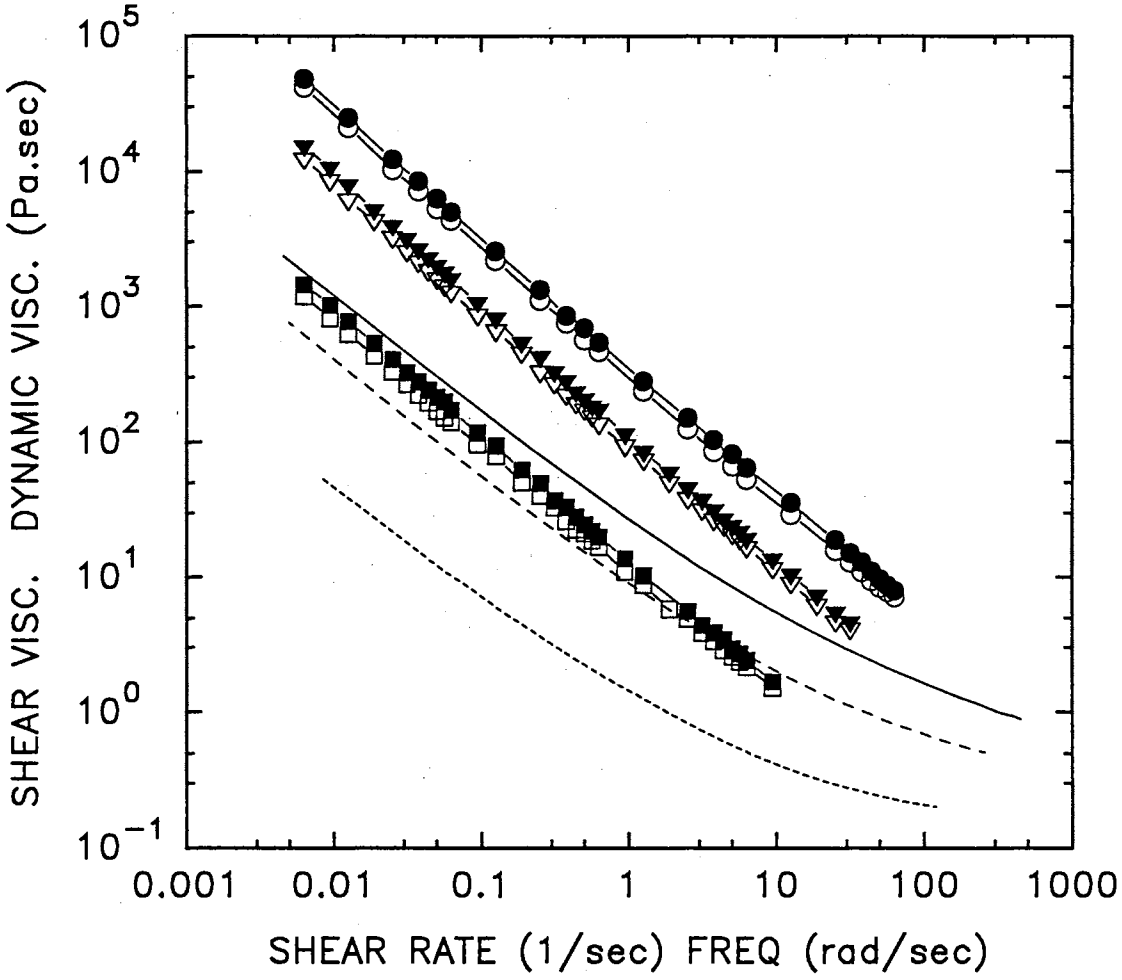

Figure 33. The dynamic (symbols) and steady state (lines) viscosity for ○ $\phi^* = 1.218$, ▽ $\phi^* = 1.03$, □ $\phi^* = 0.783$. The open and closed symbols indicate presheared and fcc initial microstructural states, respectively. The solid, long and short dashed lines represent decreasing ϕ^* at the values noted above.

in Fig. 34 document the typical evolution of microstructure from the fcc to the presheared structure, with increasing strain. They correspond to the moduli for $\phi^* = 1.03$, $\omega = 1$ Hz shown in Fig. 29. Here, it can be seen that while G' does indicate a microstructural change occuring, it does not correlate well with the observed scattering much beyond a strain of 0.8. This can be observed by comparing the scattering image for $\gamma = 1.6$ of Fig. 34d with the corresponding G' from Fig. 29a. Here, G' for the presheared and fcc structures appear to be merging together at a point where the evolution in microstructure seems to be the most dramatic. One may argue that G'' is showing behavior which indicates this change. That is, G'' shows differences at values in strain coincident with this evolution. However, the data is not conclusive in this regard. This poor correlation between the moduli in the nonlinear regin and observed microstructure is also evident in other effective volume fraction samples and at other frequencies. This is, of course, not to say that microstructure does not effect the rheology in the microgels. The results of the creep measurements indicate otherwise. It must be remembered that G' and G'' are quantities defined strictly in the linear region. Using the fundamental from the response spectrum under the assumption that it corresponds to the usual G' of linear viscoelasticity is in error. It has been demonstrated that for a viscoelastic system driven into the nonlinear regime, even the first harmonic is affected [87]. A true set of nonlinear material functions which properly account for higher order harmonics may indicate a stronger dynamic dependence of the material on microstructure. However, the physical meaning of such functions may not be so readily identifiable as the storage and loss moduli of the linear theory.

It is observed that the lower the applied frequency, the larger the strain required to evolve the fcc microstructure into a mixed state. Again, however, the behavior of the storage modulus for the fcc structure as a function of strain does not yield a correlation with the scattering. This is evidenced in Fig. 35. Here, the loss and storage moduli for the $\phi^* = 1.03$ at 1 and 5 Hz are plotted for comparison. As shown by the accompaning scattering images for $\gamma \sim 0.8$, the moduli do not

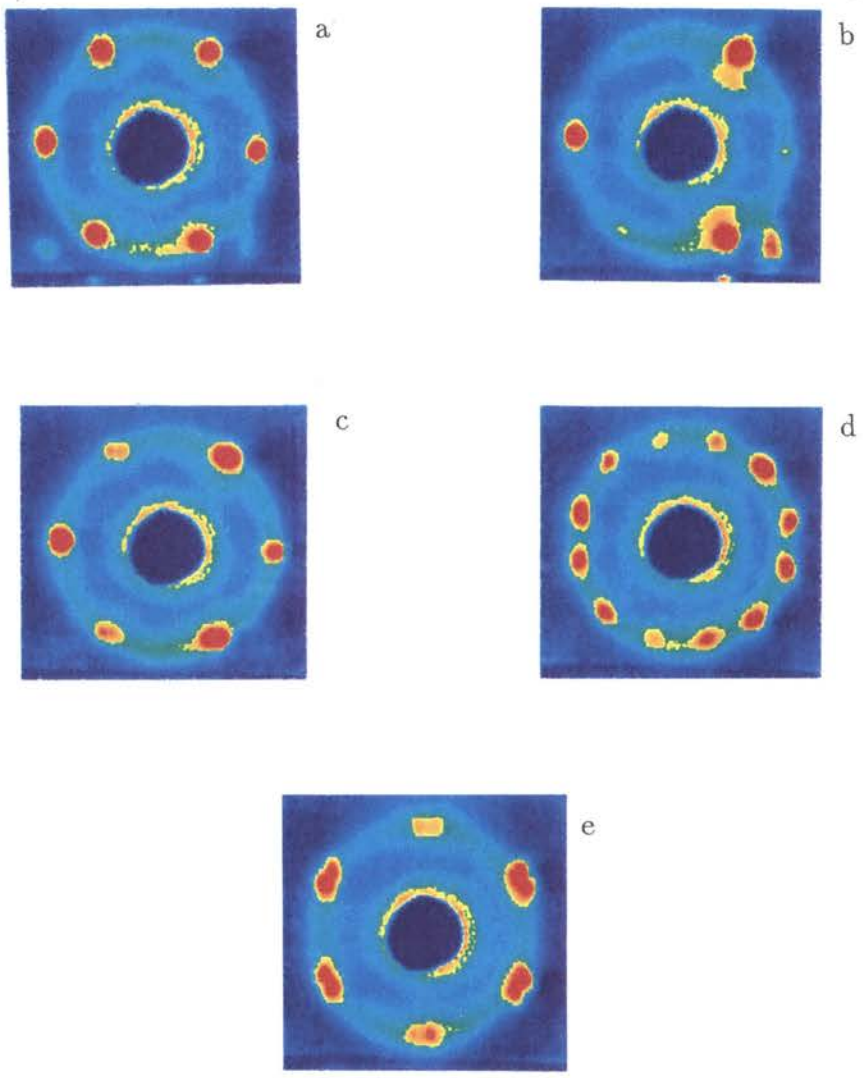

Figure 34. Evolution of $\phi^* = 1.03$ sample at 1 Hz. (a) $\gamma = 0$, (b) $\gamma \sim 0.2$, (c) $\gamma \sim 0.85$, (d) $\gamma \sim 1.6$ (e) $\gamma \sim 6.6$

reflect the relative underlying differences in microstructure between the presheared and fcc observed for each frequency. It cannot be determined whether or not this strain/evolution effect is dependent on the frequency or applied stress. They are unfortunately coupled in the nonlinear region. The higher frequency requires a larger applied stress in order to reach the same strain amplitude as a lower frequency run.

Examination of the Fourier transformed strain response at a given frequency yields the results shown in Figs. 36 - 42. Here, the higher order harmonics normalized by the fundamental are plotted as a function of strain. The axis labeled 'harmonics' represents $\omega_1, \omega_2, \omega_3...$, which are the first, second, and third, ... harmonics generated, respectively. The vertical axis is the amplitude of each harmonic normalized by the amplitude of the fundamental. Generally, it is observed that higher order harmonics appear in the suspension response at points roughly coincident with the onset of nonlinear behavior in the moduli. Although this may not be surprising, several points of observation can be made concerning the less expected behavior. For each effective volume fraction, it is observed that the contribution of higher order harmonics decreases with increasing frequency of oscillation, independent of whether or not the strains are sufficiently large that the moduli and scattering clearly indicate the measurement to be in the nonlinear regime. This also occurs independent of the microstructure (i.e. both the fcc and presheared states show the same behavior). In connection with this observation, it is also found that for those frequencies which do show harmonic content in the nonlinear region, the harmonic contribution consistently decays with increasing strain. Examining the effect of concentration at a given frequency, it is found that as the effective volume fraction is decreased, this decay becomes more rapid in strain, with the higher order harmonics eventually disappearing altogether. The frequency at which the harmonics disappear also decreases with decreasing effective volume fraction. This apparent complicated dependence on concentration, frequency and strain can be understood by considering the applied stress.

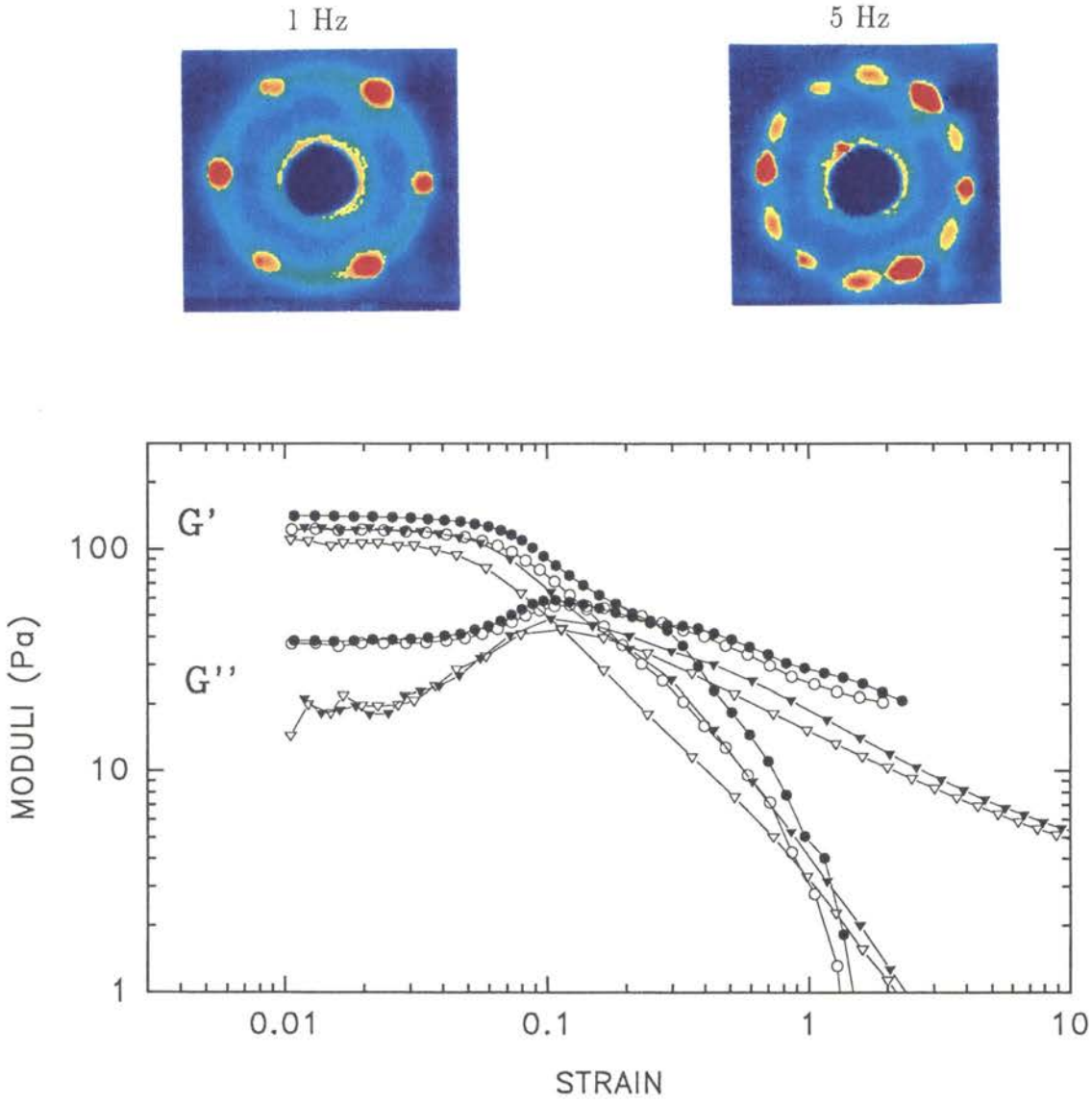

Figure 35. The loss and storage moduli for $\phi^* = 1.03$ at $\omega = 1$ Hz and 5 Hz. The scattering images depict microstructure at nearly the same value of strain, $\gamma \sim 0.8$. $\bigcirc$ $\omega = 5$ Hz, $\bigtriangledown$ $\omega = 1$ Hz. Open and closed symbols represent presheared and fcc structures, respectively.

Since these are nonlinear measurements, the stress, strain and frequency are coupled in a complicated way. In an attempt to understand why higher order harmonics appear and disappear with frequency, the corresponding stress behavior as a function of strain was examined for each frequency. It is here that the key to the behavior of the observed higher order harmonics resides. If the stress is sufficiently large, the higher order harmonics are quenched, independent of the strain. For a given frequency, as the stress is increased (thus increasing the strain), the higher order harmonics decrease until vanishing. For the sake of discussion, let this stress be represented as σ_C. If the frequency is high enough such that the stresses associated with the linear region are greater than σ_C, then no higher order harmonics will be observed, even into the nonlinear region. That is, by the time the system reaches the nonlinear region in strain, the applied stresses to get it there are large enough to diminish any higher order harmonics. On the other hand, if the frequency is reduced, thus reducing the necessary stress required to maintain linearity in strain, the system may evolve into the nonlinear region at stresses which are smaller than σ_C. In this case, the system will develop higher order harmonics, which may decay with increased strain, as the stress increases up to and beyond σ_C.

Unfortunately, σ_C must be concentration dependent, which would describe the observed effect of concentration on the frequency at which the harmonic contributions tend to disappear. That is, the stress which quenches the higher order harmonics is observed to be smaller for a lower concentration sample, when compared to a more concentrated sample at the same frequency. Examination of the critical stress at different frequencies for a given effective volume fraction, indicates it to also be frequency dependent. It is not clear why the stress appears to govern the harmonic content, while the dynamic moduli show nonlinearities. Since these observed effects appear to change with effective volume fraction, it is believed that they are not an artifact of the measuring aparatus. At the time of this writing, the physical underlying process is not understood. The data is sketchy at best and further analysis and thought is required to fill in much of the missing framework.

The microstructure associated with the Fourier analysis provides an additional piece of information. For the fcc microstructure, twinning between the ABCABC... and ACBACB... stacking appears to occur at about the initial peak in harmonic content. However, the occurence of a similar peak for the presheared structure, indicates perhaps local microstructure is governing the suspensions departure from linearity and not the 'global' structure observed in the scattering. When higher order harmonics are present, the shear induced microstructure does not initially appear to greatly effect the harmonic content of the strain response. The presheared and fcc structures are not dramatically different, even though the scattering is quite unique for the evolution of each structure. There is, however, a slight dip observed in the amplitude of the higher order harmonics for the fcc structure as the strain is increased. This dip is consistently observed for all samples where the higher order harmonic content has not been quenched. The observed scattering in the dip is still twinning fcc, with a distortion of this structure as the harmonic amplitudes begin to again increase. This is shown in Fig. 44 for the $\phi^* = 1.03$ sample at a frequency of 0.1 Hz, and is typical observed behavior in the microgel suspensions. Consistent with the observation that the fcc microstructure distorts at smaller strains with increased frequency, the dip is found to shift to smaller strains as the frequency is increased.

The harmonic behavior of the strain response appears to reasonably correlate with the underlying microstructure, where as the linear moduli do not. This is expected as the harmonic data represents the fundamental data, uncorrupted by a linear analysis.

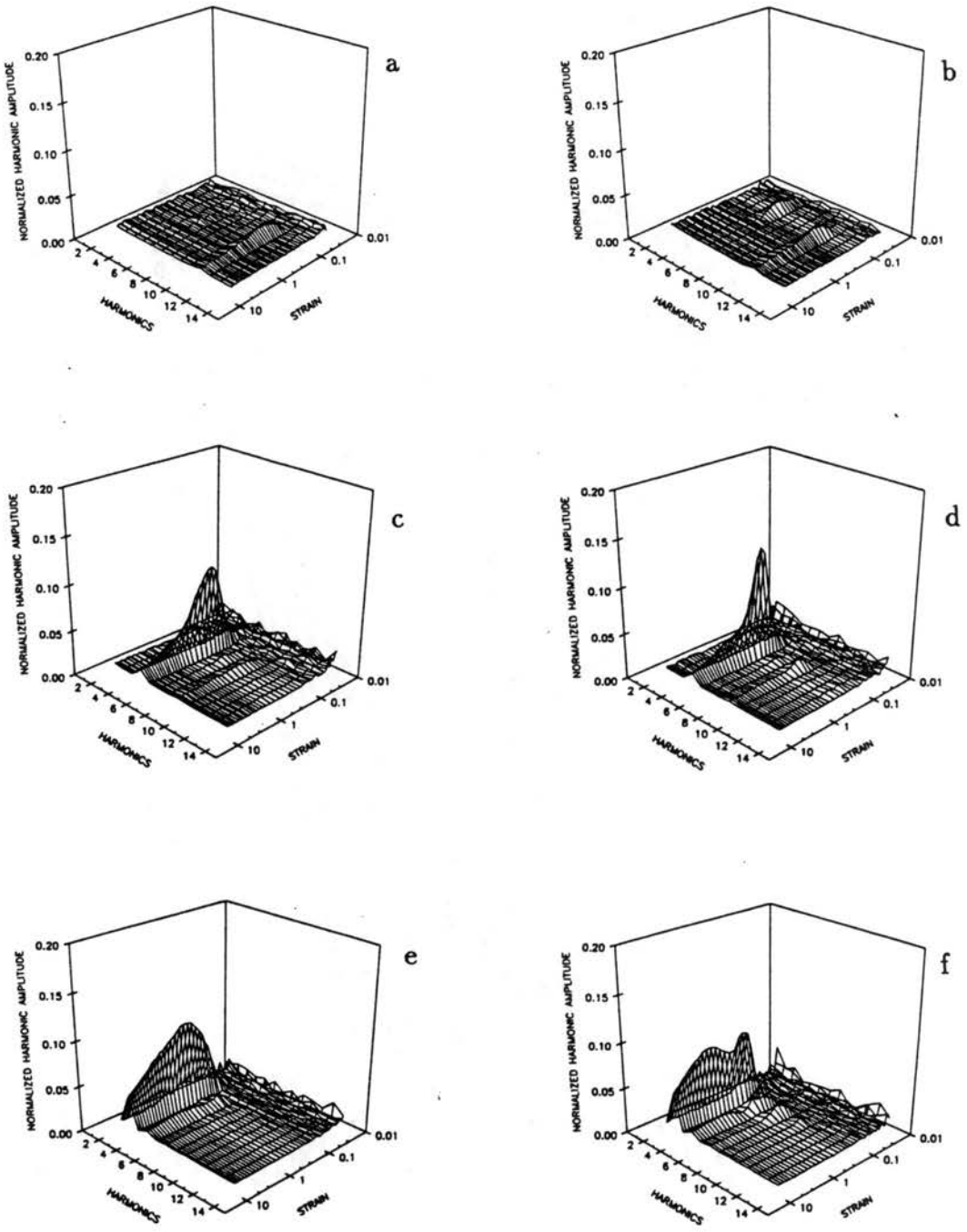

Figure 36. The harmonic content of the strain response as a function of frequency for the $\phi^* = 1.218$ sample. (a,b), (c,d), (e,f), (g,h), (i,j), and (k,l) represent 5, 2, 1, 0.1, 0.01, 0.001 Hz, respectively. a,c,e,g,i, and k represent presheared states and b,d,f,h,j, and l fcc states.

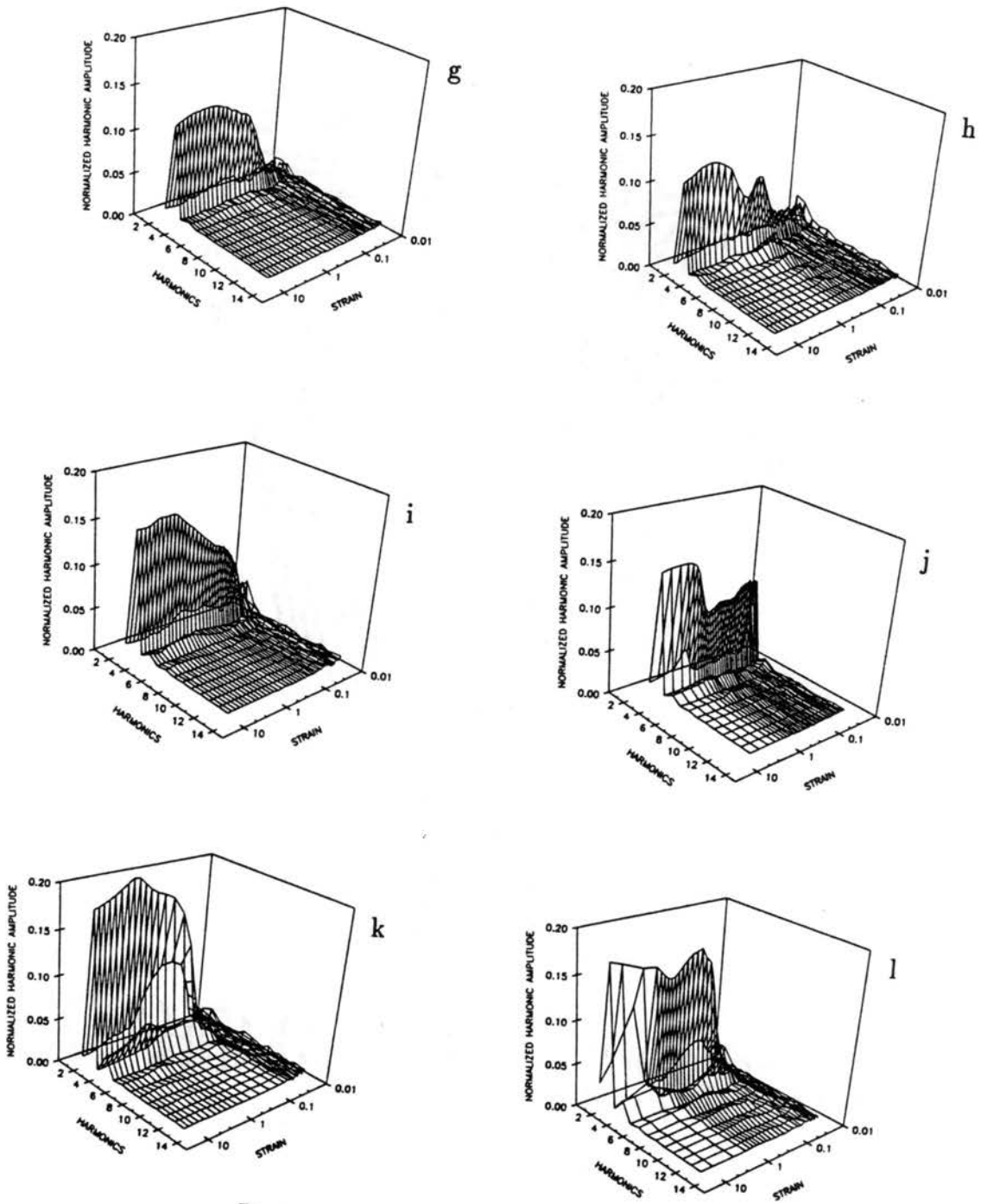

Figure 37. Continuation of Fig. 36.

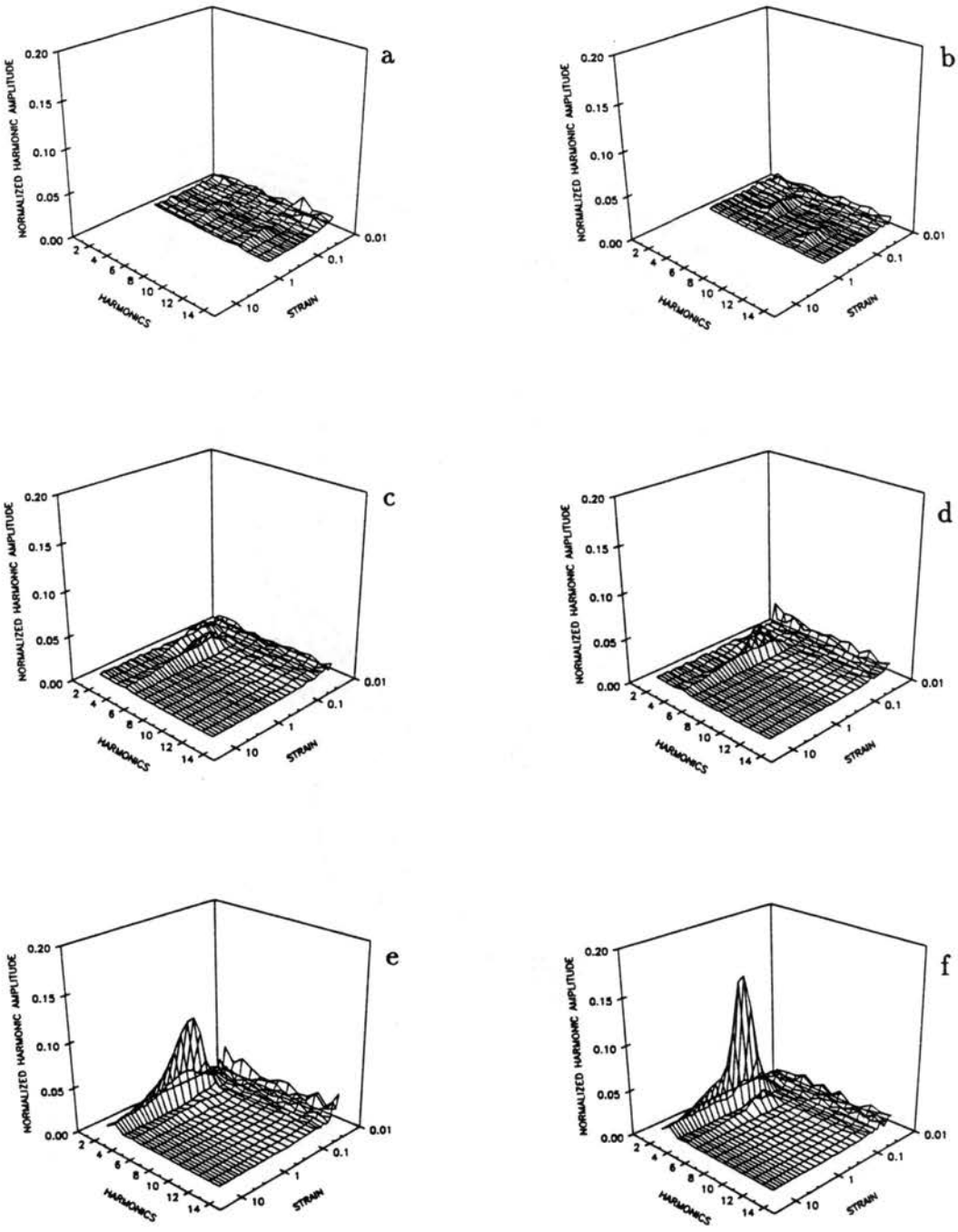

Figure 38. The harmonic content of the strain response as a function of frequency for the $\phi^* = 1.03$ sample. (a,b), (c,d), (e,f), (g,h), (i,j), and (k,l) represent 5, 2, 1, 0.1, 0.01, 0.001 Hz, respectively. a,c,e,g,i, and k represent presheared states and b,d,f,h,j, and l fcc states.

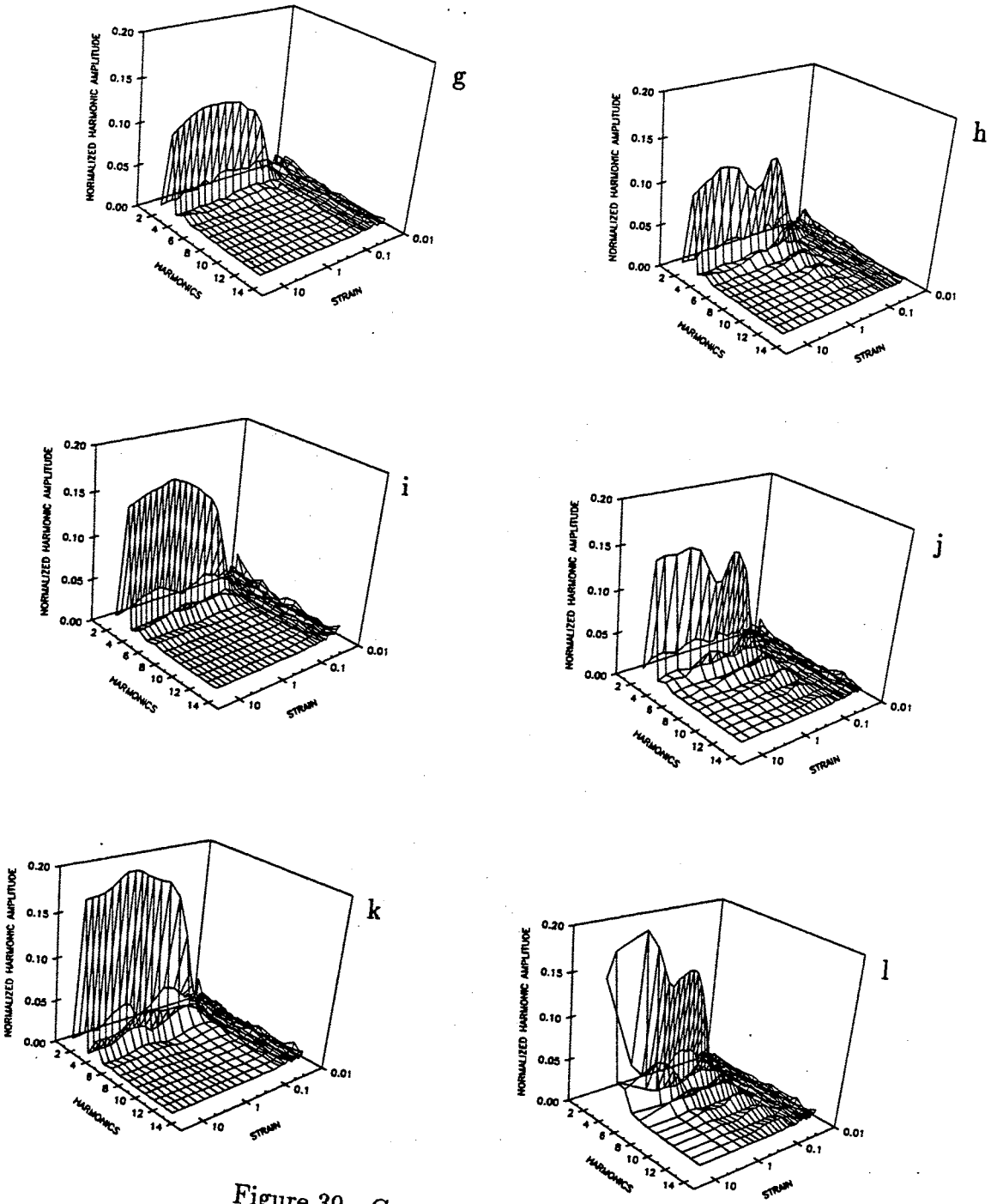

Figure 39. Continuation of Fig. 38.

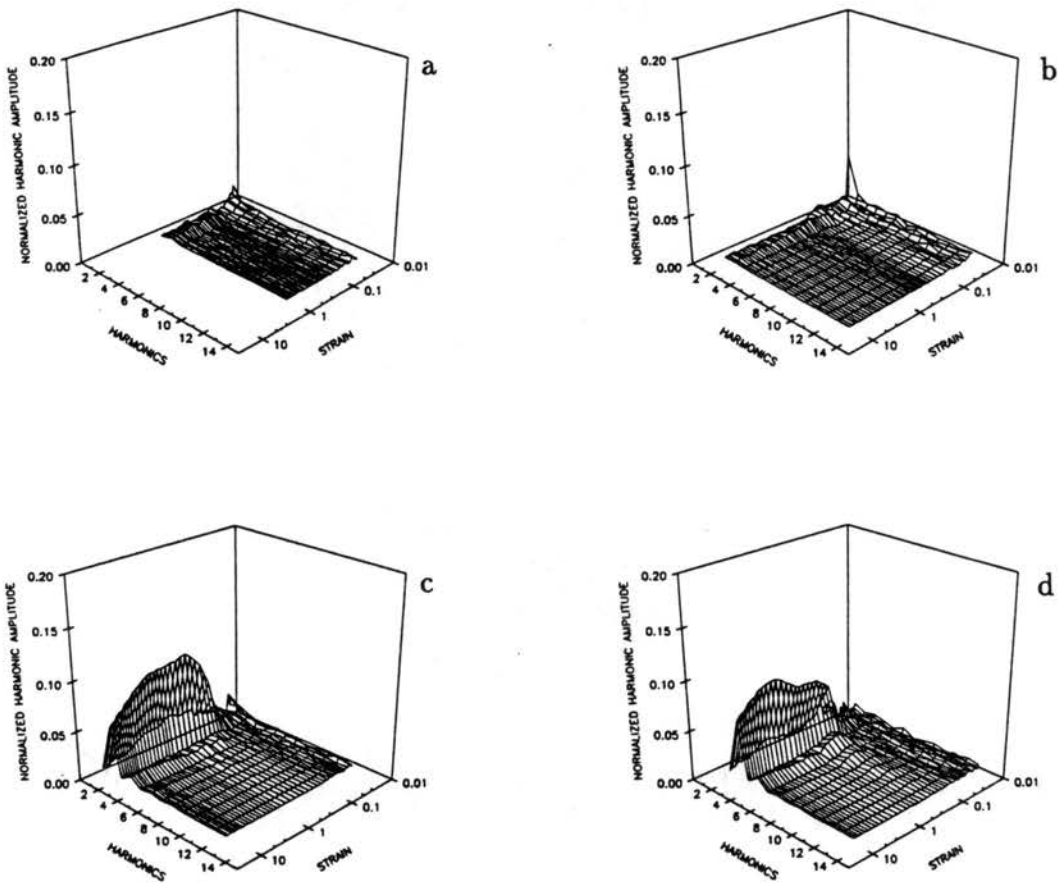

Figure 40. The harmonic content of the strain response as a function of frequency for the $\phi^* = 0.783$ sample. (a,b), (c,d), (e,f), and (g,h) represent 1, 0.1, 0.01, 0.001 Hz, respectively. a,c,e, and g represent presheared states and b,d,f, and h fcc states.

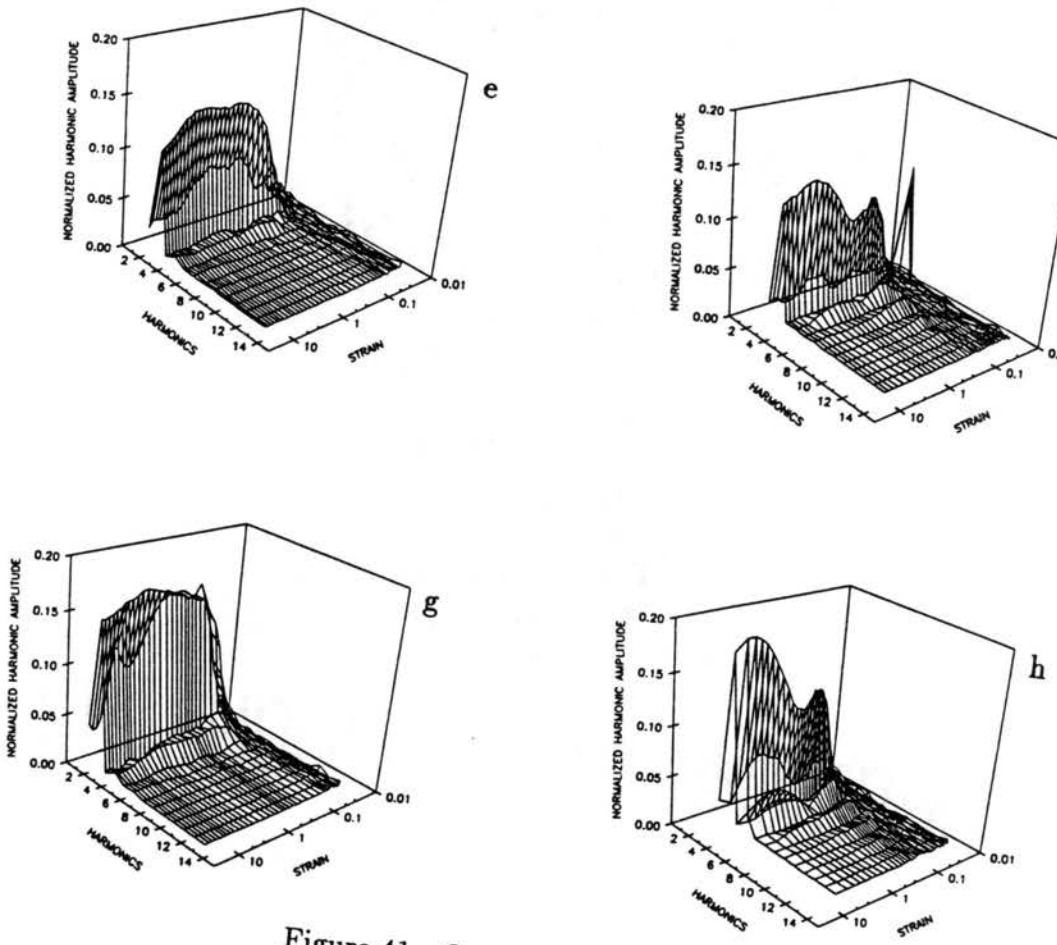

Figure 41. Continuation of Fig. 40.

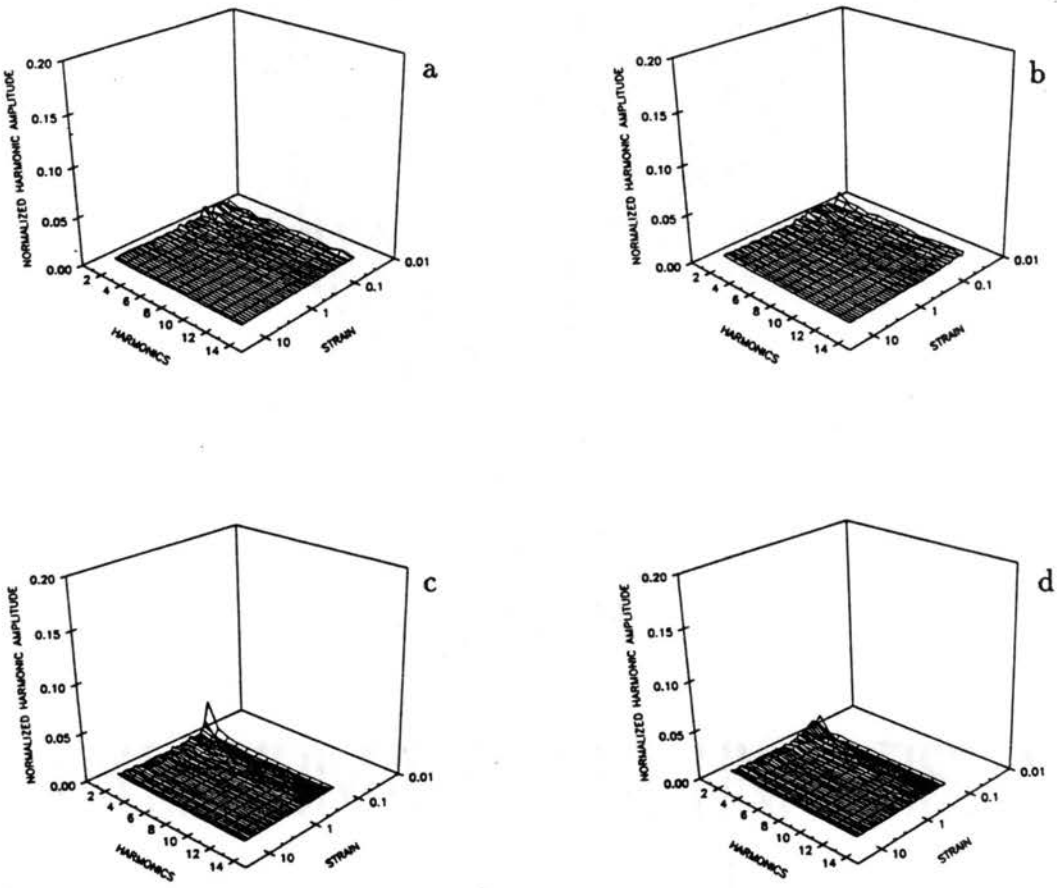

Figure 42. The harmonic content of the strain response as a function of frequency for the $\phi^* = 0.681$ sample. (a,b), (c,d), (e,f), and (g,h) represent 1, 0.5, 0.1, 0.01 Hz, respectively. a,c,e, and g represent presheared states and b,d,f, and h fcc states.

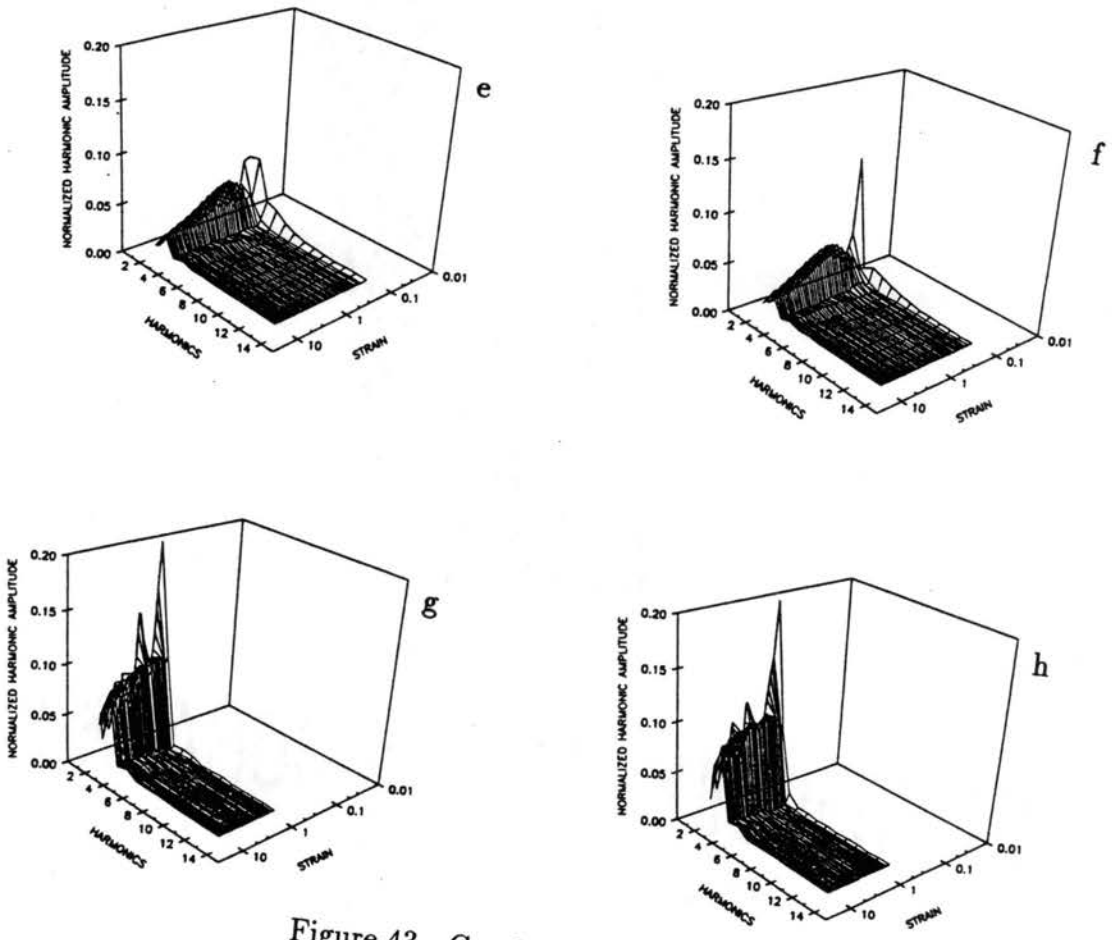

Figure 43. Continuation of Fig. 42.

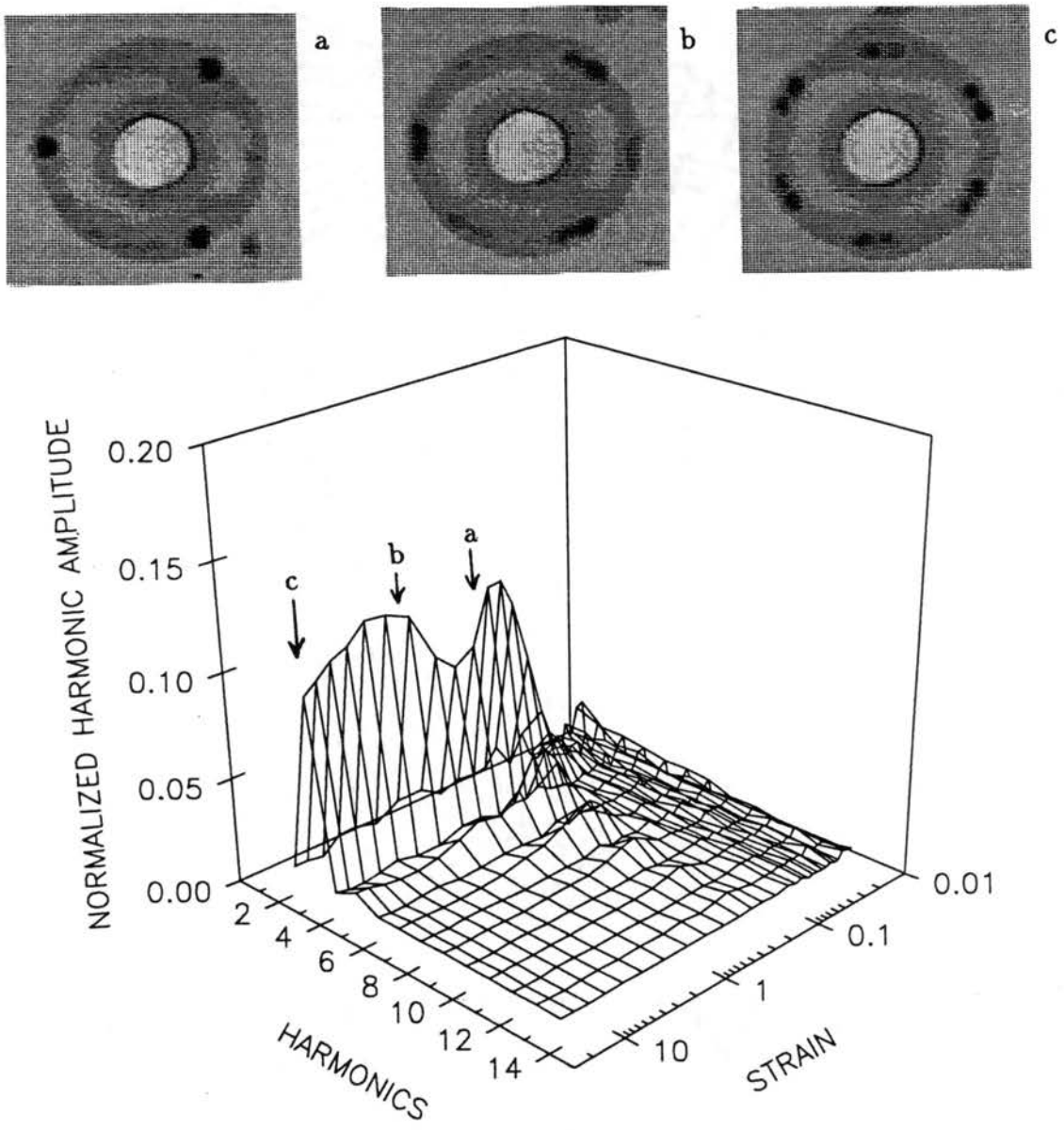

Figure 44. The harmonic content of the strain response for an fcc structure as a function of strain. Here, $\phi^* = 1.03$ at 0.1 Hz. The images a, b and c correspond to $\gamma = 0.19$, 2.3 and 10, respectively.

CHAPTER VII

CONCLUSION

The foundation of any complete study on the rheology of colloidal suspensions requires that the suspension is characterized at the particle level. Knowledge of particle shape, composition and interparticle interaction all aid in determining the macroscopic properties measured when applying a stress. Some of this information is known or at least suggested from the chemistry involved in manufacturing the particles. Dilute limit equilibrium phase behavior, electrophoretic measurements, dynamic and static light scattering and neutron scattering can help complete the picture. For sterically stabilized suspensions of spheres, this information is usually interpreted in terms of very simple models. i.e. hard spheres with Stokes drag. Charge stabilized suspensions are similarly interpreted, except here, the rigid particle core is surrounded by counterions. The key element in these interpretations is the rigidity of the particle. Independent of how the interparticle interactions affect the suspension behavior (equilibrium or nonequilibrium), there is a common invariant - the volume fraction. For spherical particles, one knows there is no packing fraction which can be greater than 74%. This provides an upper limit to the concentration for which a suspension is likely to flow under applied shear, and a minimum in interparticle separation. This also implies invariability of the particle form factor. Even though the particle may not be optically homogeneous when near index matching, a fit to the scattered intensity data in the dilute limit should apply at higher concentrations, allowing the structure factor to be extracted from scattered intensity data with a reasonable degree of confidence. Thus, the effect of shear may directly be examined through the structure factor. For the microgels examined in this study, the volume fraction is ill defined relative to a maximum packing fraction. The particles are swollen sufficiently that

they must compress at higher concentrations, not only raising questions as to the nature of the interparticle interactions, but also the particle form factor. Does the scattering result mostly from a central undisturbed core, or does the shape of the form factor change with concentration? How much does the particle distort under shear? The interaction potential between particles presumably results from a distortion of the particle. The amount of that distortion before the particles can approach no closer, relative to the overall particle size, determines the error in defining a rigid core. Presently, the best one may characterize the microgels is by comparing their equilibrium and nonequilibrium phase behavior to some reference system (hard spheres in this case). Future work in determining PMMA microgel particle structure is certainly warranted. Previous core shell models used to estimate microgel structure have met with some success in predicting scattering results [92]. Correlating the meaning of effective volume fraction with such structure can only serve to strengthen and perhaps quantify arguments concerning shear thinning, elasticity and microstructure, with Brownian, hydrodynamic and nonhydrodynamic interparticle interactions.

The intent of this study has been to correlate suspension microstructure with gross, macroscopic rheological measurements. In this sense, the emphasis may be placed less on the question as to why the microstructure evolves, and more on how this evolution affects the observed rheology. Such a course restricts one to volume fractions greater than 50% (below which induced microstructure is not observed). Due to experimental difficulties with inertia of the measuring system, which manifests itself as a DC drift in the oscillatory measurements, a decision to work at high effective volume fractions was made. Here, the effects of measuring system inertia are decreased due to increased viscous forces. A consequence of this is that the samples were concentrated enough ($\phi^* \geq 0.681$) that once microstructure had been induced, it was no longer possible to bring the suspension back to an amorphous state. Stable structures in which the closest packed direction in an hcp plane was oriented either in the velocity or vorticity direction could be induced. This result makes it natural to perform the series of measurements detailed in Chapter V and

VI, in which the evolution of each structure is examined from zero strain to strains approaching 1000%. The correlation between specific microstructural states with stress and strain has been demonstrated in the creep measurements. Where the system becomes frustrated, indicated by an increased instantaneous viscosity, the structure is seen to be evolving into a state which jams layers of particles into one another. In dynamic measurements, the linear moduli are observed to indicate a small dependence on microstructure. The storage modulus for the random stacked structure oriented with the closest packed along vorticity axis (fcc of Chapter VI) is found to be $\sim 15\%$ larger than for the random stacked structure with the closest packed structure oriented along the velocity direction (presheared structure). This behavior is observed over a frequency range of 1 Hz to 0.001 Hz, with little variation in G'. A microstructural correlation in the nonlinear region is clearly exhibited in the harmonic content of the strain response, where the moduli (linear quantities by definition) show a poor correlation. Taken as a whole, the steady shear and dynamic measurements appear to offer many connections, many of which are yet to be found. An aid in making some of these connections may be in found future experiments. There are several either incomplete or new measurements which may prove interesting for the microgel suspensions.

Similar to the measurements used to generate the nonequilibrium phase diagram of Chapter IV, a series of dynamic stress relaxation runs were made over all but the most concentrated samples examined. Here, the sample was initialized in a presheared state. An oscillatory stress was applied at a fixed frequency and strain. The dynamic stress was then observed and correlated with the microstructure. The results shown in Fig. 45 are shown for only the $\phi^* = 0.681$ sample and may or not be typical of other samples. Here, the dynamic stress is shown as a function of time, along with the corresponding microstructure. The trend indicates the relaxation of stress as the microstructure evolves either into a more defined ($\bigcirc$) presheared or ($\bullet$, $\bigtriangledown$) presheared/fcc structure. Difficulty in obtaining consistant results due to drift (presumably manifested as the oscillations shown), prevented a complete set of data from being taken. For the data shown, no higher order

harmonics were present in the response signal, thus σ^* is thought to be a valid quantity. The strains were in the nonlinear region.

Where as the above measurements are at strains which probe the gross evolution of one microstructural state into another, one could induce either a presheared or fcc structure and perform the same measurement as outlined above, only at small strains. Here, at a constant frequency, the strain could be maintained in the linear region and the moduli observed as a function of time. Although gross microstructural changes would not be expected, careful scattering measurements could be made on the structure in which the spot size and intensity is measured. This would essentially provide information about the dynamic stress as a function of 'working' the induced structure. Such a measurement would be the linear analog to that described in the previous paragraph. It would be curious to observe to what extent a 'linear' measurement would alter the microstructure. Perhaps the sample would anneal out defects, causing a sharpening of the Bragg spots?

The observation of a dip in the harmonic content for fcc microstructural states is indicating a softening of the system from nonlinearity. Since this dip appears to occur at about where the maximum amount of twinning may occur without distorting from an fcc to a mixed state, it would be of value to probe that region of strain as a function of time. What would happen to the harmonic amplitude if the system was held at the dip over a longer period of time?

In the context of steady shear measurements, stress relaxation would be of interest as a complement to the observations made in creep and creep recovery. Here, the time required for elastic relaxation may be independently checked with such measurements.

Overall, much effort was extended to making the rheological measurements reported in this study. Since the scattering images observed for the microgels qualitatively appear to be the same as those observed in hard sphere like PMMA suspensions, much of the time it was assumed the microstructure was behaving according to the geometrical model developed for those results [46]. In this regard,

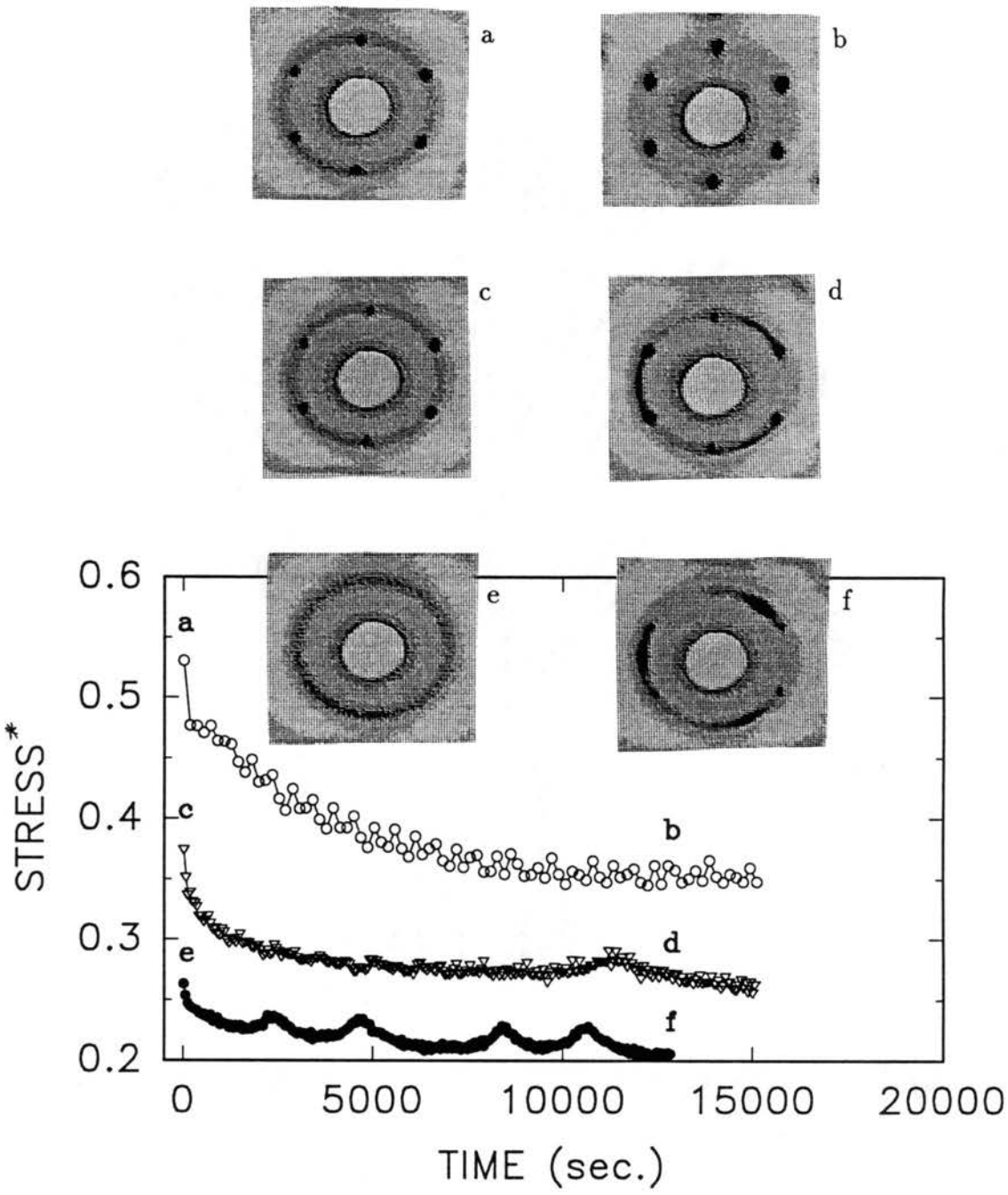

Figure 45. The dynamic stress versus time for $\phi^* = 0.681$. ○ $\omega = 0.4$ Hz strain $= 0.6$, ● $\omega = 0.4$ Hz strain $= 0.2$, ▽ $\omega = 0.8$ Hz strain $= 0.2$. The corresponding images a,c, and e are for $t \sim 0$ and b,d, and f $t \sim 13000$ sec.

more careful intensity measurements of the Bragg spots under applied shear and along different k vectors may prove enlightening.

BIBLIOGRAPHY

1. S. E. Paulin, Bruce J. Ackerson, and M. S. Wolfe, in *Complex Fluids,* M.R.S. Proceedings **248,** 259 (1991).

2. V. E. Shashoua and R. G. Beaman, J. Polymer Sci. **33,** 101 (1958).

3. L. H. Cragg and J. A. Manson, J. Polymer Sci. **9,** 265 (1952).

4. R. A Hayes, J. Polymer Sci. **13,** 583 (1954).

5. C. L. Sieglaff, polymer **4,** 281 (1963).

6. M. S. Wolfe and C. Scopazzi, J. Colloid Int. Sci. **133,** 265 (1989).

7. Private communication with M.S. Wolfe.

8. Bruce J. Berne and R. Pecora, *Dynamic Light Scattering* (Wiley, New York, 1976.)

9. A. Guinier, *X-Ray Diffraction in Crystals, Imperfect Crystals and Amorphous Bodies* (W.H. Freeman, San Francisco, 1963.)

10. P. N. Pusey and R. J. A. Tough, *Dynamic Light Scattering* edited by R. Pecora (Plenum, New York, 1985).

11. B. Chu, *Laser Light Scattering* (Academic Press, New York, 1974).

12. D. Kunz and W. Burchard, Colloid and Polymer Sci. **264,** 498 (1986).

13. J. V. Sanders, Nature **204,** 1151 (1964).

14. R. C. Williams and K. M. Smith, Nature **179,** 119 (1957).

15. K. M. Smith and R. C. Williams, Endeavour **17,** 12 (1958).

16. Seradyn Inc., Particle Technology Division, *Uniform Latex Particles* (Seragen Diagnostics Inc., Indianapolis, (1984).

17. P. N. Pusey, in *Liquids, Freezing and the Glass Transition,* edited by D. Levesque, J. P. Hansen, and J. Zinn-Justin (Elsevier, Amsterdam, 1990).

18. W. Luck, M. Klier, and H. Wesslau, Naturwiss **50,** 485 (1963).

19. T. Alfrey, E. B. Bradford, J. W. Vanderhoff, and G. Oster, J. Opt. Soc. Am. **44,** 603 (1954).

20. P. N. Pusey and W. van Megen, Nature (London) **320,** 340 (1986).

21. S. E. Paulin and Bruce J. Ackerson, Phys. Rev. Lett. **64,** 2663 (1990).

22. C. G. deKruif, J. W. Jansen, and A. Vrij, *Physics of Complex and Supermolecular Fluids,* edited by S. A. Safran and N. A. Clark (Wiley-Interscience, New York, 1987).

23. Akira Kose and Sei Hachisu, J. Colloid Int. Sci. **46,** 460 (1974).

24. W. B. Russel, *Phase Transitions in Colloidal Suspensions,* edited by Bruce J. Ackerson [Phase Transitions **21**, 127 (1990)].

25. B. J. Alder and T. E. Wainwright, J. Chem. Phys. **27,** 1208 (1957).

26. W. G. Hoover and F. H. Ree, J. Chem. Phys. **49,** 3609 (1968).

27. S. Hachisu and Y. Kobayashi, J. Colloid Interface Sci. **46,** 470 (1974).

28. R. D. Mountain and A. C. Brown, J. Chem. Phys. **80,** 2730 (1984).

29. J. P. Hansen, Phys. Rev. A **2,** 221 (1970).

30. W. G. Hoover, M. Ross, K. W. Johnson, D. Henderson, J. A. Barker, and B. C. Brown, J. Chem. Phys. **52,** 4931 (1970).

31. W. G. Hoover, S. G. Gray, and K. W. Johnson, J. Chem. Phys. **55,** 1128 (1971).

32. J. P. Hansen and D. Schiff, Mol. Phys. **25,** 1281 (1973).

33. J. L. Barrat, J. P. Hansen, G. Pastore, and E. M. Waisman, J. Chem. Phys. **86,** 6360 (1987).

34. B. B. Laird and D. M. Kroll, Phys. Rev. A **42,** 4810 (1990).

35. J. S. Rowlinson, Mol. Phys. **8,** 107 (1964).

36. J. A. Barker and D. Henderson, J. Chem. Phys. **47,** 4714 (1967).

37. H. C. Anderson, J. D. Weeks, and D. Chandler, Phys. Rev. A **4,** 1597 (1971).

38. M. S. Wolfe, 17^{th} Int. Conf. Org. Coat. Sci. Technol. Proceedings **17,** 369 (1991).

39. C. Smits, PhD thesis, Rijksuniversiteit Utrecht, 1991.

40. D. J. W. Aastuen, N. A. Clark, L. K. Cotter, and Bruce J. Ackerson, Phys. Rev. Lett. bf 57, 1733 (1986).

41. D. J. W. Aastuen, N. A. Clark, J. C. Swindal, and C. D. Muzny, *Phase Transitions in Colloidal Suspensions,* edited by Bruce J. Ackerson [Phase Transitions **21**, 127 (1990)].

42. K. Schatzel and Bruce J. Ackerson, Phys. Rev. Lett. **68,** 337 (1992).

43. P. N. Pusey, W. van Megen, P. Bartlett, Bruce J. Ackerson, J. G. Rarity, and S. M. Underwood, Phys. Rev. Lett. **63,** 2753 (1989).

44. C. Kittel, *Introduction to Solid State Physics,* 6^{th} Ed. (Wiley, New York, 1986).

45. Private communication with Bruce J. Ackerson

46. Bruce J. Ackerson, J. Rheol. **34,** 553 (1990).

47. J. L. Barrat and J. P. Hansen, J. Physique **47,** 1547 (1986).

48. D. J. Evans, H. J. M. Hanley, and S. Hess, Physics Today **37,** No. (1), 26 (1984).

49. Theo G.M. van de Ven, *Colloidal Hydrodynamics* (Academic Press, New York, 1989).

50. G. K. Batchelor, J. Fluid Mech. **41,** 571 (1970).

51. G. K. Batchelor and J. T. Green, J. Fluid Mech. **56,** 375 (1972).

52. G. K. Batchelor and J. T. Green, J. Fluid Mech. **56,** 401 (1972).

53. G. K. Batchelor, J. Fluid Mech. **74,** 1 (1976).

54. G. K. Batchelor, J. Fluid Mech. **83,** 97 (1977).

55. B. U. Felderhof, Physica A **118,** 69 (1983).

56. B. U. Felderhof, Physica A **147,** 203 (1987).

57. B. U. Felderhof and R. B. Jones, Physica A **146,** 417 (1987).

58. W. B. Russel, J. Chem. Soc., Faraday Trans. **80,** 31 (1984).

59. W. B. Russel and A. P. Gast, J. Chem. Phys. **84,** 1815 (1986).

60. N. J. Wagner and W. B. Russel, Physica A **155,** 475 (1989).

61. Bruce J. Ackerson and N. A. Clark, Physica A **118,** 221 (1983).

62. David Ronis, Phys. Rev. Lett. **52,** 473 (1984).

63. David Ronis, Phys. Rev. A **29,** 1453 (1984).

64. Bruce. J. Ackerson and N. A. Clark, Phys. Rev. A **30,** 906 (1984).

65. Bruce. J. Ackerson, J. B. Hayter, N. A. Clark, and L. Cotter, J. Chem. Phys. **84,** 2344 (1986).

66. David Ronis, Phys. Rev. A **34,** 1472 (1986).

67. N . J. Wagner, G. G. Fuller, W. B. Russel, J. Chem. Phys. **89,** 1580 (1988).

68. Bruce J. Ackerson, C. G. De Kruif, N. J. Wagner, and W. B. Russel, J. Chem. Phys. **90,** 3250 (1989).

69. Bruce J. Ackerson, Physica A **174,** 15 (1991).

70. N. J. Wagner, and Bruce J. Ackerson, J. Chem. Phys. **97,** 1473 (1992).

71. A. T. J. M. Woutersen PhD thesis, Rijksuniversiteit Utrecht, 1993.

72. P. M. Chaikin, J. M. di Meglio, W. D. Dozier, H. M. Lindsay, and D. A. Weitz, *Physics of Complex and Supermolecular Fluids,* edited by S. A. Safran and N. A. Clark (Wiley-Interscience, New York, 1987).

73. R. L. Hoffman, Trans. Soc. Rheol. **16,** 155 (1972).

74. R. L. Hoffman, J. Colloid Interface Sci. **46,** 491 (1974).

75. M. Tomita and T. G. M. Van De Ven, J. Colloid Interface Sci. **99,** 374 (1984).

76. Bruce J. Ackerson and P. N. Pusey, Phys. Rev. Lett. **61,** 1033 (1988).

77. J. C. Van Der Werff, Bruce J. Ackerson, R. P. May, and C. G. De Kruif, Physica A **165,** 375 (1990).

78. L. B. Chen, PhD thesis, University of Illinois, Urbana, 1991.

79. J. F. Brady and Georges Bossis, Ann. Rev. Fluid Mech. **20,** 111 (1988).

80. R. Buscall, J. W. Goodwin, M. W. Hawkins, and R. Ottewill, J. Chem. Soc., Faraday Trans. I **78,** 2873 (1982).

81. W. B. Russel, *Future Directions in Polymer Colloids,* edited by M.S. El-Aasser and R.M. Fitch (Martinus Nijhoff, Netherlands, 1987).

82. W. J. Frith, PhD thesis, Katholieke Universiteit Leuven, 1986.

83. I. M. Krieger and M. Eguiluz, Trans. Soc. Rheol. **20** 29 (1976).

84. M. Reiner, Physics Today **17** 62 (1964).

85. R. M. Christensen, *Theory of Viscoelasticity, An Introduction* (Academic Press, New York, 1982.)

86. G. C. Berry, B. L. Hagar and C.-P. Wong, Macromolecules **10** 361 (1977).

87. K. Walters, *Rheometry* (Chapman and Hall, London, 1975.)

88. G. Bohme, *Non-Newtonian Fluid Mechanics* (Elsevier, New York, 1987.)

89. R. B. Bird, R. C. Armstrong and O. Hassager, *Dynamics of Polymeric Liquids, Vol. 1* (Wiley and Sons, New York, 1987).

90. I. F. MacDonald, B. D. Marsh, and E. Ashare, Chem. Eng. Sci. **24,** 1615 (1969).

91. W. Philippoff, Trans. Soc. Rheol. **10,** 317 (1966).

92. B. E. Rodriguez, M. S. Wolfe and M. Fryd, Macromolecules, submitted

APPENDICES

APPENDIX A

RANDOM STACKING OF HCP PLANES

Unlike the randomly dispersed particles of a liquid, a crystalline structure has long ranged order associated with it. This unique property requires that the lattice associated with the crystal is invariant under translation [44]. That is, one can move to any lattice point in the crystal by a translation, $\vec{T}$

$$\vec{T} = u_1\vec{a}_1 + u_2\vec{a}_2 \tag{39}$$

where $\vec{a}_1$ and $\vec{a}_2$ are fundamental translation vectors and u_1 and u_2 arbitrary integers. As a consequence of this, any local, periodic property of the crystal, $n(\vec{r})$, must also be invariant under translation

$$n(\vec{r} + \vec{T}) = n(\vec{r}) \tag{40}$$

This periodicity can be used to Fourier expand $n(\vec{r})$ as

$$n(\vec{r}) = \sum_{\vec{G}} C_{\vec{g}} \exp^{i\vec{G}\cdot\vec{r}} \tag{41}$$

resulting in a connection between the real space lattice and its dual in Fourier space. The lattice in Fourier space is known as the reciprical lattice, where $\vec{G}$ is a reciprical lattice translation vector, analogous to $\vec{T}$. Here, translantional invariance requires

$$\vec{G}\cdot\vec{T} = 2\pi \times \text{integer} \tag{42}$$

where

$$\vec{G} = v_1\vec{b}_1 + v_2\vec{b}_2 \tag{43}$$

with v_1, v_2, and m integers and $\vec{b}_1$ and $\vec{b}_2$ are the reciprical translation vectors. They may be constructed as [44]

$$\begin{aligned} \vec{b}_1 &= 2\pi \frac{\vec{a}_2 \times \vec{a}_3}{\vec{a}_1 \cdot (\vec{a}_2 \times \vec{a}_3)} \\ \vec{b}_2 &= 2\pi \frac{\vec{a}_3 \times \vec{a}_1}{\vec{a}_1 \cdot (\vec{a}_2 \times \vec{a}_3)} \\ \vec{b}_3 &= 2\pi \frac{\vec{a}_1 \times \vec{a}_2}{\vec{a}_1 \cdot (\vec{a}_2 \times \vec{a}_3)} \end{aligned} \tag{44}$$

The diffraction pattern of a crystal is given by the reciprocal lattice, which may be constructed from the reciprocal translation vectors. The condition for diffraction to occur such that the crystal structure in real space is mapped by the reciprocal lattice in a light scattering measurement is given by Laue: *constuctive interference between scatterers will occur, only if the scattering wave vector is a vector of the reciprical lattice*, $\vec{k} = \vec{G} = \vec{k}_s - \vec{k}_i$. This is nicely illustrated by the Ewald Construction shown in Fig. 46. Here, in reciprical space, a sphere of radius k_i is drawn about $\vec{k}_i$. The condition for a diffraction peak occurs only if the reciprocal lattice vector $\vec{G}$ connects two reciprocal lattice points on the surface of this sphere. A more formal way of stating the Laue condition is

$$\vec{T} \cdot \vec{G} = \vec{T} \cdot \vec{k} = 2\pi \times \text{integer} \tag{45}$$

from which it can be seen that a one, two, and three dimensional lattice in real space results in planes, tubes and points, respectively, in reciprical space. To compare the measured results of the powder pattern scattering with that of randomly stacked layers of hexagonal close packed planes, the reciprocal space structure must be calculated and suitably averaged over all crystallite orientations.

First consider a single hcp layer as shown in Fig. 47a, with fundamental translation vectors, scaled on nearest neighbor distance

$$\begin{aligned} \vec{r}_a &= \hat{x} \\ \vec{r}_b &= \tfrac{1}{2}\hat{x} + \tfrac{\sqrt{3}}{2}\hat{y} \end{aligned} \tag{46}$$

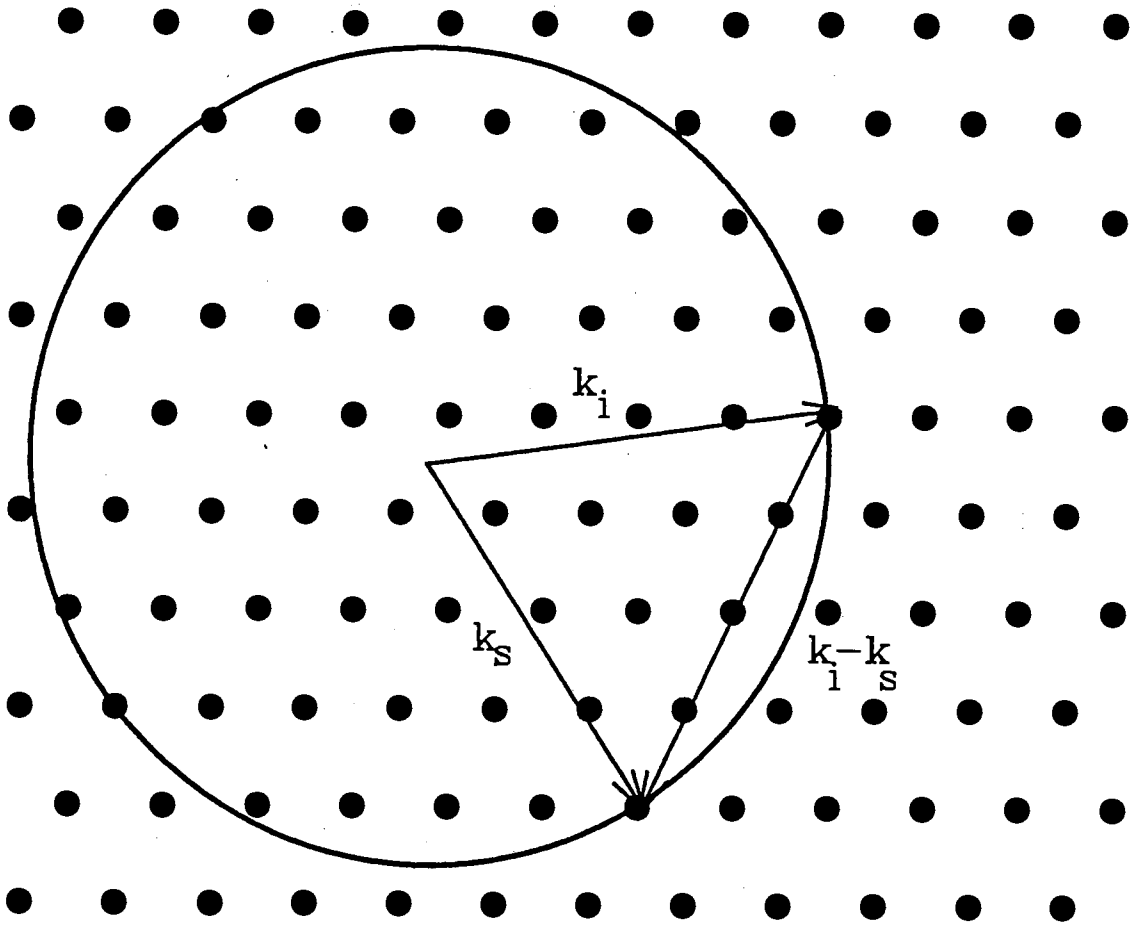

Figure 46. Ewald construction for diffraction. $\vec{k}_i$, $\vec{k}_s$, and $\vec{k} = \vec{k}_i - \vec{k}_s$ are the incident, scattered, and scattering wave vectors, respectively. A diffraction maximum will occur only if $\vec{G} = \vec{k}$ connects two reciprocal lattice points on the surface of a sphere of radius $|\vec{k}_i|$, drawn about $\vec{k}_i$.

The reciprocal space structure associated with this plane is shown in Fig. 47b, where the points of real space are now lines in reciprocal space. Depending on the size and/or disorder of the hcp plane, the lines will be broadened into tubes. In a scattering measurement, the intensity distribution of these tubes as a function of k, is obtained from the geometrical form factor, $F(\vec{k})$, of the plane

$$F(\vec{k}) = P(\vec{k}) \sum_{j=1}^{N} \exp(i\vec{k} \cdot \vec{r}_j) \tag{47}$$

where P is the particle form factor, N the number of spheres in the plane, and $\vec{r}_j$ representing the position of the j^{th} sphere in the plane, referenced to an arbitrary origin

$$\vec{r}_j = m\vec{r}_a + n\vec{r}_b. \tag{48}$$

where m and n are integers. The layer form factor results from summing the scattered radiation from each of the spheres, along with their phase shift. The intensity may be obtained as the modulus squared of the form factor $|F(\vec{k})|^2$.

Stacking of the hcp planes results in a further modulation of the tubes along the z axis. This modulation may be accounted for in the intensity by a phase factor associated with the scattering between hcp planes, as

$$I(\vec{k}) = \frac{N}{M} \sum_{l} |F(\vec{k})|^2 \langle \exp^{-i\vec{k}\cdot\vec{R}_l} \rangle \tag{49}$$

where N now represents the total number of particles and M the total number of layers (hcp planes). $\vec{R}_l$ represents the postition of the l^{th} layer. In calculating the sum over all configurations, it is useful to examine the stacking of hcp planes. Once the first layer is placed, there are two choices of placement for the next layer. If A denotes the initial layer, then B and C denote the possible choices of placement of the next layer. This results in the possible stacking sequences ABCABC..., and ACBACB..., or ABABA..., and ACACA..., corresponding to fcc or hcp crystal structures, respectively. Such stacking sequences can also be realized by the application of successive stacking along one of two vectors, $\vec{R}_1$ and $\vec{R}_2$

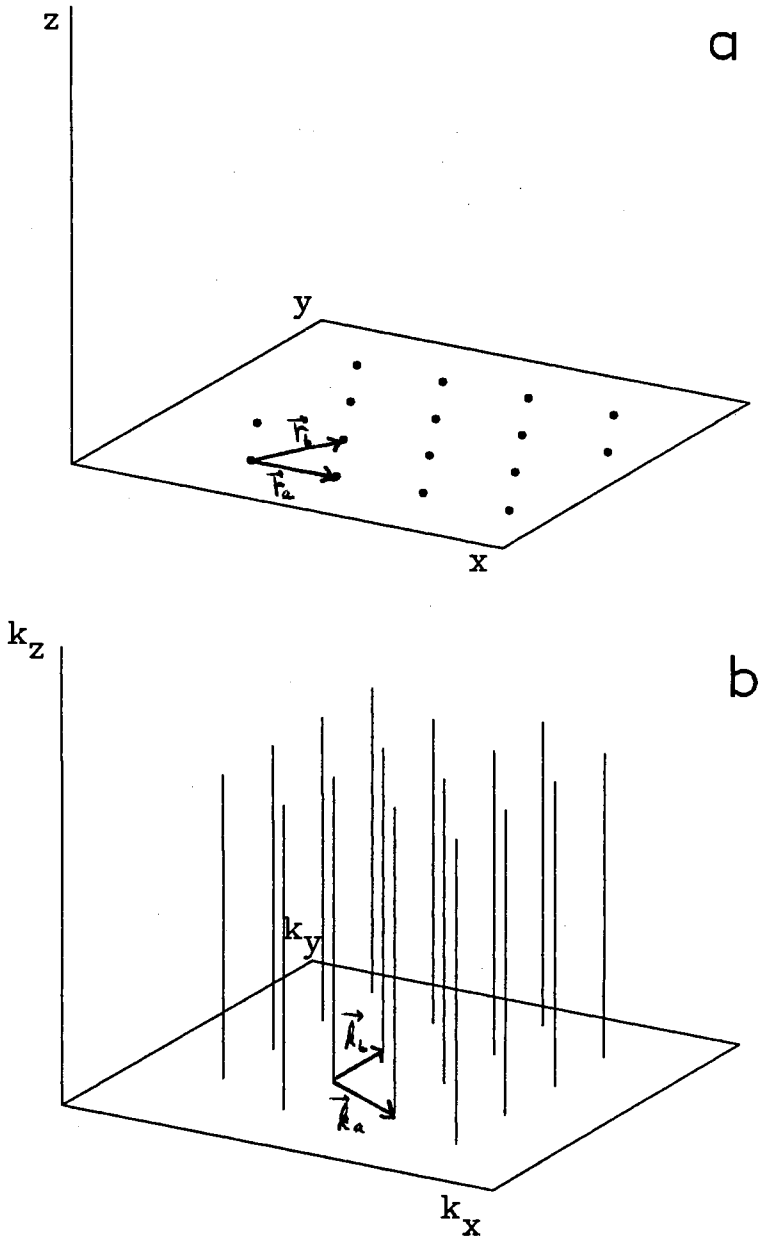

Figure 47. (a) Single hexagonal close packed plane with translation vectors $\vec{r}_a$ and $\vec{r}_b$, respectively. (b) Reciprocal space construction of the real space plane, depicting lines (tubes) perpendicular to that plane.

$$\begin{aligned} \vec{R}_1 &= \tfrac{1}{2}\hat{x} + \tfrac{1}{2\sqrt{3}}\hat{y} + \sqrt{\tfrac{2}{3}}\hat{z} \\ \vec{R}_2 &= \tfrac{1}{2}\hat{x} - \tfrac{1}{2\sqrt{3}}\hat{y} + \sqrt{\tfrac{2}{3}}\hat{z} \end{aligned} \tag{50}$$

Ackerson recognized this property and utilized a transfer matrix technique to generate the possible layer configurations Here, the propogation of a scattered wave vector from plane to plane is given by the successive multiplications of the transfer matrix

$$\bar{A} = \begin{pmatrix} \alpha \exp^{i\vec{k}\cdot\vec{R}_1} & (1-\alpha)\exp^{i\vec{k}\cdot\vec{R}_2} \\ (1-\alpha)\exp^{i\vec{k}\cdot\vec{R}_1} & \alpha \exp^{i\vec{k}\cdot\vec{R}_2} \end{pmatrix} \tag{51}$$

The parameter α determines the randomness of the layer stacking, with α ranging from 1 to 0 for fcc to hcp stacking, respectively. Thus, the scattered intensity may be written,

$$I(\vec{k}) = \frac{M}{N}|F(\vec{k})|^2 \left[\sum_{l=1}^{\infty}(\bar{A})^l + \bar{I} + \sum_{l=1}^{\infty}(\bar{A}^*)^l\right] \tag{52}$$

where * represents the complex conjugate and $\bar{I}$ the unit matrix. Under the assumptions of perfect stacking and convergence of the above summations, the scattered intensity from registered, stacked hcp planes is found to be

$$\begin{aligned} I(\vec{k}) = \frac{M}{N}|F(\vec{k})|^2\, \alpha(1-\alpha)[1-\cos\vec{k}\cdot(\vec{R}_1-\vec{R}_2)]/ \\ [1-2\alpha+3\alpha^2-2\alpha^2(\cos\vec{k}\cdot\vec{R}_1+\cos\vec{k}\cdot\vec{R}_2)+\alpha^2\cos\vec{k}\cdot(\vec{R}_1-\vec{R}_2)+ \\ (2\alpha-1)\cos\vec{k}\cdot(\vec{R}_1+\vec{R}_2)] \end{aligned} \tag{53}$$

The above can be used to find the modulation of intensity along the tubes in reciprocal space. However, in calculating the powder scattering from a sample of randomly oriented crystallites requires orientational averaging. This is achieved via a method devised by Guinier [9]. Assuming that all of the powder grains are identical, the powder scattering profile is obtained by rotating in all directions about the center of the reciprical lattice for a single crystal. Projections of the intersection of modulated tubes onto the Ewald sphere of radius k are then

integrated over the entire sphere, yielding the scattering intensity at that angle (defined by k). Repetion of this process over a range in k produces the powder pattern signature for random stacked hcp planes. This calculation is carried out by the program listed in Appendix II.

APPENDIX B

POWDER PATTERN PROGRAM

```
//  CALCULATE THE SCATTERING FROM A CRYSTALLITE COMPOSED OF
//  RANDOMLY STACKED HEXAGONAL CLOSE PACKED PLANES
//  A1=stacking probability (A1=1 is fcc, A1=0 is hcp, A1=0.5 is random)
//  Based on the original basic code of Bruce J. Ackerson (1989).
//  S.E. Paulin modified:
//   Temperature diffuse scattering added 12/91
//   Converted to C 5/92.
//   Revised tube correction factor 1/93.
//

#include <math.h>
#include <stdio.h>
#include <string.h>

FILE *indata,*outdata,*andata;

double  A8,A9,B1,R1,R2,R3,R4,R5,R6,K1,K2,K3,K4,K5,K9,L1,V1,V2,V3,V4,N9,D9;
double  Q9,Q4,Q5,S1,VIB,fac,abt,A1,L9,K,C1,A,B,K6,U6,U5,ZZ,dia,thet,net;
int     I1,I2,I3,J1,J2,pn,nps,scl;
char    *oufi;

main(int argc, char * argv[])
{

/*** FCC - HCP RANDOM STACKING POWDER PATTERN CALC  5-3-92  ***/

printf("%s ","Filename ");
scanf("%s",oufi);

   if((outdata = fopen(oufi,"w")) == NULL)  {
      fprintf(stderr,"ERROR*** cannot open %s\n",oufi);
      exit(1);
   }
```

```
printf("%s","A8 (100.0) and A9 (7.): ");
scanf("%lf%lf",&A8,&A9);
printf("%s","VIB (0.0) and fac (1.0): ");
scanf("%lf%lf",&VIB,&fac);
printf("%s","dia: ");
scanf("%lf",&dia);
printf("%s","start angle (degrees): ");
scanf("%lf",&L1);

pn  = 5;
abt = 12; /*** integrate out to 3 standard deviations ***/

fac=fac;

net = 1.0/sqrt(2.0*A9);  /*** net is the standard deviation ***/
net = net/4.0;

/*** BASIS VECTORS ***/
R1 = dia*(1.0 / 2.0);
R2 = dia*(1.0 / (2.0 * 1.732051));
R3 = dia*0.8164966;
R4 = dia*(1.0 / 2.0);
R5 = -R2;
R6 = R3;

/***  TUBE WAVE VECTOR POSITION  ***/
K1 = (2.0 * 3.1415)/dia;
K2 = (2.0 * 3.1415 / 1.732051)/dia;
K3 = (2.0 * K2);

/*** FCC STACKING PROBABILITY ***/
printf("%s","FCC stacking probability: ");
scanf("%lf",&A1);

/***   A1 = 0.5;  ***/

/***  HCP STACKING PROBABILITY ***/
B1 = (1.0 - A1);

/*** LAYER CONTINUATION PROB ***/
/*   DEPENDS ON K AND NOT KZ   */
/*** SWEEPING WAVEVECTORS    ***/
printf("%s","Number of points? ");
scanf("%d",&nps);
   for(I3 = 1;I3<nps+1;I3++)  {
```

```
      thet = 0.25;
      L9 = (6.2832*2.0*1.54/632.8)*sin(thet*3.1416/360.0);
      K = (6.2832*2.0*1.54/632.8)*sin((L1+(I3*thet))*3.1416/360.0);
      C1 = exp(-A8 * K * K);
      A  = C1 * A1;
      B  = C1 * B1;

/***  SCANNING PENETRATION ****/
     S1 = 0.0;
 for(I1 = -pn;I1<pn+1;I1++)  {

    for(I2 = -pn;I2<pn+1;I2++)  {
       Q4 = I1 * K1;
       Q5 = ((I1 * K2) + (I2 * K3));
       Q9 = sqrt(Q4*Q4+Q5*Q5);

  if(Q9 <= 0.0)  {
     Q9 = L9;
  }

  if(Q9 > K + (abt*net))  {
     continue;

  }

  /***  SCAN ABOUT THE TUBES ***/
  for(J1 = -abt;J1<abt+1;J1++)  {

     for(J2 = -abt;J2<abt+1;J2++)  {
K4 = Q4 +  ((double)(J1) * net);
K5 = Q5 +  ((double)(J2) * net);
K9 = sqrt(K4*K4+K5*K5);
   if(K9 > K)  {
      continue;

   }
  K6 = sqrt(K*K-K4*K4-K5*K5);

  /***  TUBE DIAMETER FACTOR ***/
  U6 = exp(-A9 * ((J1 * J1) + (J2 * J2))*net*net);

   /*** AREA PROJECTION CORRECTION ***/
   if(K6==0.0)  {
      continue;
   }
```

```
U5 = net*net;
U5 = U5*sqrt((K4*K4)/(K6*K6)+(K5*K5)/(K6*K6)+1.0);

/*** CALC TRIG FUNCTIONS  ***/
V1 = (K4 * R1) + (K5 * R2) + (K6 * R3);
V2 = (K4 * R4) + (K5 * R5) + (K6 * R6);
V3 = V1 - V2;
V4 = V1 + V2;

/*** CALC THE MODULATED INTENSITY ***/
N9 = (1.0-2.0*A*B+2.0*A*A*B*B-pow(A,4)-pow(B,4))
   + (B-A+B*A*A-A*B*B-pow(B,3)+pow(A,3))
   * (cos(V1)+cos(V2))-2.0*A*B*cos(V3);

D9 = (1.0+2.0*A*A-2.0*A*A*B*B+pow(A,4)
   + pow(B,4))+(-2.0*A+2.0*B*B*A-2.0*pow(A,3))
   * (cos(V1)+cos(V2))+2.0*A*A*cos(V3)
   + 2.0*(A*A-B*B)*cos(V4);

S1 = S1 + (2.0 * N9 * U5 * U6) / D9;

     }
  }
    }
 }

/*** TEMPERATURE CORRECTION ***/
ZZ = fac*(1.0-exp(-VIB*K*K/3.0)) + S1*exp(-VIB*K*K/3.0);

fprintf(outdata,"%f\t%e\t%e\n", K, S1, ZZ);
printf("%f\t%e\t%e\n",K,S1,ZZ);
// printf(".");

     }
fprintf(outdata,"%f\t%e\t%f\n", A8, A9, A1);
fprintf(outdata,"%f\t%e\n", VIB, fac);

close(outdata);

}
```

APPENDIX C

DRIVER FOR STEPPER MOTOR AND LANGLEY-FORD CORRELATOR

```
/*   LFI:  driver program for stepper motor goniometer and Langley-Ford
     correlator.

     S. E. Paulin  04-12-92   */


#include <ctype.h>
#include <math.h>
#include <stdio.h>
#include <conio.h>
#include <bios.h>
#include <dos.h>
#include <string.h>
#include <graphics.h>
#include <io.h>

FILE *fo,*par;
char *fiout;
double vplt[500];


/*              List of variables for main()

par      input file stream for parameters used by LFC
fo       file output stream
pff      path for output file (lfc.par variable)
fiout    name of output file
daf      name of output file with appended path and .int
cflag    flag set to value of GET_COR() upon too many
overflows or not enough counts
flag     flags program  to close if too many overflows
ovfl     maximum number of overflows (lfc.par variable)
minc     minimum number of counts (lfc.par variable)
slp      automatic cycle time (sec) for correlator
```

```
k       index for the number of steps completed from the
start angle to the final angle in increments of step
stsi    step size in degrees
prepos  the maximum number of steps required to achieve
the final angle
delay   timing variable for delay loop in STEP_MOT()
fang    final angle goniometer is moved to in degrees
stdeg   number of steps/degree required by the stepper
motor (25000/360)
step    number of steps required to go from the starting angle
to the final angle in steps of size stsi
stang   start angle in degrees
pang    present angle in degrees at start of program
cstep   correction for the starting angle to which the motor
is stepped due to floating-integer round off error.
i.e.  stepper motor must be stepped an integer
number if steps
vplt    global variable which holds the sine theta corrected
intensity used in PL_IT()
in      kbhit variable
gdriver variables used in initializing graphics driver
*/


int main(void)
{

int gdriver = DETECT, gmode, errorcode;
int gflag,ovfl,cflag,flag,slp,k,prepos,step,delay,fang,minc;
float stdeg,stsi,cstep,stang,pang;
register int in;
char daf[20],pff[20];

initgraph(&gdriver,&gmode,"");
errorcode = graphresult();

if(errorcode != grOk)
{
   printf("Problem here!  Closing and exiting...\n",grapherrormsg(errorcode)
   exit(1);

}

restorecrtmode();
```

```
cflag = -1;
stdeg = 69.4444;

if ((par = fopen("lfc.par","r")) == NULL)  {
   puts("ERROR*** cannot find parameter file 'lfc.par'\n");
   exit();
}

fscanf(par,"%d\n",&ovfl);
fscanf(par,"%d\n",&minc);
fscanf(par,"%s\n",pff);
fclose(par);

printf("Enter a filename\n ");
scanf("%s",fiout);
strcat(fiout,".int");
strcpy(daf,pff);
strcat(daf,fiout);

if (access(daf,0) == 0)  {
   puts("FILE EXISTS...  OVERWRITE?  y or n,  DO NOT TYPE A RETURN!");
   printf("%s\n"," ");

in = getch();
in = tolower(in);

if (in == '\x6E')  {
   exit();
}
}

if ((fo = fopen(daf,"w")) == NULL)  {
   puts("ERROR*** cannot open file\n");
   exit();
}

printf("Enter present angle in degrees\n ");
scanf("%f",&pang);

printf("start angle in degrees\n ");
scanf("%f",&stang);

printf("final angle in degrees\n ");
scanf("%d",&fang);
```

```
printf("step size in degrees\n ");
scanf("%f",&stsi);

/***   printf("Enter delay (500 is nice)\n ");
scanf("%d",&delay);   ***/

delay = 500;

printf("How long to sleep?\n ");
scanf("%d",&slp);

/*  step:  number of steps required to move from present angle to
    starting angle, truncated to integer value  */

step = (stang - pang)*stdeg;
printf("Please wait...\n");

STEP_MOT(step,delay);

/*  'if' needed for correct calculation for negative angle entries  */

if(step<0) step = step*(-1);

/*  cstep:  calculate correction for angle due to integer truncation
    for number of pulses sent to stepper motor  */

cstep = (abs(stang - pang) - (step/stdeg));

/*  prepos:  calculate the number of moves required to move from
    starting to final angle  */

prepos = abs(abs((fang-stang))/stsi);  /***  careful int,float decl..***/

/*  'if' needed for correct calculation for negative angle entries  */

if(stang<0)  {
   stsi=stsi*(-1);
   cstep = cstep*(-1);
}

/*  'if' decides which way to move rotor  */

if((fang-stang<0)) stsi=stsi*(-1);

/*  stang:  correct the user entered angle with cstep and report the
```

```
    actual angle to which the goniometer was moved  */

stang = stang - cstep;
printf("Starting angle:  ");
printf("%f\n",stang);

/*  step:  reinitialize step as the number of pulses required for the
    stepper motor to move to the desired angular increment in degrees  */

step = stsi*stdeg;

printf("Turn correlator to autocycle now and strike any key\n ");
getch();

/*************************************************************/
/*  'for' controlling loop in MAIN() which makes calls for   */
/*   data acquisition and motor control                      */
/*     i.e.  after rotation to the initial starting angle,   */
/*           the program resides entirely in the loop below  */
/*************************************************************/

   for(k=0;k<=prepos;k++)  {
      printf("Sleeping...\n");
      sleep(slp+1);

 if (kbhit())  {
    while(kbhit()) {
    in = getch();
    }
    in = tolower(in);

       /*  'q' finishes up present data point collection
    then exits the program, keeping the goniometer
    at the last stated angle  */

       if (in == '\x71')  {
  printf("Finishing last cycle, closing all files\n");
  GET_COR(stang,ovfl,minc,k,step);
  fclose(fo);

  printf("Type p for final look at the plot?\n");

     if(getch()=='\x70')  {
 PL_IT(k);
 }
```

```
  closegraph();
  exit(0);
       }

       /*  'p' plots the data as log(I) vs. theta  */

       if (in == '\x70')  {
  printf("Plotting...\n");
  PL_IT(k);
  goto wow;
       }

  }


wow:

       /*  STEP to the next angle before dumping correlator data  */

       STEP_MOT(step,delay);
       printf("Getting correlator data...\n");
       flag = GET_COR(stang,ovfl,minc,k,step);

 /*  'if' there are too many overflows or not enough
       counts, back up to the last reported angle and
       exit the program  */

 if(flag == cflag)  {
    step = (-2)*(stsi*stdeg);
    STEP_MOT(step,delay);
    fclose(fo);

    printf("Type p for final look at the plot\n");

        if(getch()=='\x70')  {
  PL_IT(k);
       }
closegraph();
    exit(0);
 }
   }

fclose(fo);

printf("Type p for final look at the plot\n");
```

```
   if(getch()=='\x70')  {
      PL_IT(k);
   }
closegraph();

/*  step:  when all angles have been measured, back up to last reported
    angle and exit program  */

step = (-1)*(stsi*stdeg);
STEP_MOT(step,delay);

exit(0);
return 0;

}
/**********                END OF MAIN                **********/


/*************************************************************/
/**  CONTROL OF THE STEPPER MOTOR VIA THE PARALLEL PORT IS  **/
/**  ACHIEVED WITH STEP_MOT()                               **/
/*************************************************************/
STEP_MOT(step,delay)

int step,delay;

{

#define STATUS 0        /* status 0 means send the byte */
#define PORTNUM 0       /*     port number for LPT1     */

int i,j,chbyte,clbyte,abyte;

   if(step<0)  {
      step   = abs(step);
      chbyte = 6;       /* high byte for reverse step */
      clbyte = 4;       /* low  byte for reverse step */

   }

      else  {

 chbyte = 7;     /* high byte for forward step */
 clbyte = 5;     /* low  byte for forward step */
```

```
      }


   for(i=0;i<step;i++)  {
      abyte = chbyte;

 for(j=0;j<delay;j++)  {   /* delay loop */

 }

      biosprint(STATUS, abyte, PORTNUM);   /* send high to LPT1 */

      abyte = clbyte;

 for(j=0;j<delay;j++)  {   /* delay loop */

     }

       biosprint(STATUS, abyte, PORTNUM);   /* send low  to LPT1 */

   }

return 0;

}


/*********************************************************************/
/**  RETRIEVAL OF CORRELATION FUNCTION, INTENSITY AND CORRELATOR   **/
/**  CONTROL PANEL SETTINGS (see L.F. manual) VIA THE SERIAL PORT  **/
/**  IS ACHIEVED WITH GET_COR()                                    **/
/*********************************************************************/
GET_COR(stang,ovfl,minc,k,step)

int k,step,ovfl,minc;
float stang;

{

#define COM1 0
#define SETTINGS (0x80 | 0x02 | 0x00 | 0x18)
#define STATUS 0
#define PORTNUM 0
```

```
int abyte,data[400];
unsigned int fdata[80];
double vard,stangd;
int i,n,j,in, out, status,result;

bioscom(0,SETTINGS,COM1);

   if(step<0)  {
  abyte = 52;

   }

   else  {
  abyte = 53;

   }

biosprint(STATUS, abyte, PORTNUM);

abyte = abyte - 48;

j=0;
n=0;

   while(j<400)
   {
      if((out = bioscom(2,0,COM1) & 0x7F) !=0)  {
 if(isdigit(out))  {
    data[j]=out-48;
    j++;
 }
      }
   }

   for(j=0;j<400;j++)  {
      fdata[n] = data[j]*10000;
      fdata[n] = fdata[n] + data[j+1]*1000;
      fdata[n] = fdata[n] + data[j+2]*100;
      fdata[n] = fdata[n] + data[j+3]*10;
      fdata[n] = fdata[n] + data[j+4];

      /*** printf("%d\t%d\t%u\n",j,data[j],fdata[n]);  ***/
      n++;
      j = j + 4;
```

```
   }

   for(i=0;i<80;i++)  {

      for(j=0;j<10;j++)  {
 printf("%u ",fdata[i+j]);
 /***   fprintf(fo,"%u ",fdata[i+j]); ***/

      }

      printf("%s\n"," ");
      /***  fprintf(fo,"%s\n"," ");  ***/
      i=i+9;

   }

   /* 'if' checks for overflow condition  */

   if(fdata[70] > ovfl)  {
      OV_FLO();
      printf("*** overflow limit exceeded, closing files ***\n");
      biosprint(STATUS, abyte, PORTNUM);
      return(-1);

   }

stangd = stang + (step/69.4444)*(k);
vard = ((fdata[66]*(65536))+fdata[67]);

   /*  'if' checks for minimum counts  */

   if(vard < minc)  {
      OV_FLO();
      printf("*** minimum counts not satisfied, closing files ***\n");
      biosprint(STATUS, abyte, PORTNUM);
      return(-1);

   }

vard = vard*sin(3.14159*(stangd/180.));
if(vard < 0)  vard=vard*(-1);
fprintf(fo,"%f\t%f\t%u\n",stangd,vard,fdata[70]);
printf("%f\t%f\t%u\n",stangd,vard,fdata[70]);

vplt[k] = vard;
```

```
sleep(1);
biosprint(STATUS, abyte, PORTNUM);
return 0;

}

OV_FLO()

{
sound(100);
delay(2000);
nosound();
return(0);
}

/**  PL_IT() IS PLOTTING THE DATA  **/

PL_IT(k)

int k;

{

int i,maxx, maxy,ivplt,xax[500];
float crap,divplt;
double oqvplt,hplt;

if(k<2)  {
printf("Wait for at least two points please\n");
return 0;
}

maxx = getmaxx() + 1;
maxy = getmaxy() + 1;

oqvplt = 0;
xax[0] = 0;

   for(i=0;i<k;i++)  {

 if(vplt[i]>oqvplt)
{
       oqvplt = vplt[i];
  }
```

```
   }

hplt = oqvplt;

setgraphmode(getgraphmode());

   for(i=0;i<k;i++)  {
      crap = log10(vplt[i]);
      divplt = (crap/log10((hplt+1)))*170;
      ivplt = divplt;
      xax[i+1] = xax[i] + ((maxx-(maxx/3))/(k-1));
      ivplt = maxy - ivplt;

      putpixel(xax[i],ivplt,15);

   }

getch();
restorecrtmode();
return(0);

}

/**********      END OF PROGRAM      **********/
```

v

VITA

STEVEN EDWARD PAULIN

Candidate for the Degree of

Doctor of Philosophy

Thesis: MICROSTRUCTURE AND RHEOLOGY IN SUSPENSIONS OF SWOLLEN PMMA SPHERES

Major field: Physics

Biographical:

Personal Data: Born in Cleveland, Ohio, November 18, 1963, the son of Edward and Mary Jane Paulin. Married to Carol Diahann Bandy on May 5, 1990.

Education: Received Bachelor of Science Degree in Physics from Cleveland State University, Cleveland, Ohio in 1986; received Master of Science Degree in Physics from Oklahoma State University, Stillwater, Oklahoma in 1990; completed requirements for the Doctor of Philosophy Degree at Oklahoma State University, Stillwater, Oklahoma in December, 1993.

Professional Experience: Undergraduate Research Assistant, Cleveland State University, January 1985 to July 1987; Graduate Teaching Assistant, Oklahoma State University, August 1987 to December 1988; Graduate Research Assistant, Oklahoma State University, January 1989 to Present.